LITHUANIAN ENERGY INSTITUTE

EDGARAS MISIULIS

NUMERICAL INVESTIGATION OF THE BLOOD FLOW IN COMPLIANT ARTERIES

Doctoral Dissertation
Technological sciences, Energetics and Power Engineering (T 006)

2019, Kaunas

This doctoral dissertation was prepared at Lithuanian Energy Institute, Laboratory of Combustion Processes during the period of 2014-2018.

Scientific Supervisor:

Dr. Algis DŽIUGYS (Lithuanian Energy Institute, Technological Sciences, Energetics and Power Engineering – T 006).

Doctoral dissertation has been published in:
http://ktu.edu

Editor:

Jūratė Kulčickytė-Gutaitė (Lithuanian Energy Institute)

ISBN 978-609-02-1606-4

The bibliographic information about the publication is available in the National Bibliographic Data Bank (NBDB) of the Martynas Mažvydas National Library of Lithuania.

LIETUVOS ENERGETIKOS INSTITUTAS

EDGARAS MISIULIS

KRAUJO TEKĖJIMO TAMPRIOSE ARTERIJOSE SKAITINIS TYRIMAS

Daktaro disertacija
Technologijos mokslai, energetika ir termoinžinerija (T 006)

2019, Kaunas

Disertacija rengta 2014-2018 metais Lietuvos energetikos instituto Degimo procesų laboratorijoje.

Mokslinis vadovas:

Dr. Algis DŽIUGYS (Lietuvos energetikos institutas, technologijos mokslai, energetika ir termoinžinerija – T 006).

Interneto svetainės, kurioje skelbiama disertacija, adresas:
http://ktu.edu

Redagavo:

Jūratė Kulčickytė-Gutaitė (Lietuvos energetikos institutas)

ISBN 978-609-02-1606-4

Leidinio bibliografinė informacija pateikiama Lietuvos nacionalinės Martyno Mažvydo bibliotekos Nacionalinės bibliografijos duomenų banke (NBDB).

CONTENT

ABBREVIATIONS

TBI	-	Traumatic brain injury
ICP	-	Intracranial pressure
OA	-	Ophthalmic artery
ICA	-	Internal carotid artery
CCA	-	Common carotid artery
TDTCD	-	Two depth transcranial Doppler ultrasound
US	-	Ultrasonic
Pe	-	Added external pressure
IOA	-	Intracranial ophthalmic artery
OC	-	Optic canal
EOA	-	Extracranial ophthalmic artery
CFD	-	Computational fluid dynamics
FSI	-	Fluid-structure interaction
ALE	-	Arbitrary Lagrangian-Eulerian
FEM	-	Finite element method
MRI	-	Magnetic resonance imaging
RBC	-	Red blood cells
DNS	-	Direct numerical simulation
AAA	-	Abdominal aortic aneurysm
CSF	-	Cerebrospinal fluid
CPP	-	Cerebral perfusion pressure
IEL	-	Internal elastic lamina
EEL	-	External elastic lamina
3D	-	Three dimensional
SEF	-	Strain energy density function
CT	-	Computed tomography
OCT	-	Optical coherence tomography
DICOM	-	Digital imaging and communications in medicine
ISO	-	International organization for standardization

NOMENCLATURE

Notation	Units	Definition
A_{ICP}	Pa	amplitude of the intracranial pressure
A_{Pe}	Pa	amplitude of the external pressure
$\mathrm{d}\mathbf{A}$	m^2	infinitesimal oriented surface element in the material configuration
$\mathrm{d}\mathbf{a}$	m^2	infinitesimal oriented surface element in the spatial configuration
A	m^2	surface area in the material configuration
a	m^2	surface area in the spatial configuration
$\mathfrak{a}$	m	coefficient for the Fourier fit of the maximum inscribed sphere radius
a	m	cube side length
α		Womersley number
$\mathbf{B}_{\boldsymbol{\mathcal{F}}}$	N/m^3	body force in the material configuration
$\mathbf{B}$		left Cauchy-Green tensor
$\mathbf{b}_{\boldsymbol{\mathcal{F}}}$	N/m^3	body force in the spatial configuration
$\boldsymbol{\mathcal{B}}$		continuum body
b	m	deformed cube side length
$\mathfrak{b}$	m	coefficient for the Fourier fit of the maximum inscribed sphere radius
β	rad	fiber angle with respect to local circumferential component
$\Delta\beta$	%	the percentage ratio between difference in fiber angle obtained with different fiber definition methods and the prescribed fiber angle
c_{10}	Pa	arterial wall parameter used in isotropic part
c	m	deformed cube side length
$\boldsymbol{\chi}_p$		mapping from the load-free configuration to the loaded configuration
$\boldsymbol{\chi}_{res}$		mapping from the stress-free configuration to the load-free configuration
$\boldsymbol{\chi}_p$		mapping from the load-free configuration to the loaded configuration
$\boldsymbol{\chi}$		motion map (from the reference configuration to the current configuration)
$\mathbf{C}$		right Cauchy-Green deformation tensor
$\mathbf{c}$	m/s	convective velocity defined as the difference between material and mesh velocities
c		arbitrary coefficient
$\mathcal{D}_{\mathrm{int}}$	W/m^3	internal dissipation

$\mathbf{d}$	$1/s$	rate of deformation
d	m	vessel's lumen diameter
$\mathbf{e}$	m	basis vector
ε	Pa	deviation from the balance condition ICP = Pe
$\boldsymbol{\varphi}_a$		array of test functions
$\mathrm{d}\mathbf{f}$	N	infinitesimal force vector
$\mathbf{F}$		deformation gradient
f		arbitrary function
$\boldsymbol{\mathcal{F}}$	N	force
Γ		boundary
h_{wall}	m	thickness of vessel wall
I_1		first invariant of the elastic right Cauchy-Green deformation tensor
I_2		second invariant of the elastic right Cauchy-Green deformation tensor
I_3		third invariant of the elastic right Cauchy-Green deformation tensor
$\mathbf{I}$		identity tensor
ICP	Pa	intracranial pressure
J		determinant of the deformation gradient
k	N/m^3	spring constant
k_1	Pa	stress-like material parameter used in the anisotropic part of the material
k_2		dimensionless parameter used in the anisotropic part of the material
$\boldsymbol{\kappa}_{\mathrm{m}}$		mapping from the reference configuration to the material configuration
$\boldsymbol{\kappa}_{\mathrm{t}}$		mapping from the reference configuration to the current configuration
$\mathbf{K}$		arbitrary stiffness matrix
$\mathcal{K}$	J	kinetic energy
κ	Pa	bulk modulus
L_{exit}	m	outlet exit distance
$\mathbf{L}$	$N \cdot s$	linear momentum
L	m	length of vessel
l	m	distance between simulated measurement locations
λ		principal stretch
$\mathbf{M}$		arbitrary mass matrix
$\mathbf{M}_f$		fiber preferred direction tensor
$\mathbf{m}$		fiber direction vector
m	kg	mass
μ_f	$Pa \cdot s$	blood dynamic viscosity

μ	Pa	stress-like material parameter
$\mathbf{N}_a$		array of shape (trial) functions for the test functions
$\mathbf{N}_b$		array of shape (trial) functions for the arbitrary dependent variable
v		arbitrary approximate solution
$\mathbf{N}$		normal vector in the material configuration
$\mathbf{n}$		normal vector in the spatial configuration
N		shape (trial) function
n		number of arbitrary entries
O		origin
Δp	Pa	hydrodynamic pressure difference between two distinct simulated measurement locations
p_{add}	Pa	deviation due to mechanical non-equivalence between two distinct simulated measurement locations
P_{dist}	Pa	internal blood pressure at the outlet exit distance
P_v	Pa	prescribed internal blood pressure waveform
$\mathcal{P}_{\text{ext}}$	W	rate of external mechanical work
$\mathcal{P}_{\text{int}}$	W	rate of internal mechanical work done by the stress field
$\mathbf{P}$	N/m^2	first Piola-Kirchhoff stress tensor
P		arbitrary particle in the continuum body in material configuration
P	Pa	pressure
Pe	Pa	external pressure
p	Pa	pressure
p		arbitrary particle in the continuum body in spatial configuration
$\boldsymbol{\theta}_\Omega$		unit vector defining circumferential direction
Q		arbitrary particle in the continuum body closest to the particle P
q		arbitrary particle in the continuum body closest to the particle p
$\mathbf{R}$		rotation matrix
$\mathbf{R}_p$		array of externally applied nodal point loads
$\mathbf{r}_\Omega$		unit vector defining radial direction
R		radius in the material configuration
r		radius in the spatial configuration
Re		Reynolds number
ρ	kg/m^3	density
ϱ		dispersion
s_{Pe}	Pa	magnitude of the external pressure increase
s_{ICP}	Pa	magnitude of the intracranial pressure increase

$\boldsymbol{\sigma}_m$	N/m^2	volumetric stress
$\mathbf{S}$	N/m^2	second Piola-Kirchhoff stress tensor
S	m^2	lumen cross-sectional area
$\boldsymbol{\sigma}$	N/m^2	Cauchy stress tensor
t_{init}	s	duration of initialization
t_P	s	duration of external pressure loop
t_c	s	duration of external pressure being constant
$\mathbf{T}$	N/m^2	traction vector in the material configuration
$\mathbf{t}$	N/m^2	traction vector in the spatial configuration
T	s	time period
t	s	time
$\mathbf{u}_b$		array of arbitrary dependent variable on boundary nodes
$u_{max_{mean}}$	m/s	the average of the blood flow velocity profile at the systole
$u_{max_{peak}}$	m/s	the maximum of the blood flow velocity profile at the systole
$u_{min_{mean}}$	m/s	the average of the blood flow velocity profile at the diastole
$u_{min_{peak}}$	m/s	the maximum of the blood flow velocity profile at the diastole
u_v	J/m^3	internal energy per unit current volume
$\mathbf{U}$		right stretch tensor
$\mathbf{U}_d$	m	displacement in the material configuration
$\mathbf{U}_n$		nodal unknowns
U		arbitrary scalar field
$\mathbf{u}$	m	displacement in the spatial configuration
u		arbitrary dependent variable
$\mathcal{U}$	J	internal energy
Ψ	J/m^3	the strain energy density function
$\mathbf{v}_b$		array of arbitrary dependent variable on domain
$\mathbf{V}$	m/s	velocity in the material configuration
$\mathbf{v}$	m/s	velocity
V	m^3	volume in the material configuration
v	m^3	volume in the spatial configuration
w_{int}	W/m^3	real physical rate of internal mechanical work per unit reference volume
w_f		coefficient for the Fourier fit of the maximum inscribed sphere radius
w		weight function (test function)
Ω		domain
$\mathrm{d}\mathbf{X}$	m	material tangent vector of the material curve
$\mathrm{d}\mathbf{x}$	m	spatial tangent vector of the spatial curve
$\mathbf{X}$	m	position vector in the material configuration
$\mathbf{x}$	m	position vector in the spatial configuration

ξ	parametrization of the smoothed out centerline of the vessel
$\mathbf{z}_\Omega$	unit vector defining axial direction
∇	nabla operator

Subscripts:

0	reference configuration
D	Dirichlet boundary condition
$dias$	diastolic
EOA	extracranial segment of ophthalmic artery
f	fluid
ICA	internal carotid artery
IOA	intracranial segment of ophthalmic artery
i	index
in	defined on inlet boundary
$init$	initial
max	maximum
N	Neumann boundary condition
OA	ophthalmic artery
OC	optic canal of ophthalmic artery
out	defined on outlet boundary
S	cross-sectional area
s	solid
sys	systolic
t	current configuration
v	volume in current configuration
vol	volumetric part
V	volume in reference configuration

Accents:

$\bar{}$	isochoric part

NOTE: Symbols in bold sign vectors, or tensors or mapping functions, except cases commented directly in the text.

INTRODUCTION

In the dissertation, the investigation of the blood flow in the ophthalmic artery is presented. It is part of the broader task of pulsating fluid flow in the compliant channel. The objectives and the tasks emerged in pursuance to investigate the conditions and to improve the accuracy of the non-invasive intracranial pressure measurement (nICP) method, which is based on the peculiarities of the blood flow in the ophthalmic artery.

The blood flow system of the human, in principle, is a mass and heat transfer system, whose research requires consideration of not only the fluid dynamics, but also the dynamics of blood vessels and the interaction between blood flow and blood vessels. As with other cerebral vessels, the ophthalmic artery is affected by the intracranial pressure. However, at the same time, the part of the ophthalmic artery, which is outside the skull, is exposed to the external pressure. This unique feature of the ophthalmic artery is used in the nICP method and is the objective of this investigation.

The intracranial pressure (ICP) is the dynamic pressure acting inside the human skull and for a healthy human being mean ICP is in the range from 2 mmHg to 15 mmHg depending on age, conditions and patient-specificities. An ICP value outside these limits is a life threatening condition as it poses the risk of the secondary brain injury. The secondary brain injury can be caused in many situations of which here we name a few: the traumatic brain injury (TBI), which is one of the leading causes of disability and death worldwide, the intracranial and central nervous system tumors, infections after cranial surgery, prolonged stay in microgravity conditions, specific surgeries that requires a patient to lay with the head tilted down for an extended period of time, etc. In all of these aforementioned and in other cases one of the possible prevention methods of the secondary brain injury is the monitoring of ICP, which allows clinicians to resolve their further actions based on the available additional ICP measure.

Until now, the gold standard method of the ICP monitoring is the use of the invasive ICP (iICP) intraventricular catheters; nevertheless this method pose the risk of complications, requires qualified neurosurgeons to perform it and the patient must be hospitalized. Hospitalization results in a delay of an additional ICP measure provision to the clinicians, which is very important to obtain during the first hour after the event. The disadvantages of the iICP monitoring methods led scientists to develop new non-invasive ICP (nICP) methods.

One of the emerging nICP monitoring methods is based on the unique ophthalmic artery (OA) morphological property: commonly, the OA can be divided into three segments (Fig. 1): the segment that originates from the internal carotid artery (ICA) and resides in the intracranial space (IOA), followed by the segment that traverses the optic canal (OC), and the third segment that resides in the eye socket (EOA). Presumably, the ICP affects the IOA and OC segments, while the eye socket pressure affects the EOA segment. In addition, added external pressure (Pe) can affect the EOA segment in such a way that the information obtained by measuring the blood flow velocity in (IOA, OC) and EOA segments in turn can be translated into the value

of ICP. However, in order to extend its application into the clinical practice the accuracy of the nICP method must be increased.

The accuracy of the nICP measurement depends not only on the properties of the device, but also on the properties of the object being measured (blood flow in the compliant OA affected by ICP and Pe). Therefore, the need of fundamental understanding of the pulsating blood flow in the OA when ICP and Pe affects different OA segments arises.

Clinical research is too expensive or sometimes even impossible to perform, as for example up till now, the absolute value of blood flow velocity cannot be measured credibly as it depends on the angle of measurement. With the advent of the sophisticated computational methods and available computing power, numerical simulations of this type are now possible. However, many factors influence the model's ability to simulate the physical system.

Previous investigations have not considered the patient-specific curvature of the ophthalmic artery, which can be an important factor affecting the blood flow and the accuracy of the non-invasive intracranial pressure measurement. Therefore, the **aim of the research** - by means of the numerical method, determine the dependencies of the blood flow of the compliant curved (patient-specific) ophthalmic artery based on additional external pressure applied when using the non-invasive intracranial pressure measurement method. The **object of the research** - the blood flow in the compliant patient-specific ophthalmic artery exposed to the additional external pressure applied when using the non-invasive intracranial pressure measurement method.

To achieve the research aim it was necessary to develop a method for the modeling of the patient–specific ophthalmic artery using the state-of-the-art artery wall material model by forming a vector field that models the fibrous structure of the artery wall.

In order to achieve the goal, the following research objectives were raised:

- Develop a method for the formation of the uniformly directed fiber structure, that is independent of the material model.
- Determine the dependencies of the arterial blood flow on the intracranial pressure, modeled measurement distance and the added external pressure.
- Determine the dependencies of the systematic deviation of the non-invasive intracranial pressure measurement on the prescribed intracranial pressure and distance according to the differences of cross-sectional areas and average blood flow velocities.

Scientific novelty

The dependencies of the standard deviation of the differences of the average blood flow velocities and the cross-sectional areas of the ophthalmic artery from their over the heartbeat pulse period averaged values on the acting pressures and the distance were determined.

Practical value

The established dependencies of the blood flow of the ophthalmic artery can be used to increase the accuracy of the non-invasive intracranial pressure measurement method. Developed numerical model can be adapted to solve various compliant material-fluid interaction problems.

Statements carried out for defense

1. Developed method produces directly uniform fiber structure that is independent on the material model.
2. By increasing the added external pressure, the minimum standard deviation of the cross-sectional area difference, from over the heartbeat pulse period averaged cross-sectional area difference, will be obtained at a larger distance.
3. The standard deviation of the mean blood flow velocity difference, from over the heartbeat pulse period averaged mean blood flow velocity difference, is proportional to the distance.
4. By increasing the added external pressure or with the increasing intracranial pressure, the standard deviation of the mean blood flow velocity difference, from over the heartbeat pulse period averaged mean blood flow velocity difference, increases.
5. By increasing the prescribed intracranial pressure, the systematic deviation of the intracranial pressure obtained during the modeled measurement decreases.
6. By increasing the distance between the measurement locations, the systematic deviation of the intracranial pressure obtained during the modeled measurement increases.

Scientific approval

The results presented in this dissertation were published in 3 scientific articles, of which 2 are published in a journals with an impact factor that is referenced in the "Clarivate Analytics" "Web of Science" database, the third is published in the scientific journal, registered in the international scientific information databases. The results were also presented in 8 conferences, 5 of which were international.

Structure and content

The content of the dissertation is as follows: the introduction, where the problem is defined, followed by the literature review, where the newest scientific articles are reviewed that is relevant to the problem followed by the methods chapter that mainly highlights the continuum mechanics, finite element method and presents the research methodology based upon which the numerical studies are performed and the results are presented in the consecutive chapter. In the last chapters the conclusions and the list of referred scientific literature.

1 LITERATURE REVIEW

Today, one of the leading causes of disability and death worldwide are severe traumatic brain injuries (TBI), especially among children and young adults. Each year, around 7 million cases of TBI are recorded, and it is calculated that by the year 2020, this threat will become number one among fatal injuries (Roozenbeek et al., 2013). Intracranial and central nervous system tumors are the 17th most common cancer type worldwide, with more than 256,000 new cases diagnosed in 2012 (Torre et al., 2015). Infections after cranial surgery are also very serious threats that require immediate recognition and treatment (Dashti et al., 2008). Microgravity conditions could affect the human body's fluidic system, which in turn affects intracranial pressure (ICP), leading to vision deterioration or even vision loss (Hargens et al., 2013).

Clinically, only the secondary brain damage can be prevented, as the only prevention of primary head injury is higher self-awareness. Secondary brain damage is caused by excessive brain swelling. Human skull, once the sutures and fontanelles have been closed, becomes a structure that permits no further expansion; consequently, the internal volume is negligibly dependent on ICP (Rodríguez-Boto et al., 2015). ICP is the pressure inside the human skull and thus in the brain tissue and cerebrospinal fluid. The increase in ICP could be acute or chronic (Asiedu et al., 2014). For a healthy adult in the supine position, normal ICP values are in the range between 7 mmHg and 15 mmHg (Steiner et al., 2006), for children between 3 mmHg and 7 mmHg, for term infants from 2 mmHg and 6 mmHg, and for pathological patients, ICP can exceed 25 mmHg (Dunn, 2002).

ICP is a result of interactions among internal constituents, such as arterial blood, venous blood, cerebrospinal fluid, and brain tissue. Brain tissue is sensitive to blood flow dynamics, and several mechanisms (metabolic, myogenic, and neurogenic) are involved in maintaining the appropriate cerebral blood pressure. Within certain limits, a human body utilizes auto regulatory mechanisms of ICP, which is also known as the Monro-Kellie hypothesis (Mokri, 2001). When the auto regulatory mechanism fails, secondary brain damage may occur.

In aforementioned situations, adequate patient monitoring can help in prevention of the secondary brain damage and could enable making clinical decisions in a timely manner. Intracranial pressure can be monitored invasively and noninvasively. The gold standard for ICP measurement is the use of intraventricular catheters that are connected to an external pressure transducer; nevertheless, this invasive method increases the risk of complications (Hickman et al., 1990). Invasive methods have only proven to be accurate in short term, due to the need of calibration - a zero drift is a common problem (Dashti et al., 2008), also implementation of invasive methods requires qualified neurosurgeons (Dashti et al., 2008). Therefore, an accurate and certified nICP measurement method is needed. There are several proposed nICP measurement methods, such as numerical modeling, medical imaging, the implementation of the impedance mismatch principle, etc. (Raboel et al., 2012, Asiedu et al., 2014, Padayachy, 2016). One of the most promising nICP measurement method among them uses ophthalmic artery as a sensor to safely monitor intracranial

pressure (Ragauskas et al., 1999, 2005). As result, the ophthalmic artery (OA) becomes a very important sensor that provides information about the brain state, a sensor that can be used to determine the causes, course, and consequences of illnesses, for example glaucoma (Siaudvytyte et al., 2015).

OA supplies oxygenated blood to the eye. In most cases, it is the first intracranial bifurcation of the internal carotid artery (ICA), which in turn arises from the common carotid artery (CCA), which bifurcates from the abdominal aorta (AA). OA starts inside the cranium and traverses the optic nerve canal to the eye socket, which is outside the skull (Ho et al., 2012) (Fig. 1).

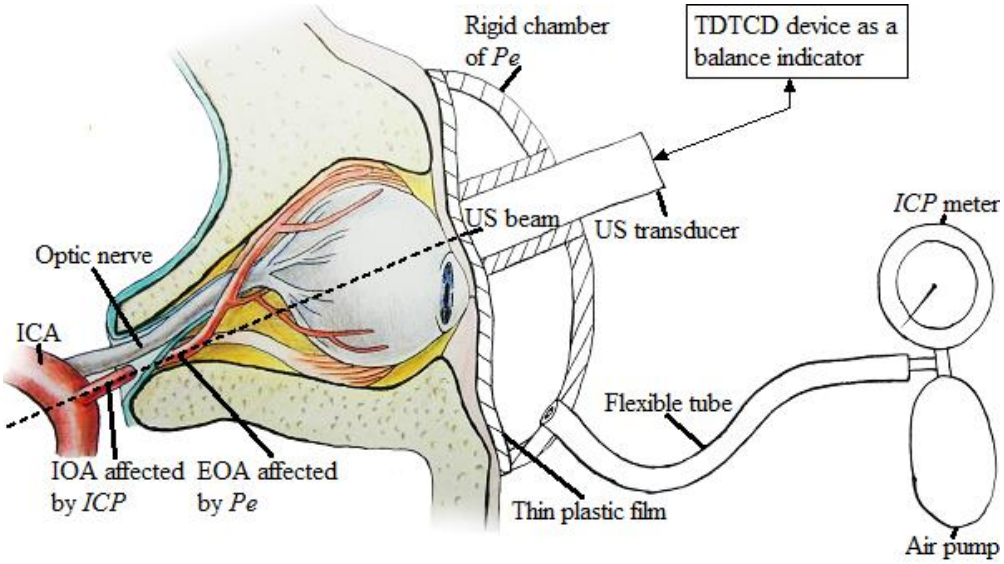

Fig. 1. The nICP measurement scheme. A special mask that consists of a rigid chamber with a deformable thin plastic film and an ultrasonic (US) transducer is placed on the patient's head. While the Pe is being applied on the EOA segment, the US transducer measures the velocity of blood flow in the IOA and EOA segments and sends the data to a TDTCD device for processing. Figure reproduced from Fig. 1 in (Misiulis et al., 2017)

The nICP measurement method is based on the simultaneous measurement of the blood flow velocity in the OA at two distinct locations using the two-depth transcranial Doppler ultrasound (TDTCD) technique: in the intracranial space of the OA (IOA) and in the eye socket, EOA. Additional external pressure Pe is introduced in the cushion of the special head mask, tightly enclosing the area around the eye.

Head mask and measurement equipment consists of several devices in which the most vital are external air pump, inflatable cushion, rigid chamber, ultrasound device and a signal-processing unit. During ICP measurement, the air is regularly pumped (approximately increasing Pe by 2 mmHg on every 10-heart pulses) to the inflatable cushion of which part of a surface surrounds the eye while the other part is enclosed by a rigid chamber. Measurements of blood flow velocity in IOA and EOA segments are performed by ultrasound waves generated by Two Depth Transcranial Doppler (TDTD) device that is mounted on a head mask's rigid chamber while being enveloped by the cushion. It should be oriented towards OA in the optimum manner,

although this optimum manner is still in question and requires its own research. During the blood flow, measurement the obtained velocity value is dependent on the angle between the incident ultrasound beam and the blood flow direction, therefore the relative blood flow velocity is obtained. Recorded signals representing a relative blood flow velocity profile are transferred to a signal processing unit where, based on the balance principle (Ragauskas et al., 2005), further data operations are made to obtain the ICP value.

In the balance principle, it is postulated that when the added external pressure Pe is close to ICP then the values of measured blood flow velocity in IOA and EOA segments are also approximately equal.

A working device for the nICP monitoring was created and is already patented in Europe and USA (Ragauskas et al., 1999, 2013, Chomskis et al., 2011). The device was practically tested and validated through an *in vivo* TDTCD measurements and the results were compared with the invasive methods (Ragauskas et al., 2005, 2012, Siaudvytyte et al., 2015), including the "gold standard" ventricular ICP method (Krakauskaite et al., 2016). In order to extend the device usage in the clinical practice, the accuracy of the nICP measurement must be improved. According to the ANSI/AAMI standards, the accuracy of the ICP measuring device should not exceed ± 2 mmHg in the range of 0–20 mmHg, and in the range of 20–100 mmHg, the maximum error should not exceed $\pm 10\%$ (Kawoos et al., 2015). Further device improvements e.g.: increase in precision, extension of its capabilities and applicability, requires fundamental understanding of a pulsatile blood flow in a compliant OA and its interaction with surrounding tissues when the outer wall of OA is exposed to varying pressures. Experiments *in vivo* are too expensive or even impossible to perform, while the numerical simulation of the blood flow in the compliant OA in situations close to those encountered during the nICP measurements allows performing the accuracy assessment of the nICP measurement method.

The problem requires a multidisciplinary approach incorporating the blood flow (hemodynamics, computational fluid mechanics (CFD)), arterial compliance (nonlinear solid mechanics, biomechanics) and its constitutive models (fiber-reinforcement linked to the internal collagen structure), blood flow-arterial tissue interaction (fluid-structure interaction (FSI)) and in this case for the large displacements and large deformations the arbitrary Lagrangian-Eulerian (ALE) formulation, numerical procedures (finite element method (FEM)) all of which diverse from the continuum mechanics, in addition, knowledge about the human cardiovascular system, blood properties, intracranial pressure inside the human head, artery wall structure and its mechanical behavior, geometry reconstruction techniques from medical imaging, evaluation of prestress that is common to arteries and the morphological properties of OA.

In the next sub-chapters, we will present the literature review that is required to define the physical problem based on the state of the art knowledge in the respective scientific fields.

1.1 Human cardiovascular system

Human cardiovascular system is the momentum, energy and mass transport system. The momentum of the blood stream is generated by the heart muscle contraction, in which the chemical energy is converted to the bulk kinetic energy. Energy transfer is due to the molecular kinetic energy (temperature) transfer. Mass transfer is mostly happening in the capillaries where there is an exchange of oxygen and carbon dioxide or any other molecular species (generally nutrients and waste exchange).

Blood circulatory systems between humans differ by their spatial configuration, path variations, mechanical properties, etc. From here, we can take statistical approach and evaluate a large number of people to generate database, which further can be used for preliminary predictions. Notably, in scientific articles, artistically designed variations of a part of human vessel networks are given with percentage marks that describe the chance of finding a particular vessel network path variation (Hayreh, 1962a, 1962b, 1962c, 2006). Many investigations were carried out where the mechanical properties of various arteries for a large group of people were measured, and it was found that they depend on the location in the human body (or otherwise depends on the artery) (Riley et al., 1992, Kamenskiy et al., 2012). The blood flow rates at different cardiovascular system's segments were measured and statistical data was obtained (Holdsworth et al., 1999, Khamdaeng et al., 2012). Although the statistical approach has its own benefits, the only way to investigate and predict with higher detail is to include patient specific information as differences in human bodies are not only within the vessel networks, but also within any other bodily systems. Depending on the problem these differences sometimes can be neglected, but sometimes are crucial and must be seriously considered.

Not only do every human body is different but also many interdependencies coexist in live human being and change in one may have a substantial effect on the other. In addition, external stimuli can have a profound effect on the body's inner workings.

We must note that different size scales of tissues composing human body exist. We can evaluate human system as composed of organs and form macroscopic equations. However, at some point we will have to take into account cells – the buildings blocks of human organs, here we might need to construct microscopic equations to predict system behavior. In addition, at some point we will have to take into account the molecular structure where we need to construct equations based on the kinetic theory. So the human body is a specific, multi-scale, inter- and extern-dependent ever changing system.

For these reasons, human body is one of the hardest systems to investigate and predict. The main limiting factor is the computing power, for which to simulate the whole multi-scale human body is a tremendously demanding task. In addition, the acquisition of all the patient specific data would be an extreme challenge, and to worsen things everything must be done in such a way that would not influence the system itself, which is extremely counteractive. If we consider only the vascular structure alone there exists great progress made on robust vascular network

extractions from medical imaging data (Gould et al., 2017), but even acquiring only the vascular network data is still a very time-consuming task, and requires experts in this field. Vessel resistance is strongly dependent on vessel radius, and so the extreme accuracy of geometry reconstruction of vessel network is needed to compute accurate blood flow field.

To cope with this problem one of the solutions is to form a numerical model, such that would require the least amount of computing power and would be able to reproduce empirical data (high fidelity local phenomena, or simplified global phenomena) in some range of the variable parameter or parameters. To accomplish such thing lumped numerical models are created, where only the local problem within a lumped volume is further investigated, usually, at the macroscopic level. To have as much realistic system as possible the adequate boundary conditions is the key problem (Lorthois et al., 2011). Boundary conditions of blood flow are usually defined by artificial networks (Su et al., 2012, El-Bouri et al., 2015, 2016) that are based on the electric scheme analog with various analogous items: resistors, capacitors and inductive bands.

One of the simplest model is the windkessel model, which uses few lumped parameters to define the overall behavior of blood flow in a large number of vessels (Mandeville et al., 1999, Buxton et al., 2004, Segers et al., 2008, Zheng et al., 2009). The lumped parameter models are limited by their simplicity and the difficulty to link problem with the network physiology. Some authors use a constant pressure boundary conditions, which are the simplest of all to implement and based on the problem can have negligible effect on the solution. Other authors use bifurcating vessels as their vascular network scheme (Payne et al., 2018) but in these models no spatial information is considered.

Arterial elasticity dampens the arterial pulse pressure wave maintaining stable blood flow throughout the cardiac cycle. As the walls of larger arteries contain elastin fibers, they distend during systole, and recoil during diastole. In addition, due to distant vasculature resistance the net blood flow in elastic region is higher, which means that during systole a net storage of blood accumulates in the elastic arteries. This accumulated blood is discharged during diastole assisting in the maintenance of organ perfusion. Although windkessel effect is extensively used in blood flow modeling it is superseded by the modern ideas, which interpret arterial pressure and blood flow waveforms in terms of wave propagation and reflection (Nichols et al., 2011). There are also proposed methods that encompass both effects (Schaafsma, 2014).

1.2 Blood

Blood is a fluid used to transport nutrients and oxygen to the organism cells and metabolic waste products away from these cells. Blood stream is composed of suspension of erythrocytes (red blood cells, RBC) 45% by vol., thrombocytes (platelets), leukocytes (white blood cells) 0.7% by vol. and a fluidic blood plasma 54.3% by vol. (Thibodeau et al., 2012). The proportion of blood occupied by red blood cells is called hematocrit, and in normal conditions, it is about 45%.

Blood plasma is a solution containing 92% of water, 8% of blood plasma proteins, and some amount of other materials. Plasma circulates dissolved nutrients, glucose, amino acids, and fatty acids, which can be bound to plasma proteins or dissolved in blood, and removes waste products such as urea, lactic acid, carbon dioxide.

Depending on the problem blood flow can be modeled as a one-phase or multi-phase, one-scale or multi-scale, Newtonian or non-Newtonian fluid and flow being laminar or turbulent, mostly depending on the vessel size, blood flow patterns and other considerations. In the multi-scale analysis, the continuum approach is coupled with the discrete particle method. When using the discrete particle method the red blood cells are governed by the spring network model that can be integrated within continuum model based on the minimum energy concept (Nakamura et al., 2013).

Blood exhibits non-Newtonian fluid dynamics, however if the shear rate is larger than 100 s^{-1} then constant dynamic viscosity will provide similar wall shear stresses and flow patterns as non-Newtonian models (Berger et al., 2000). This large shear rate can be approximated with a vessel diameter and hematocrit parameters, and usually if there are no stagnation points or backflow, the constant viscosity can accurately capture the blood flow behavior in the arteries whose diameter is larger than 1 mm (Tu et al., 2015). In the scientific community the effects of the non-Newtonian blood model versus the Newtonian blood model was studied in (Jung et al., 2006, 2008, Bernsdorf et al., 2009, Liu et al., 2011, Razavi et al., 2011, Karimi et al., 2014, Apostolidis et al., 2015, Akbar, 2016, Doost et al., 2016) without reaching a concluding remark whether these effects are significant in large arteries. Recently, (Marrero et al., 2014) have performed a direct numerical simulation (DNS) (the gold standard of fluid simulation, resolving all turbulent length scales down to Kolmogorov scale) of pulsatile blood flow in abdominal aortic aneurysm (AAA) and compared Newtonian and non-Newtonian blood flow models. They have found that in case Newtonian law governed blood viscosity, high shear layers led to a greater flow unsteadiness relative to the non-Newtonian viscosity model of the blood flow. This resulted in non-Newtonian model being less computationally expensive model and the wall shear stress distribution prediction was comparable between models.

1.3 Intracranial pressure

Normal ICP varies cyclically with cardiac cycle, respiration, there also could be rapid changes in ICP with straining, coughing and change of posture (Wykes et al., 2015). Intracranial space of a healthy human contains about 1400 ml of brain tissue, 80 ml of cerebrospinal fluid (CSF) and 150 ml of cerebral blood (Rajesh et al., 2017). Intracranial space is space inside the rigid human skull, which means that the inside volume is fixed. These constituents exert an evenly distributed inside pressure called intracranial pressure (ICP).

CSF is a colorless fluid mainly composed of water. It is generated by the choroid plexus at the rate of a 500 milliliters per day, meaning that the entire CSF volume of 150 ml is replaced more than three times a day (Puntis et al., 2016). CSF is contained

between the arachnoid membrane and the pia mater. CSF provides mechanical protection, chemical stability and buoyancy for the brain.

The Monro-Kellie doctrine states that the sum of all the constituents in the intracranial space volumes is constant and therefore any increase in the volume of a constituent, must be offset by a decrease in the volume of any other constituent as otherwise ICP will rise (Mokri, 2001) (Fig. 2). This is being accomplished by cerebral auto regulatory mechanism, which may displace some of the CSF into the spinal *intradural* space and the vascular resistance may change that will result in the increased drainage of cerebral veins and venous sinuses into systemic venous system (Oswal et al., 2017). Failing of auto regulatory mechanism happens when these before mentioned methods are fully exhausted or if the change in volume is very rapid as in case of spontaneous hematoma, and this will lead to the increase in ICP. Increased ICP is very hazardous to life as the tissue of the brain is the least tolerant to oxygen deprivation.

Human brain receives about 20% of the blood flow of cardiac output (Langham, 2009). This blood flow is called the cerebral blood flow (CBF). Under normal physiological conditions, the cerebral autoregulation mechanism maintains about 50 ml/minute of 100 g brain tissue while the cerebral perfusion pressure changes in a range of (50-140 mmHg) by altering the vascular resistance (Fig. 3). In case of TBI, this mechanism may reach the exhaustion. When this happens the cerebral perfusion pressure (CPP) and CBF begins to closely correlate (Wykes et al., 2015).

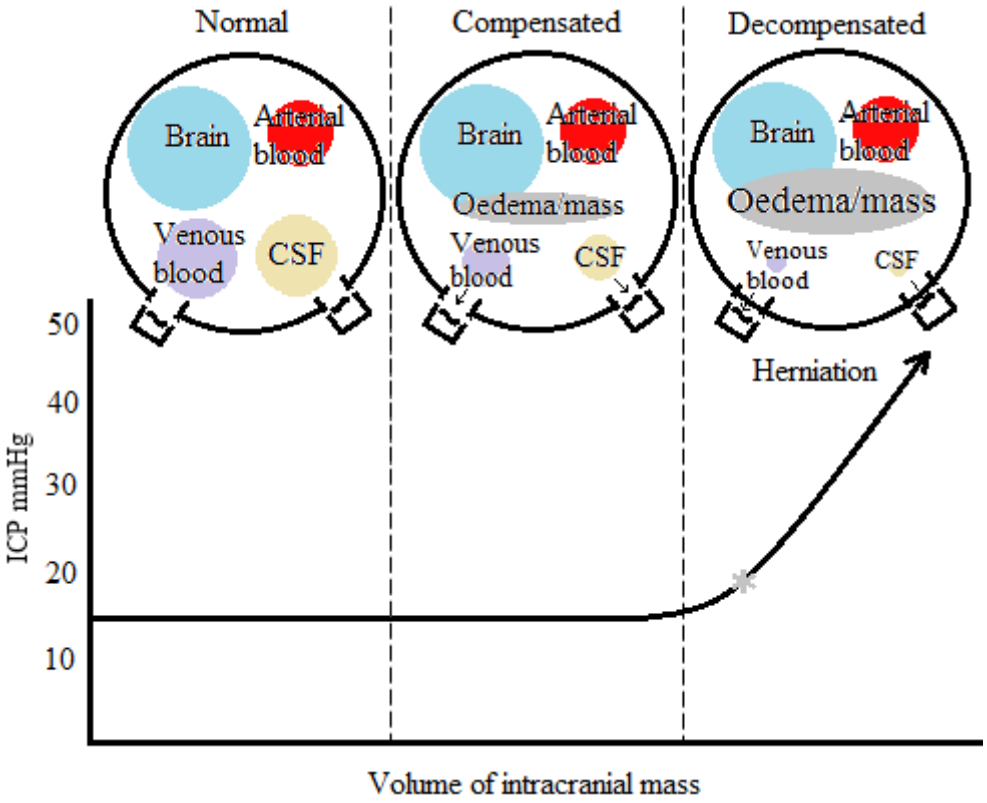

Fig. 2. The scheme of Monro-Kellie doctrine. When the swelling begins in the intracranial compartment, venous blood and cerebrospinal fluid decrease their volume by drainage (autoregulation). The exponential increase in intracranial pressure may lead to herniation

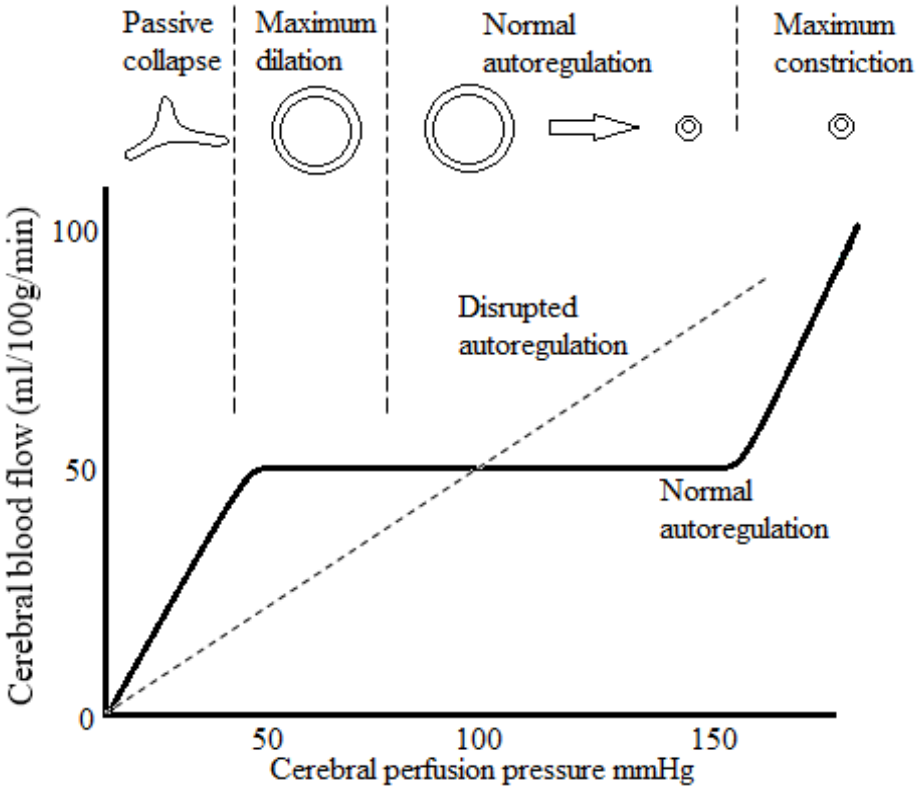

Fig. 3. The scheme of cerebral autoregulation. Abnormal or disrupted autoregulation results in a linear relation of the cerebral blood flow and cerebral perfusion pressure

1.4 Artery wall structure

Arteries are blood vessels through which blood flows away from the heart. The blood flowing through arteries is oxygenated with an only exception of pulmonary artery. Artery wall is a multilayer (Li et al., 2009) porous structure with plasma in the interstitial areas. All arteries have relatively thick walls and are able to withstand a heart generated high pressures. Because of this relatively high blood pressure, arteries tend to be round in cross-section.

Artery wall structure changes with its diameter, as smaller arteries contain more smooth muscle tissue, which gives them more control over the changing inside arterial blood pressure (Tricerri et al., 2016).

Structurally healthy artery wall is composed of three different layers: *tunica intima*, *tunica media* and *tunica adventitia* (Fortier et al., 2014) (Fig. 4). The proportion and structure of each artery wall varies with the size and the function of the particular artery.

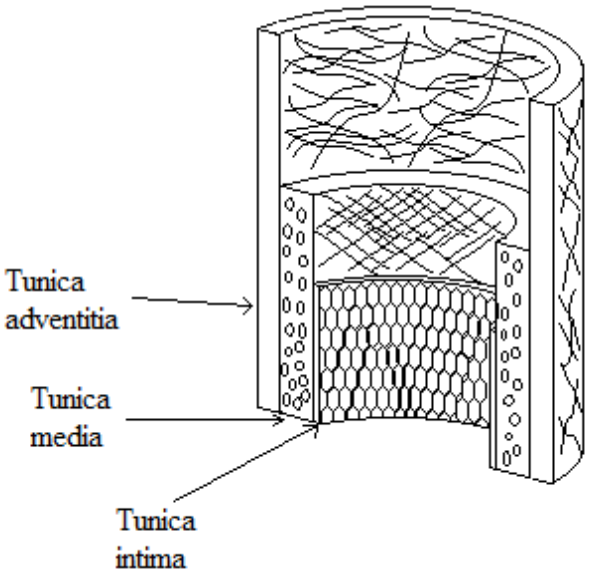

Fig. 4. Healthy artery wall layers: the innermost layer (*tunica intima),* middle layer (*tunica media),* and outermost layer (*tunica adventitia)*

Tunica intima is the innermost layer, which is in direct contact with the blood flowing in the artery. It consists of smooth *endothelial* cells that lines the *tunica intima,* elastic membrane and a *subendothelial* layer mainly consisting of connective tissues and collagen fibers. The outer boundary of *tunica intima* is composed of an elastic tissue with *fenestral* pores also called the internal elastic *lamina* (IEL). Damage induced to the *endothelial* lining leads to collagenous fibers exposure to blood, which is one of the primary cause of clot formation. *Endothelium* cells are physiologically critical as they can regulate capillary exchange and the blood flow. *Endothelium* releases local chemicals called *endothelins* that helps in constricting the smooth muscle cells that are embedded in the vessel wall, by, which increases the blood pressure. The excessive amount of *endothelins* can lead to hypertension (high blood pressure). Elastic membrane is used to link the *endothelium* with connective tissue and to provide strength while maintaining flexibility and this membrane is permeable to mass exchange.

Tunica media is the middle layer and consists of concentric sheets of smooth muscle cells, elastic fibers and some collagenous fibers. The outermost portion of *tunica media* consists of thin band of elastic fibers, also called external elastic *lamina* (EEL). Smooth muscle cells allows artery to contract and relax. In arteries, vasoconstriction is the decrease in blood flow by the artery contraction via the smooth muscles embedded in the artery wall narrowing the artery lumen and increasing the blood pressure. Vasodilation is the opposite effect reached when the smooth muscles relax and the lumen widens leading to the drop in the blood pressure. Both processes are regulated in part by nerves in the vessel wall called *nervi vasorum*. Locally

hormones and chemicals also control blood vessels. Neural and chemical mechanisms together control the blood flow to cope with the change in body conditions, such as hydration, exercising, etc. The smooth muscle layers are held by collagenous fibers, which bind all the artery wall layers. Elastic fibers add to flexibility while collagenous fibers in the outermost layer of *intima media* increase the strength of the artery.

Tunica adventitia is the outermost layer of arteries and consists of connective tissue mainly of composed collagen fibers, and smaller amount of elastic fibers and some capillaries. Elastic fibers help to stabilize the artery within the body.

All of this before mentioned structure falls into histological one scale semi-layered artery wall description. However, collagen fibers, one of the most important constituent in terms of artery wall mechanical behavior, are composed of smaller structures, forming their mechanical behavior. They can be regarded as periodic beam-like structures, which are composed of densely-packed fibrils (Bianchi et al., 2016). Fibrils are composed of staggered arrays of collagen molecules, which are interconnected with the head-to-tail arrangement by intermolecular covalent cross-links (Eyre et al., 2008). The behavior of collagen molecules is dependent on thermal effects and on the uncoiling process of collagen triple helices (Marino, 2012).

1.5 Artery wall mechanical behavior

Artery wall structure, chemical and physical factors, such as pH, osmotic pressure, temperature, partial pressures of carbon dioxide and oxygen, monosaccharide and ionic concentrations forms a basis of the artery wall mechanical behavior (Holzapfel et al., 2000). This behavior changes (arteries become stiffer or otherwise) along the vascular tree as the arterial wall structure changes, however the general mechanical behavior is conserved. The abundance of the possible transient, and long-term variations *in vivo*, the anisotropy of artery wall, makes it very hard to generalize arterial wall mechanical behavior *in vivo*. Therefore, the general artery wall mechanical behavior is determined *in vitro*, by inflation (Bader, 1967), uniaxial extension (Walsh et al., 2014), shear and other (Macrae et al., 2016) mechanical tests.

The compressibility of the hyperelastic arterial wall is an important parameter as the resulting stresses can differ significantly between the incompressible and slightly compressible material (up to 100%) (Yosibash et al., 2011). For a long time it was thought that arteries can be regarded as incompressible material, as their volume was found to stay constant under physiological conditions (Carew et al., 1968). Recently, studies performed by (Yosibash et al., 2014, Nolan et al., 2016, Yossef et al., 2017), have shown that arteries are slightly compressible.

From the stress-free configuration over a relatively high strain range, arteries are highly deformable and exhibit a non-linear stress-strain response with a typical exponential stiffening effect at higher stresses. Stiffening effect is due to collagen fibers, which are wavy when the strain is relatively low, and stretches when the strain becomes large.

Histologically artery wall can be considered as a composition of two constituents: the matrix of a relatively less stiff material, which, for example, can be a composition of smooth muscle cells, elastin fibers, etc. and a significantly stiffer

material embedded into the matrix - the protein collagen (Waller et al., 1992, Holzapfel et al., 2000). This histological feature leads to inhomogeneity and anisotropy or in an ideal case to the transverse isotropy.

1.6 Mathematical models of artery wall mechanical behavior

Artery wall is usually modeled using shell elements, which is a good approximation for structures that have a relatively high lumen diameter versus wall thickness ratio or 3D finite elements that fully resolve the inner stresses in artery wall (Dunn, 2006, Valencia et al., 2013). These elements are formulated based on the continuum mechanics. The mathematical models used to describe the artery wall behavior can be classified into two groups: phenomenological and mechanistic (Roccabianca et al., 2014). Models that define active mechanical behavior take into account the properties of elastin, collagen fibers and the degree of smooth muscle activation (Chen et al., 2017, Coccarelli et al., 2018). Passive behavior is defined in terms of the properties of elastin, collagen fibers, and some authors take into account the contribution of smooth muscles in a passive state (Taghizadeh et al., 2015).

Artery wall is usually threated as hyperelastic material, of which mechanical response is governed by strain energy density function (SEF). There are isotropic and anisotropic models. Isotropic models threat artery wall as if the whole tissue would react similarly to strains in any direction. In contrast, anisotropic artery wall models treat artery tissue as if the mechanical response is dependent on direction.

In artery models, SEF must satisfy polyconvexity condition as otherwise there would be no guarantee of the existence of realistic physical solution. In addition, the volumetric strain energy and isochoric strain energy functions must satisfy the requirement of objectivity under the change of coordinate systems.

(Tricerri et al., 2016) performed a numerical study on the ability of isotropic and anisotropic constitutive artery wall models to reproduce empirical data of the artery inflation tests. The isotropic models with their SEF satisfying the polyconvexity conditions were considered: the first order exponential model proposed by (Delfino et al., 1997), the second order exponential model (Balzani et al., 2006) and St. Venant-Kirchhoff. Following anisotropic models were also addressed: the second order exponential law along the fiber direction with different activation of *i*-th collagen fiber family in the reference and deformed configurations. Authors concluded that fitted coefficients of isotropic exponential law and anisotropic constitutive models enable to adequately model the experimental data and that in case histological data is unavailable isotropic models could adequately replace them. Authors also highlighted that spatial distribution of the mechanical stresses are highly affected by the constitutive models type: isotropic, anisotropic, and that this can have considerable effect when evaluating unhealthy arterial tissues.

(Auricchio et al., 2013) investigated the influence on the stress distribution between isotropic and anisotropic constitutive artery wall models. The isotropic model was a five parameter Mooney-Rivlin model, while anisotropic model was fiber-reinforced model proposed by (Holzapfel et al., 2000, Gasser et al., 2006). Authors have concluded that stresses formed using isotropic models can sometimes be higher

(up to 600%) when compared with reference anisotropic models, and therefore may lead to misinterpretation of the severity of the situation.

The more fundamental mechanistic models will provide more insight and will have higher predictive capabilities versus phenomenological models, while phenomenological models will reduce the need for the computing power. Therefore, usually, constructed simplified models are modified to account for more details in case problem requires and otherwise used as a fast and reliable basis for problems that they were originally intended to solve.

1.7 Geometry reconstruction from the medical imaging data

Vessel geometry reconstruction from the medical imaging data is a rapidly developing field, as new image capture techniques become available (Chiastra et al., 2017). It is the first step in developing a patient specific case study. The process of geometry reconstruction can be divided into several steps:

- Acquisition of medical images
- Segmentation of medical images

The first step of the patient specificity modeling is the obtaining of the medical image via one of the following methods: radiography, ultrasonography, computed tomography (CT), magnetic resonance imaging (MRI), radiation therapy, optical coherence tomography (OCT) or other techniques. Usually data of the image is stored in digital imaging and communications in medicine (DICOM) standard ISO format, where further it can be used for 3-D visualization or image segmentation.

The second step is the image segmentation. Image segmentation is a method of image partitioning into different segments with the same attributes as intensity, gray level, texture, etc. to obtain the desired object from the background (Bali et al., 2015) (Fig. 5). Image segmentation can be done manually or autonomously. Manual segmentation is prone to bias, expertise requirements and is a tedious time consuming task, and for these reasons automatic segmentation techniques are widely developed (Khan et al., 2018). Different authors provide different classification of automatic segmentation methods, probably due to different emphasis in their studies. Here the classification proposed by (Anjna et al., 2017) is used. Automatic image segmentation methods are based on the discontinuity detection (boundary, edge detection methods) or similarity detection methods (clustering) (Bali et al., 2015). These techniques are then further classified as structural, stochastic or hybrid methods. In structural methods, the structure of the segment is known *a priori*. In stochastic methods discrete information available in every pixel are used, while in the hybrid method both the structural and stochastic information is used (Anjna et al., 2017). Finally, the methods of segmentation are as follows: thresholding, edge based, region, clustering, watershed, partial differential equations, artificial neural network, etc.

Thresholding method is a structural method based on similarity detection, where the global, variable (local, adaptive), multiple threshold values on the intensity level are used to segment the image.

Edge based method is a structural method based on discontinuity detection, where the derivative of intensity is used to obtain the change in intensity levels near the edge. There are various edges: step, ramp, roof, line. Step edge results in an abrupt change in intensity level, while in ramp edge there is a gradual change in the intensity level. Roof edge results in a gradual increase of the intensity up to a maximum value, and then gradual decrease of intensity. The line edge is formed where the abrupt increase in the intensity is followed by the abrupt decrease in the intensity.

Region based method is based on the similarity detection. Region based methods are divided into two groups: region growing methods, split and merge methods. Region growing is performed by selecting (manually or automatically) the seed points, which based on the grey level, color, intensity similarity or threshold values expands further to segment object of interest. In split and merge technique, the initial image is continuously split into reasonable regions. After splitting was performed, the merging of the adjacent regions are performed based on defined similarity condition. This is done until no merging is possible.

Clustering based segmentation method is based on the similarity detection. Pixels with similar characteristics are grouped into clusters. There are two types of clustering methods: hierarchical and partition based methods. Hierarchical methods are based on the hierarchical tree, were the root represents the database, while the internal nodes represents clusters. Partition based methods use optimization techniques that iteratively minimize the objective function. Clusters are determined using algorithms that perform hard clustering or soft clustering. In hard clustering algorithm the pixel can only belong to one cluster, while in soft clustering the same pixel may belong to several clusters.

Watershed based segmentation method is based on the idea of watershed separating the two basins. This separation is done on the image based on its greytone, of which the preprocessed smoothed out gradient magnitude with aiding markers could be used to segment the image.

Partial differential equations based segmentation methods are relatively fast methods and can be used in cases where time is the significant parameter.

Artificial neural network based segmentation is based on the image mapping into the neural network, where pixel characteristics are defined. These artificial neural networks have to be trained with a large amount of input data.

Some of these methods are used in the computer software such as Vascular Modeling Toolkit (VMTK) (Fig. 5), 3D Slicer, MITK, etc.

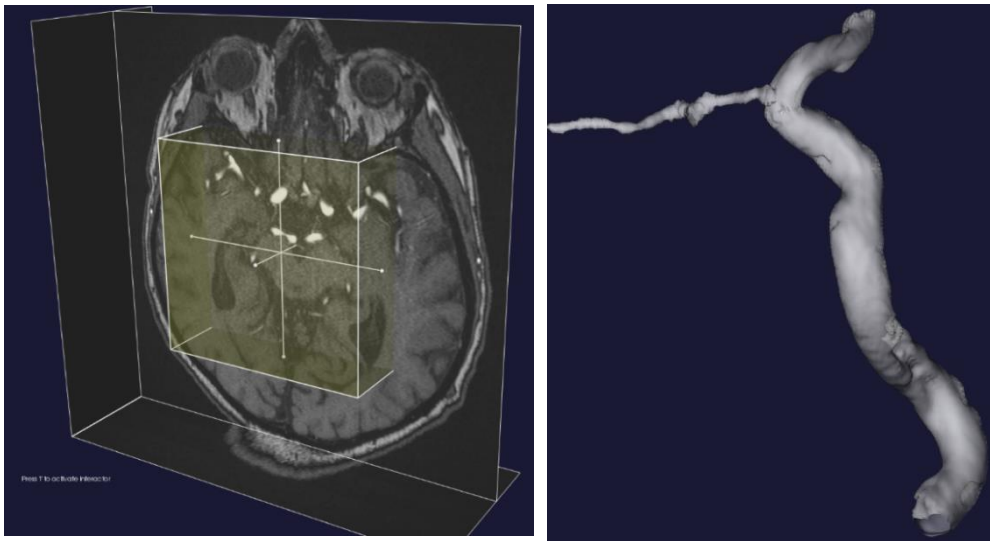

Fig. 5. Arterial network segmentation using “VMTK 1.3” computer software

1.8 Reconstruction of the prestress

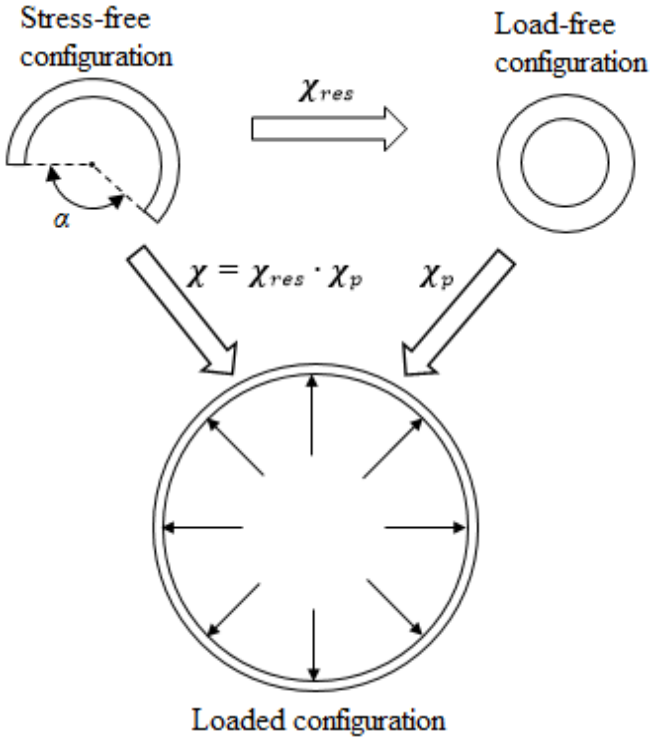

Fig. 6. The load free configuration of an artery resembles situation when there is no acting inside pressure, only prestress. Loaded configuration is similar to *in vivo* case when artery is prestressed and loaded by the internal arterial blood pressure

In the *in vivo* state artery wall is loaded and prestressed (Fig. 6), however during the geometry reconstruction from the medical imaging data the *in vivo* stress state cannot be reconstructed and without further actions, the obtained geometry would be assumed to be in a stress-free state, which is not adequate.

The pre-loading comes from the inner arterial blood pressure and viscous traction, which is defined by χ_p mapping, while prestress, defined by χ_{res} mapping, is due to the arterial growth and remodeling mechanisms or may accumulate due to cyclic loading (Huyghe et al., 1991).

The hyperelastic mechanical behavior of an artery wall is governed by the SEF, denoted as Ψ, and some material constants, which are usually obtained for the reference configuration. Reference configuration is usually a stress-free or load-free configuration that is obtained *in vitro*. As the artery reconstructed from the medical imaging is in the *in vivo* state, we cannot directly apply the SEF with material parameters obtained *in vitro* to model the mechanical behavior, the stresses of internal arterial blood pressure and prestress must be incorporated to match the configuration. Methods that perform such task are called the prestress algorithms. Several of these prestress algorithms are proposed in the scientific community.

The inverse design algorithm for quasi-incompressible material formulation was proposed by (Govindjee et al., 1998). The idea of inverse design analysis is to compute the un-deformed shape from the given final deformed shape, with available Cauchy tractions and displacement boundary conditions. The drawbacks of this method shown by (Gee et al., 2010) are the non-uniqueness of the stress-free material configuration and the buckling of thin walled structures. (Hsu et al., 2011) have proposed a prestressing method in, which the stress is iteratively accumulated in the second Piola-Kirchoff stress tensor by solving a modified variational formulation representing the balance of linear momentum of structural mechanics in the quasi-static analysis with the unknown being the displacement field. The drawback of this method is that although the stress state that is in equilibrium with the preloaded state is reached, the stiffness of the artery remains the same as the SEF is dependent on the deformation gradient, which is held close to the identity. Other method proposed by (Weisbecker et al., 2014) is used to incrementally update the deformation gradient, which also reconstructs the stiffness of an artery at the current stress level and is able to converge to the configuration obtained by a classical forward computation. However, this method is only applicable if the material law is path-independent.

1.9 Concluding remarks on the literature review

A thorough search of the relevant literature yielded only one scientific article presenting the numerical assessment of the accuracy of the nICP measurement method (Ragauskas et al., 2005). In (Ragauskas et al., 2005) the numerical model was presented, which considered the interaction of the pulsatile blood flow and the compliant OA in case of the straight, axisymmetric OA. Blood was considered as Newtonian fluid (Berger et al., 2000), while the dynamic blood flow and dynamic blood pressure boundary conditions were prescribed on the OA's inlet and outlet boundaries. The numerical modeling was performed using the finite difference method (Dimov et al., 2018). (Ragauskas et al., 2005) found that the systematic error of the nICP measurement method was within the range of [-3, 1] mmHg, while ICP changed in the range of [10, 40] mmHg. In addition, (Ragauskas et al., 2005) found that the $ICP = Pe$ balance condition holds regardless of the outlet resistance to the blood flow. In (Ragauskas et al., 2005) the stress-strain curve of the artery wall was considered exponential (Fung et al., 1979). However, current state-of-the-art constitutive artery wall models consider that the stress-strain curve of the artery wall material at the low end of the internal pressure range is approximately linear, and at the high end of the pressure range the exponential stiffening effect takes over (Li et al., 2016). Based on (Langham, 2009) OA's arterial pressure is dependent on the patient's condition and may be in both areas of the stress-strain curve, so it is important to incorporate the state-of-the-art constitutive material model that can accurately model the arterial mechanical response in a wide range of arterial pressures. In addition, the influence of the patient-specificity was not considered in (Ragauskas et al., 2005). Patient-specificity introduces curvature of the artery structure, which induce local effects (Chiastra et al., 2017) that may influence the systematic errors of the nICP measurement method.

In order to perform the numerical modeling and to assess the accuracy of the nICP measurement method in case of a patient-specific OA, it is necessary to develop a new methodology, since the application of a finite difference numerical model (Ragauskas et al., 2005) may be very difficult or even impossible. The resulting research methodology should allow the development of a sufficiently accurate numerical model of the blood flow in the patient-specific, compliant OA. With the developed numerical model the dependencies of the pulsatile blood flow in the compliant patient-specific ophthalmic artery under the conditions of the non-invasive intracranial measurement must be determined by performing numerical modeling and evaluating the dependencies of the standard deviation of the blood flow parameters and the dependencies of the method's systematic errors based on the measurement distance, intracranial and extracranial pressures.

1.10 The author's contribution

The author of the dissertation analyzed scientific data on causes, effects and measurement methods of the intracranial pressure, on human cardiovascular system and its numerical modeling, on the internal structure of the artery wall, its mechanical behavior and mathematical models describing that behavior, about methods used to reconstruct the artery from the medical data, about the *in vivo* strains and deformations of arteries and methods of their restoration, as well as numerical studies of non-invasive intracranial pressure measurement. The author of the dissertation has implemented a stress and deformation restoration algorithm for hyperelastic materials, introduced the state-of-the-art artery wall material model and applied its own fiber structure definition method in COMSOL Multiphysics® numerical modeling computer program. The author of the dissertation created a numerical model of the blood flow of the ophthalmic artery under a non-invasive intracranial pressure measurement and performed a research on blood flow dependencies and possible systematic deviation (error) dependence on measurement conditions and ophthalmic artery blood flow features. The author of the dissertation created functional dependencies describing the standard deviation of the mean blood flow velocity on modeled measurement distance, intracranial pressure, and added external pressure.

In the next chapter, we will present the ideas, mathematical concepts and methods that allowed us to develop and solve the defined problem**.**

2 METHODOLOGY

2.1 Prerequisites

The numerical investigation of the pulsating blood flow in the compliant OA under the conditions similar to those encountered during the nICP measurement requires a model that incorporates the mechanical behavior of the OA wall, the dynamics of pulsatile blood flow, and a model coupling the blood flow and the artery wall interaction. These before mentioned phenomena can be formulated in terms of partial differential equations, which can be efficiently solved with the finite element method, which is based on continuum mechanics.

The arterial tissue and blood is considered as continuous medium, of which mechanical behavior is governed by the conservation principles (conservation of mass, conservation of momentum, and balance of mechanical energy) and the material constitutive models. Motion and dynamics are described by field quantities that are either scalars, vectors or tensors.

In this chapter, the ideas and methods that are required in order to develop the numerical model encompassing before mentioned phenomena are introduced. In chapter 2.1.1 the brief introduction on the continuum mechanics are presented based on (Ogden, 1997, Holzapfel, 2000). In chapter 2.1.1.1 the motion, deformation and stain measures of the continuum body are defined. In chapter 2.1.1.2 the distributed external forces and the inside body forces called stresses are introduced. In chapter 2.1.1.3 the fundamental conservation principles of continuum mechanics are introduced concerning the conservation of mass, conservation of momentum, and balance of mechanical energy. In chapter 2.1.2, fluid-structure interaction method is introduced together with arbitrary Lagrangian-Eulerian (ALE) formulation, which enables tracking of the fluid-structure interface in large deformation analysis. The basic principles of the finite element method are presented in chapter 2.1.3.

2.1.1 The principles of continuum mechanics

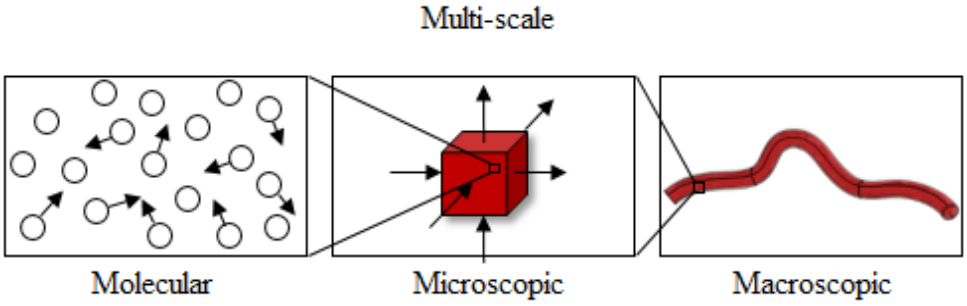

Fig. 7. The physical phenomena are multi-scale

All of the matter is made out of tiny particles called atoms. All of their interactions form the structural and fluidic behavior of an everyday life experiences.

The macroscopic system composed of countless number of particles would require an immense amount of computing power to solve all the motions and interactions happening at the molecular level. Usually, the compromise is made by implementing the continuum approach by which space properties are considered as homogeneous throughout the elementary volume, which substantially reduces computational effort required to solve the desired macroscopic system. The concept of continuum mechanics is used in solid mechanics and fluid mechanics, which has a vast number of application in engineering problems. In terms of fluid mechanics, Knudsen number defines to what extent the approximation of continuity is valid. The method of continuum mechanics estimates the complex collective behavior of many particle system without establishing the detailed formulation of the inner molecular working, but uses an approximation stating that all of this behavior can be characterized by some field quantity that is associated with the internal structure, for example, temperature, pressure, velocity, etc. These quantities form a macroscopic system (Fig. 7).

2.1.1.1 Motion, deformation and strain

Consider we have a continuum body, denoted as $\boldsymbol{\mathcal{B}}$, which is composed out of particles, which are large enough to be considered as continuous (Fig. 8). Let us introduce a right-handed, rectangular coordinate system, which is fixed at the origin point O with orthonormal basis vectors $\mathbf{e}_i$, where $i \in \{1, 2, 3\}$. The domain Ω that this body $\boldsymbol{\mathcal{B}}$ occupies at time $t_{init} = 0$ is referred as the material configuration. The position of arbitrarily chosen particle $P \in \boldsymbol{\mathcal{B}}$ is defined by the position vector $\mathbf{X}$ with respect to the introduced reference frame, while the position of the closest neighboring particle $Q \in \boldsymbol{\mathcal{B}}$ in the arbitrary direction is defined by the position vector $\mathbf{X} + \mathrm{d}\mathbf{X}$ with respect to the same reference frame, where $\mathrm{d}\mathbf{X}$ is the infinitesimally small line element between points P and Q. After time $t > t_{init}$ domain Ω experiences motion $\mathbf{x} = \boldsymbol{\chi}(\mathbf{X}, t)$, where motion $\boldsymbol{\chi}$ is one to one mapping from the configuration at time t_{init} (material) to the configuration at time t (spatial), and therefore, a new spatial configuration is obtained. The same points (P and Q) are displaced by $\mathbf{u}(\mathbf{X})$ and $\mathbf{u}(\mathbf{X} + \mathrm{d}\mathbf{X})$, respectively, and their position in the spatial configuration is now represented by particles p and q, of which the position vectors are defined by $\mathbf{x}$ and $\mathbf{x} + \mathrm{d}\mathbf{x}$, respectively (Fig. 8). The infinitesimally small distance between particles p and q is represented by the line element $\mathrm{d}\mathbf{x}$. The linear transformation of $\mathrm{d}\mathbf{X}$ into $\mathrm{d}\mathbf{x}$ is as follows:

$$\mathrm{d}\mathbf{x} = \mathbf{F}\mathrm{d}\mathbf{X} \tag{1}$$

were $\mathbf{F}$ is the deformation gradient tensor and it is defined as follow (Holzapfel, 2000):

$$\mathbf{F} = \frac{\partial \mathbf{x}}{\partial \mathbf{X}} \tag{2}$$

Due to motion, the continuum body can change its size and shape (deformation), position and orientation. If there is no change in size or shape then body is assumed

to be rigid, or it is not experiencing any external forces that will result in internal forces (stresses).

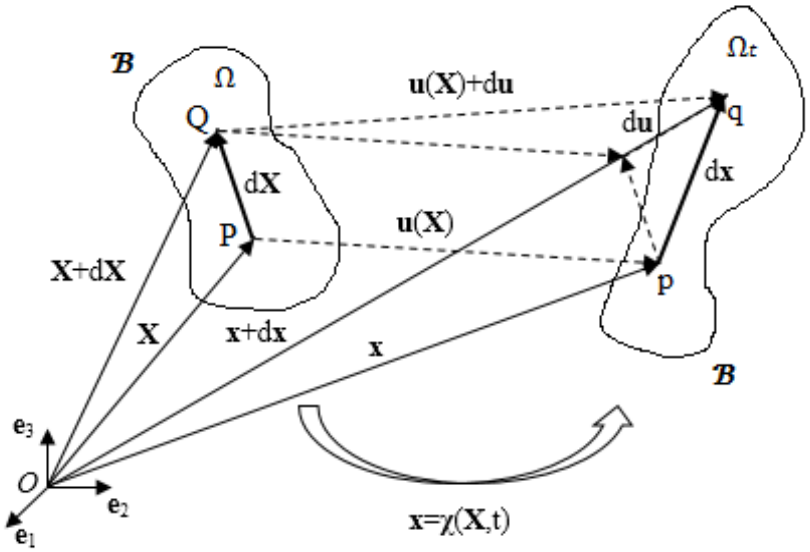

Fig. 8. The motion $\mathbf{x} = \boldsymbol{\chi}(\mathbf{X}, t)$ of the line element d**X** in the material configuration resulting in a line element d**x** in the spatial configuration

In three-dimensional analysis deformation gradient is a tensor of nine entries and it characterizes the motion around the chosen particle (Ogden, 1997, Holzapfel, 2000). It can also be described in terms of displacement, were $\mathbf{u} = \mathbf{x} - \mathbf{X}$, and then the deformation gradient is as follows:

$$\mathbf{F} = \frac{\partial}{\partial \mathbf{X}}(\mathbf{X} + \mathbf{u}) = \frac{\partial \mathbf{X}}{\partial \mathbf{X}} + \frac{\partial \mathbf{u}}{\partial \mathbf{X}} = \mathbf{I} + \frac{\partial \mathbf{u}}{\partial \mathbf{X}} \tag{3}$$

were **I** is the identity tensor.

Determinant of the deformation gradient $J = \det\mathbf{F}$ defines the change in volume as follows (Ogden, 1997, Holzapfel, 2000):

$$dv = JdV \tag{4}$$

where the deformations of infinitesimal volume element in material configuration dV is transformed into the infinitesimal volume element in spatial configuration $\mathrm{d}v$. Due to the fact that material volume cannot be negative $J > 0$. $J = 1$ corresponds to material that preserves its volume.

The oriented surface element of material configuration can be defined as $d\mathbf{A} = dA\mathbf{N}$ and of the spatial configuration as $d\mathbf{a} = da\mathbf{n}$, where **N** and **n** are the normal unit vectors in different configurations. These elements are related by Nanson's formula (Holzapfel, 2000), as follows:

$$d\mathbf{a} = J\mathbf{F}^{-\mathrm{T}}d\mathbf{A} \tag{5}$$

If the rigid translations are present, the deformation gradient will be equal to identity $\mathbf{F} = \mathbf{I}$. In case of rotations, the deformation gradient becomes non-equal to identity $\mathbf{F} \neq \mathbf{I}$, although no strains or stresses are present. For this reason the polar decomposition concept is introduced, with the left polar decomposition usually used, which is as follows (Holzapfel, 2000):

$$\mathbf{F} = \mathbf{RU} \tag{6}$$

were $\mathbf{R}$ corresponds to the rotation tensor and $\mathbf{U} = \mathbf{U}^{\mathrm{T}}$ corresponds to the right stretch tensor. From here we can introduce the strain measure as follows (Ogden, 1997, Holzapfel, 2000):

$$\mathbf{F}^{\mathrm{T}}\mathbf{F} = (\mathbf{RU})^{\mathrm{T}}\mathbf{RU} = \mathbf{U}^{\mathrm{T}}\mathbf{R}^{\mathrm{T}}\mathbf{RU} \tag{7}$$

Here $\mathbf{R}^{\mathrm{T}}$ is the inverse of $\mathbf{R}$ and then $\mathbf{R}^{\mathrm{T}}\mathbf{R} = \mathbf{R}^{-1}\mathbf{R} = \mathbf{I}$. Therefore, the $\mathbf{F}^{\mathrm{T}}\mathbf{F}$ is as follows:

$$\mathbf{F}^{\mathrm{T}}\mathbf{F} = \mathbf{U}^{\mathrm{T}}\mathbf{U} = \mathbf{U}^{2} \tag{8}$$

From the Eq. (8), we see that the rotation is not considered and we are only left with the tensor representing the squared stretches.

Now the strain measures in the material configuration can be defined. The right Cauchy-Green deformation tensor is as follows (Holzapfel, 2000):

$$\mathbf{C} = \mathbf{F}^{\mathrm{T}}\mathbf{F} \tag{9}$$

where $\mathbf{C}$ only accounts for deformations without rotations, which are the true causes of stress and strains.

To measure strains objectively, the invariants are introduced, which are scalar valued functions that do not depend on the choice of the coordinate system. The invariants of the elastic material are as follows:

$$I_1 = \mathrm{tr}\mathbf{C}, \qquad I_2 = \frac{1}{2}[(\mathrm{tr}\mathbf{C})^2 - \mathrm{tr}\mathbf{C}^2], \qquad I_3 = \det\mathbf{C} \tag{10}$$

The first invariant describes the stretch in the principal directions; second invariant describes changes in orientation, while the third invariant describes volumetric changes. In case of anisotropy, additional invariants must be introduced.

2.1.1.2 Mechanical stresses

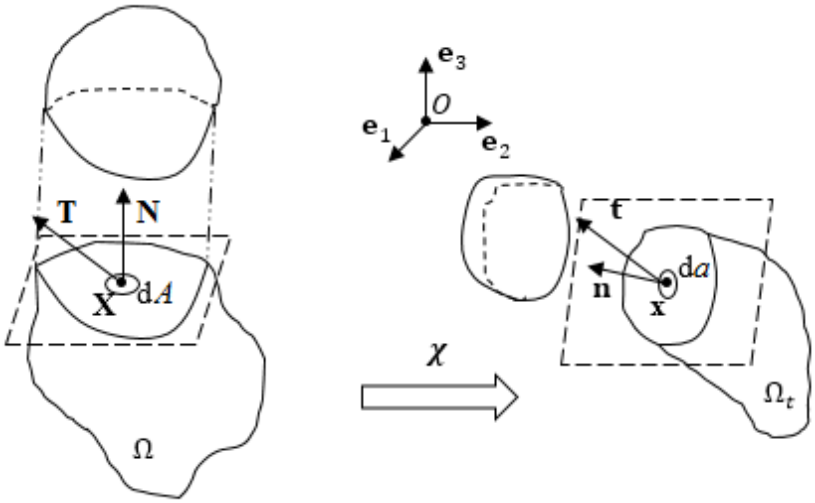

Fig. 9. Traction vectors defining internal forces on the infinitesimal area and the outward normal in the reference **T**, **N** and in current **t**, **n** configurations, respectively

Let us consider a body in the material and spatial configurations, Ω and Ω_t, respectively, which is subjected to the distributed forces: the external forces that acts on the outer boundary surface and the internal forces acting on an imaginary surface within the body (Fig. 9). The infinitesimal force d**f** acting on both infinitesimal surfaces dA and da for each surface element is as follows (Ogden, 1997, Holzapfel, 2000):

$$d\mathbf{f} = \mathbf{t}(\mathbf{x}, t, \mathbf{n})da = \mathbf{T}(\mathbf{X}, t, \mathbf{N})dA \tag{11}$$

where **t** is the traction vector (Cauchy or true) defined in the spatial configuration, acting on infinitesimal surface area da with outward normal vector **n**. **T** is the traction vector (first Piola-Kirchhoff or nominal) defined in the reference configuration pointing to the same direction as traction vector **t** and acting on infinitesimal surface area dA with with outward normal vector **N**.

From the Cauchy stress theorem, there exist unique fields **σ** and **P** so that if traction vectors depend on the outward normal, they must be linear with respect to outward normal as follows (Holzapfel, 2000):

$$\begin{cases} \mathbf{t}(\mathbf{x}, t, \mathbf{n}) = \boldsymbol{\sigma}(\mathbf{x}, t)\mathbf{n} \\ \mathbf{T}(\mathbf{X}, t, \mathbf{N}) = \mathbf{P}(\mathbf{X}, t)\mathbf{N} \end{cases} \tag{12}$$

where **σ** is the Cauchy stress tensor, **P** is the first Piola-Kirchhoff stress tensor. The relation between **σ** and **P** can be written as follows (Holzapfel, 2000):

$$\boldsymbol{\sigma}(\mathbf{x}, t)\mathbf{n}da = \mathbf{P}(\mathbf{X}, t)\mathbf{N}dA \tag{13}$$

Now using the Nanson's formula the first Piola-Kirchhoff stress tensor can be written as follows (Holzapfel, 2000):

$$\mathbf{P} = J\boldsymbol{\sigma}\mathbf{F}^{-\mathrm{T}} \tag{14}$$

In the numerical procedures for solids, usually, a second Piola-Kirchoff stress tensor **S** is used, which in terms of **P** is as follows (Holzapfel, 2000):

$$\mathbf{S} = \mathbf{F}^{-1}\mathbf{P} \tag{15}$$

2.1.1.3 Fundamental conservation principles

In our work following fundamental conservation, principles of continuum mechanics are used:

- Conservation of mass
- Conservation of linear momentum
- Balance of mechanical energy

The conservation of mass is introduced in chapter 2.1.1.3.1, conservation of momentum in chapter 2.1.1.3.2 and the balance of mechanical energy in chapter 2.1.1.3.3.

2.1.1.3.1 Conservation of mass

The continuous body $\boldsymbol{\mathcal{B}}$ is composed of continuous set of points that possess the mass. At time, $t = 0$ body $\boldsymbol{\mathcal{B}}$ encompasses the domain Ω, with its surface boundary Γ. If we assume that domain Ω is a closed system, then during the motion, this closed system may deform, however the mass of the closed system remains constant and only the energy can be transferred throughout the boundary Γ. In contrast, if we fix the domain of interest in the space, then we are left with the control volume Ω_V and the control surface Γ_V, which during the motion stays fixed and mass and energy can both enter and leave the system.

Considering a closed system the mass should always be a positive number $m > 0$ and the conservation of mass for all times t than can be written as follows:

$$m(\Omega_0) = m(\Omega) > 0 \tag{16}$$

Mass in the material configuration is a function of material density $\rho_0(\mathbf{X})$ and material volume dV, while spatial mass density is a function of spatial mass density $\rho(\mathbf{x}, t)$ and spatial volume dv. Therefore, we may write (Holzapfel, 2000):

$$\rho_0(\mathbf{X})dV = \rho(\mathbf{x}, t)dv > 0 \tag{17}$$

Eq. (17) means that during the motion if the volume of the infinitesimal volume element shrinks or increases, the density increases or decreases, respectively. We may also write it in the global form as follows:

$$m = \int_{\Omega} \rho_0(\mathbf{X}) dV = \int_{\Omega_t} \rho(\mathbf{x}, t) dv \tag{18}$$

Eq. (18) means that the mass of the whole domain Ω should be the same as the mass of the domain Ω_t, which resulted after motion. Based on the Eq. (4) we may write a continuity mass equation in the material description in local form, which is used in solid mechanics:

$$\rho_0(\mathbf{X}) = \rho(\mathbf{x}, t) J(\mathbf{X}, t) \tag{19}$$

The rate form in the material description than is as follows (Holzapfel, 2000):

$$\frac{\partial \rho_0(\mathbf{X})}{\partial t} = 0 \tag{20}$$

In the spatial description, based on the equation (20) we can write:

$$\frac{D}{Dt}(\rho(\mathbf{x}, t) J(\mathbf{X}, t)) = 0 \tag{21}$$

From Eq. (21) and also based on the (Holzapfel, 2000) where it is shown that $\frac{\partial J}{\partial t} = J \mathrm{div}\mathbf{v}$, we obtain:

$$\begin{aligned} \frac{D\big(\rho(\mathbf{x}, t) J(\mathbf{X}, t)\big)}{Dt} &= \frac{\partial \rho(\mathbf{x}, t)}{\partial t} J(\mathbf{X}, t) + \rho(\mathbf{x}, \mathrm{t}) \frac{\partial J(\mathbf{X}, t)}{\partial t} \\ &= J(\mathbf{X}, t) \left(\frac{\partial \rho(\mathbf{x}, t)}{\partial t} + \rho(\mathbf{x}, t) \mathrm{div}\mathbf{v}(\mathbf{x}, t) \right) = 0 \end{aligned} \tag{22}$$

from the Eq. (21) and based on the material time derivative of the spatial density function, we can obtain the rate form of continuity mass equation in the spatial description in the local form, which is used in fluid dynamics:

$$\frac{\partial\big(\rho(\mathbf{x}, t)\big)}{\partial t} + \mathrm{div}\left(\frac{\partial \rho(\mathbf{x}, t)}{\partial t} \mathbf{v}(\mathbf{x}, t) \right) = 0 \tag{23}$$

For the incompressible continuum, body there is no change in density with respect to time so $\frac{\partial \rho(\mathbf{x}, t)}{\partial t} = 0$ and therefore, the continuity equation in a spatial form for the incompressible body is as follows:

$$\mathrm{div}\mathbf{v}(\mathbf{x}, t) = 0 \tag{24}$$

2.1.1.3.2 Conservation of linear momentum

Only the balance of the linear momentum is considered here, as the constitutive equations of the blood and of the artery wall considers the symmetry condition on the

Cauchy stress tensor, which implies that the balance of angular momentum is also satisfied (Tricerri, 2014).

The total linear momentum **L** is defined as follows (Holzapfel, 2000):

$$\mathbf{L}(t) = \int_{\Omega_t} \rho(\mathbf{x}, t)\mathbf{v}(\mathbf{x}, t)dv = \int_{\Omega} \rho_0(\mathbf{X})\mathbf{V}(\mathbf{X}, t)dV \tag{25}$$

where **V** is the velocity in the material configuration.

The balance of the linear momentum can be written as follows (Holzapfel, 2000):

$$\dot{\mathbf{L}}(t) = \frac{D}{Dt}\int_{\Omega_t} \rho(\mathbf{x}, t)\mathbf{v}(\mathbf{x}, t)dv = \frac{D}{Dt}\int_{\Omega} \rho_0(\mathbf{X})\mathbf{V}(\mathbf{X}, t)dV = \boldsymbol{\mathcal{F}}(t) \tag{26}$$

Let us assume that a spatial body force, $\mathbf{b}_{\boldsymbol{\mathcal{F}}} = \mathbf{b}_{\boldsymbol{\mathcal{F}}}(\mathbf{x}, t)$, which acts on the elementary volume dv and the surface traction, $\mathbf{t} = \mathbf{t}(\mathbf{x}, t, \mathbf{n})$, which acts on the surface Γ affects the continuous body $\boldsymbol{\mathcal{B}}$. In this case, the force $\boldsymbol{\mathcal{F}}(t)$ is as follows:

$$\boldsymbol{\mathcal{F}}(t) = \int_{\Gamma} \mathbf{t}ds + \int_{\Omega_t} \mathbf{b}_{\boldsymbol{\mathcal{F}}}dv \tag{27}$$

Then the balance of linear momentum based on Eq. (26) and Eq. (27) is as follows:

$$\frac{D}{Dt}\int_{\Omega_t} \rho\mathbf{v}dv = \int_{\Gamma} \mathbf{t}ds + \int_{\Omega_t} \mathbf{b}_{\boldsymbol{\mathcal{F}}}dv \tag{28}$$

Integrating Eq. (12) and applying divergence theorem we obtain:

$$\int_{\Gamma} \mathbf{t}(\mathbf{x}, t, \mathbf{n})ds = \int_{\Gamma} \boldsymbol{\sigma}(\mathbf{x}, t)\mathbf{n}ds = \int_{\Omega_t} \mathrm{div}\boldsymbol{\sigma}(\mathbf{x}, t)dv \tag{29}$$

As the integral in Eq. (28) holds for any volume therefore, we can write the local form of Cauchy's first equation of motion in the spatial description, which is extensively used in fluid mechanics, from Eq. (28)(29) as follows:

$$\rho\frac{D}{Dt}\mathbf{v} - \mathrm{div}\boldsymbol{\sigma} - \mathbf{b}_{\boldsymbol{\mathcal{F}}} = \mathbf{0} \tag{30}$$

were $\frac{Df}{Dt} = \frac{\partial f}{\partial t} + \mathbf{v} \cdot \nabla f$ is the material time derivative and f is an arbitrary function. When inserting the result of the material derivative into Eq. (30) and in case of incompressible continuum body following equation is obtained:

$$\rho\left(\frac{\partial \mathbf{v}}{\partial t} + (\mathbf{v} \cdot \nabla)\mathbf{v}\right) - \mathrm{div}\boldsymbol{\sigma} - \mathbf{b}_{\boldsymbol{\mathcal{F}}} = \mathbf{0} \tag{31}$$

For the solid mechanics the Cauchy's first equation of motion is usually written in the material description (Holzapfel, 2000) in terms of the material displacement Eq. (30) is as follows:

$$\rho_0 \frac{D}{Dt^2} \mathbf{U}_d{}^2 - \mathrm{Div}\mathbf{P} - \mathbf{B}_{\mathcal{F}} = \mathbf{0} \tag{32}$$

where $\mathbf{U}_d$ is the material displacement field, Div is the divergence operator in the material description, $\mathbf{B}_{\mathcal{F}}$ is the body forces acting on the material configuration.

2.1.1.3.3 Balance of mechanical energy

The rate of internal mechanical work done by the stress field is as follows (Holzapfel, 2000):

$$\mathcal{P}_{\mathrm{int}}(t) = \int_{\Omega} \boldsymbol{\sigma} : \mathbf{d} dv \tag{33}$$

where $\mathbf{d} = \frac{1}{2}(\mathrm{grad}\mathbf{v} + \mathrm{grad}^{\mathrm{T}}\mathbf{v})$ is the rate of deformation (Holzapfel, 2000), and : is a double contraction operation, which takes two tensors and outputs a scalar value.

The kinetic energy of the continuum body is as follows (Ogden, 1997, Holzapfel, 2000):

$$\mathcal{K}(t) = \int_{\Omega} \frac{1}{2} \rho \mathbf{v}^2 dv \tag{34}$$

The rate of external mechanical work is as follows (Holzapfel, 2000):

$$\mathcal{P}_{\mathrm{ext}}(t) = \int_{\Gamma} \mathbf{t} \cdot \mathbf{v} ds + \int_{\Omega} \mathbf{b} \cdot \mathbf{v} dv \tag{35}$$

The internal energy (thermodynamic state variable), which is the sum of all the microscopic internal energy u_v per unit current volume integrated over the domain Ω, is as follows (Ogden, 1997, Holzapfel, 2000):

$$\mathcal{U}(t) = \int_{\Omega} \mathrm{u}_v dv \tag{36}$$

in addition, since only the mechanical energy is considered the internal mechanical work done by the stress field is equal to the rate of internal energy as follows:

$$\mathcal{P}_{\mathrm{int}}(t) = \frac{D}{Dt} \mathcal{U}(t) \tag{37}$$

The balance of mechanical energy in terms of internal energy is then as follows (Ogden, 1997, Holzapfel, 2000):

$$\frac{D}{Dt} \mathcal{K}(t) + \frac{D}{Dt} \mathcal{U}(t) = \mathcal{P}_{\mathrm{ext}}(t) \tag{38}$$

Explicit form of Eq. (38) in the material description is as follows (Holzapfel, 2000):

$$\frac{D}{Dt}\int_{\Omega_0}\frac{1}{2}\rho_0\mathbf{V}^2dV+\frac{D}{Dt}\int_{\Omega_0}\mathbf{P}:\mathbf{F}dV=\int_{\Gamma}\mathbf{T}\cdot\mathbf{V}dS+\int_{\Omega_0}\mathbf{B}_{\mathcal{F}}\cdot\mathbf{V}dV \tag{39}$$

alternatively, $\frac{D}{Dt}\int_{\Omega_0}\mathbf{P}:\mathbf{F}dV=\int_{\Omega_0}\mathbf{P}:\dot{\mathbf{F}}dV$. In this case the work conjugate and the real physical rate of internal mechanical work per unit reference volume is $\mathrm{w}_{\mathrm{int}}(t)=\mathbf{P}:\dot{\mathbf{F}}$ (Holzapfel, 2000).

Based on the Clausius-Planck inequality and ignoring the thermal effects the internal dissipation is as follows (Ogden, 1997, Holzapfel, 2000):

$$\mathcal{D}_{\mathrm{int}}=\mathbf{P}:\dot{\mathbf{F}}-\dot{\Psi}\geq 0 \tag{40}$$

where Ψ is the SEF and $\dot{\Psi}=\dot{\mathrm{u}}_v$.

For a reversible process, Eq. (40) is as follows:

$$\mathcal{D}_{\mathrm{int}}=\mathbf{P}:\dot{\mathbf{F}}-\dot{\Psi}=0 \tag{41}$$

As for the ideal hyperelastic material the SEF depends only on the deformation gradient (Holzapfel, 2000) and based on (41) the constitutive relation can be expressed as follows:

$$\mathbf{P}=\frac{\partial\Psi}{\partial\mathbf{F}} \tag{42}$$

2.1.2 Arbitrary Lagrangian-Eulerian formulation and the fluid-structure interaction (FSI) method

Naturally, the governing equations of fluid flow are formulated in the spatial (Eulerian) description. It could be thought as if the observer is watching the flow from a fixed location. The material (Lagrangian) description is usually used when dealing with solid materials. This can be though as if the observer is moving together with the material point. One description, either the material or the spatial is not optimal for the entire FSI problem domain (Souli et al., 2013) as the fluid-solid interface cannot be tracked. The use of material description for the fluid domain is limited as it can only handle small deformations, while the use of spatial description for the solid domain is not optimal in terms of the loss in accuracy. Notably, arbitrary Lagrangian-Eulerian (ALE) formulation is reliable and is applied as a framework to solve various FSI problems (Annerel et al., 2014, Song et al., 2017). In the ALE formulation in addition to spatial and material descriptions, additional arbitrary mesh description is introduced allowing to track the fluid-solid interface. The scheme showing the mappings between different descriptions together with the interface between solid and fluid and their respective notations are shown in Fig. 10.

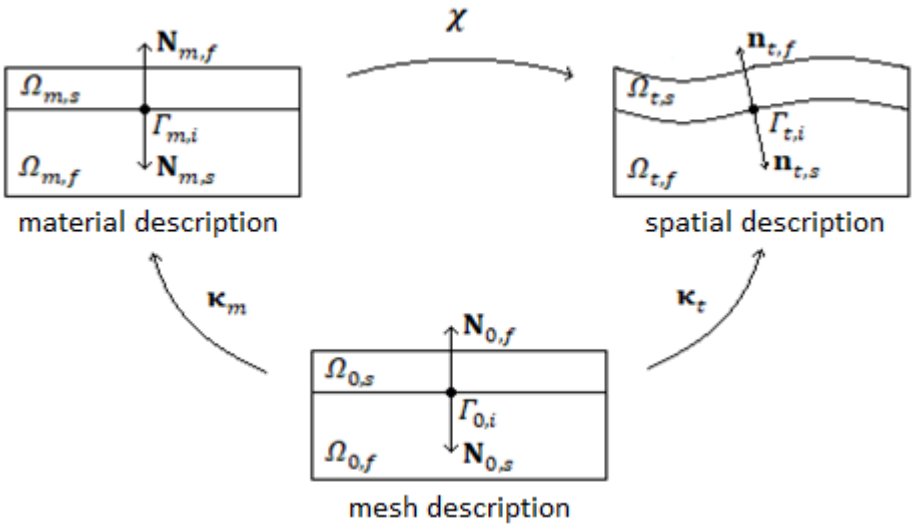

Fig. 10. Different descriptions used in the ALE framework. Figure adapted from Fig. 2 in (Misiulis et al., 2018)

$\boldsymbol{\kappa}_t$ maps from the mesh description, in which the motion of material particles is evaluated in terms of the arbitrarily moving computational mesh, to the spatial description where the motion of material particles is evaluated in terms of the initial, fixed computational mesh. $\boldsymbol{\kappa}_m$ maps from the mesh description, to the material description where the motion of material particles is evaluated in terms of the initial, fixed computational mesh. $\boldsymbol{\chi}$ maps from the material description to the spatial description. In case of ALE formulation, the material time derivative is as follows:

$$\frac{Df}{Dt} = \frac{\partial f}{\partial t}\bigg|_{\boldsymbol{\chi}} + \mathbf{c} \cdot \nabla f \tag{43}$$

were $|_{\boldsymbol{\chi}}$ means holding the $\boldsymbol{\chi}$ fixed, the relative convective velocity between material and mesh descriptions is $\mathbf{c} = \mathbf{v} - \hat{\mathbf{v}}$, where $\mathbf{v}$ is the material velocity and $\hat{\mathbf{v}}$ is the mesh velocity.

The governing continuity Eq. (24) and linear momentum equations Eq. (31) in case of ALE formulation is rewritten as follows:

- Continuity (mass conservation) remains unchanged:

$$\mathrm{div}\mathbf{v}(\mathbf{x}, t) = 0 \tag{44}$$

- Momentum (conservation of linear momentum):

$$\rho\left(\frac{\partial \mathbf{v}}{\partial t} + (\mathbf{c} \cdot \nabla)\mathbf{v}\right) - \mathrm{div}\boldsymbol{\sigma} - \mathbf{b}_{\mathcal{F}} = \mathbf{0} \tag{45}$$

The boundary between the artery wall and blood is treated as a fluid-structure interface. The interaction between fluid and wall happens at the coupling interface Γ_i

(shown in Fig. 10). Total surface force $\mathbf{f}_f = \mathbf{n}_f \boldsymbol{\sigma}_f$ exerted by the incompressible fluid on the boundary of the wall must be equal to the negative reaction surface force $\mathbf{f}_s = -\mathbf{n}_s \boldsymbol{\sigma}_s$, which is exerted on the fluid. The coupling on the interface boundary Γ_i is then calculated as follows (de Villiers et al., 2017):

$$\mathbf{n}_s \boldsymbol{\sigma}_s + \mathbf{n}_f \boldsymbol{\sigma}_f = \mathbf{0} \text{ on } \Gamma_{0,i} \tag{46}$$

where $\mathbf{n}_f$ is the normal to the fluid boundary, $\mathbf{n}_s$ is the normal to the solid boundary. In a material description based on Eq. (14), Eq. (46) can be written as follows:

$$\mathbf{N}_s \mathbf{P}_s + \mathbf{n}_f J \boldsymbol{\sigma}_f \mathbf{F}^{-\mathrm{T}} = \mathbf{0} \text{ on } \Gamma_{0,i} \tag{47}$$

Fluid domain is affected by a moving wall through the structural velocities calculated as follows:

$$\mathbf{v}_f = \mathbf{v}_s = \frac{\partial \mathbf{U}_d}{\partial t} \text{ on } \Gamma_{0,i} \tag{48}$$

where $\mathbf{v}_s$ is the wall velocity.

2.1.3 Basic principles of finite element method

Partial differential equations are usually used to describe physical phenomena in a mathematical framework, which further can be manipulated to obtain the quantitative solution of the problem. The majority of the problems described by partial differential equation cannot be solved analytically and therefore requires other solving techniques. To cope with this problem the discretization techniques are developed. In this sense, the continuous field is discretized into elements in which the partial differential equations are approximated with numerical model equations, which are solved using numerical methods.

The finite element method is composed of several procedures of which the idea is to arrive at the algebraic system of equations, which can then be solved by numerical methods (Kaltenbacher, 2015):

- The strong formulation of partial differential equations governing the phenomena in question with provided boundary conditions are multiplied by arbitrary test functions.
- Resultant is further integrated over the whole simulation domain.
- Integration by parts is further carried on one of the terms, and by doing so the weak formulation is realized.
- Next step is the discretization, which for finite elements is the Galerkin approximation method, and this procedure results in the algebraic system of equations.

Mentioned steps are covered in detail below.

The strong formulation of a scalar $u(\mathbf{z}, t)$ diffusion partial differential equation $\frac{\partial u}{\partial t} = c\nabla \cdot \nabla u + f$ with a constant parameter $c = 1$ and added source term $f(\mathbf{z}, t)$ with initial conditions are as follows:

$$\begin{cases} \dfrac{\partial u}{\partial t} = \nabla \cdot \nabla u + f & \text{in } \Omega \\ u = u_D & \text{on } \Gamma_D \\ \dfrac{\partial u}{\partial \mathbf{n}} = u_N & \text{on } \Gamma_N \\ u(\mathbf{z}, 0) = u_0 & \mathbf{z} \in \Omega \end{cases} \tag{49}$$

where Ω domain of simulation without boundaries $\Gamma_D \cup \Gamma_N$, Γ_d denotes the boundary with prescribed Dirichlet boundary condition, Γ_N denotes the prescribed Neumann boundary condition.

We multiply the strong formulation of partial differential equation by a test function:

$$w\left(\frac{\partial u}{\partial t} - \nabla \cdot \nabla u - f\right) = 0 \tag{50}$$

and integrate over domain:

$$\int_\Omega w\left(\frac{\partial u}{\partial t} - \nabla \cdot \nabla u - f\right) \mathrm{d}\Omega = 0 \tag{51}$$

The integration by parts is performed by applying divergence theorem on the above equation and the weak formulation is obtained as follows:

$$\int_\Omega w\frac{\partial u}{\partial t}\mathrm{d}\Omega + \int_\Omega \nabla w \cdot \nabla u \mathrm{d}\Omega = \int_\Omega wf\mathrm{d}\Omega + \int_{\Gamma_n} w\frac{\partial u}{\partial \mathbf{n}}\mathrm{d}\Gamma \tag{52}$$

The Neumann boundary condition is now incorporated in the weak expression, and this boundary condition can now be called the natural boundary condition. Dirichlet boundary condition is called the essential boundary condition, as it must be declared in addition to the weak formulation:

$$u = u_D \text{ on } \Gamma_D \tag{53}$$

Weak formulation and the strong formulation are equivalent, if the scalar field u is sufficiently smooth.

The weak formulation is further discretized and the Galerkin method is applied element-wise. The u has the domain component, lets declare it as v, of which values are to be found and the given boundary values, lets declare them as u_b. We define scalar field and test functions in terms of shape functions by the following ansatz:

$$u_b = \sum_{i=1}^{n_{eD}} N_i u_{Di} = \mathbf{N}_b \mathbf{u}_b \tag{54}$$

$$v = \sum_{i=1}^{n_e} N_i v_i = \mathbf{N}_b \mathbf{v}_b \tag{55}$$

$$w = \sum_{i=1}^{n_e} N_i \varphi_i = \mathbf{N}_a \boldsymbol{\varphi}_a \tag{56}$$

where i is the number of nodes, a, b is used to separate vectors of dependent variable and test function, n_e is the number of unknowns without Dirichlet boundary condition, n_{eD} is the number of unknowns with Dirichlet boundary condition, N_i, N_j are the shape functions, u_{Di}, v_i, φ_i are prescribed functions.

Now the weak formulation with boundary conditions can be written as follows:

$$\begin{aligned} \int_\Omega \left(\mathbf{N}_a \boldsymbol{\varphi}_a \frac{\partial}{\partial t} \mathbf{N}_b \mathbf{v}_b\right) \mathrm{d}\Omega + \int_\Omega \nabla(\mathbf{N}_a \boldsymbol{\varphi}_a) \cdot \nabla(\mathbf{N}_b \mathbf{v}_b) \mathrm{d}\Omega \\ + \int_\Omega \left(\mathbf{N}_a \boldsymbol{\varphi}_a \frac{\partial}{\partial t} \mathbf{N}_b \mathbf{u}_b\right) \mathrm{d}\Omega \\ + \int_\Omega \nabla(\mathbf{N}_a \boldsymbol{\varphi}_a) \cdot \nabla(\mathbf{N}_b \mathbf{u}_b) \mathrm{d}\Omega \\ = \int_\Omega \mathbf{N}_a \boldsymbol{\varphi}_a f \mathrm{d}\Omega + \int_{\Gamma_n} \mathbf{N}_a \boldsymbol{\varphi}_a \frac{\partial u}{\partial \mathbf{n}} \mathrm{d}\Gamma \end{aligned} \tag{57}$$

The constants can now be brought forward and then:

$$\begin{aligned} \boldsymbol{\varphi}_a \Bigg(\left(\int_\Omega \mathbf{N}_a \mathbf{N}_b \mathrm{d}\Omega\right) \frac{\partial}{\partial t} \mathbf{v}_b + \left(\int_\Omega (\nabla \mathbf{N}_a \cdot \nabla \mathbf{N}_b) \mathrm{d}\Omega\right) \mathbf{v}_b \\ + \left(\int_\Omega \mathbf{N}_a \mathbf{N}_b \mathrm{d}\Omega\right) \frac{\partial}{\partial t} \mathbf{u}_b + \left(\int_\Omega (\nabla \mathbf{N}_a \cdot \nabla \mathbf{N}_b) \mathrm{d}\Omega\right) \mathbf{u}_b \\ - \int_\Omega \mathbf{N}_a f \mathrm{d}\Omega - \int_\Gamma \mathbf{N}_a \frac{\partial u}{\partial \mathbf{n}} \mathrm{d}\Gamma \Bigg) = 0 \end{aligned} \tag{58}$$

Obtained equations are used to find coefficients φ_a, and here for each i following equations must be solved:

$$\begin{aligned} \left(\int_\Omega \mathbf{N}_a \mathbf{N}_b \mathrm{d}\Omega\right) \frac{\partial}{\partial t} \mathbf{v}_b + \left(\int_\Omega (\nabla \mathbf{N}_a \cdot \nabla \mathbf{N}_b) \mathrm{d}\Omega\right) \mathbf{v}_b \\ + \left(\int_\Omega \mathbf{N}_a \mathbf{N}_b \mathrm{d}\Omega\right) \frac{\partial}{\partial t} \mathbf{u}_b + \left(\int_\Omega (\nabla \mathbf{N}_a \cdot \nabla \mathbf{N}_b) \mathrm{d}\Omega\right) \mathbf{u}_b \\ - \int_\Omega \mathbf{N}_a f \mathrm{d}\Omega - \int_\Gamma \mathbf{N}_a \frac{\partial u}{\partial \mathbf{n}} \mathrm{d}\Gamma = 0 \end{aligned} \tag{59}$$

Eq. (59) can be written in the matrix form, which can be solved using numerical methods:

$$\mathbf{M}\dot{\mathbf{U}}_n + \mathbf{K}\mathbf{U}_n = \mathbf{R}_p \tag{60}$$

where $\mathbf{M}$ is the mass matrix, $\dot{\mathbf{U}}_n, \mathbf{U}_n$ are the nodal unknowns, $\mathbf{K}$ is the stiffness matrix, and $\mathbf{R}_p$ is the externally applied nodal point loads. The mass matrix can then be written as follows:

$$\mathbf{M} = M_{ab} \qquad M_{ab} = \int_\Omega N_a N_b \,\mathrm{d}\Omega \quad 1 \le a, b \le n_e \tag{61}$$

stiffness matrix can be written as follows:

$$\mathbf{K} = M_{ab} \qquad K_{ab} = \int_\Omega (\nabla N_a \cdot \nabla N_b)\mathrm{d}\Omega \quad 1 \le a, b \le n_e \tag{62}$$

and the externally applied nodal point loads can then be written as follows:

$$\begin{gathered}\mathbf{R}_p = R_a \\ R_a = \int_\Omega N_i f \,\mathrm{d}\Omega + \int_\Gamma N_i \frac{\partial u}{\partial \mathbf{n}} \mathrm{d}\Gamma \\ - \sum_{j=1}^{n_{eD}} \left(\int_\Omega \left(\nabla N_i \cdot \nabla N_j\right) \mathrm{d}\Omega \right) u_{Dj} \\ - \sum_{j=1}^{n_{eD}} \left(\int_\Omega N_i N_j \,\mathrm{d}\Omega \right) \frac{u_{Dj}}{\partial t} \\ 1 \le a \le n_e \quad 1 \le b \le n_{eD}\end{gathered} \tag{63}$$

The names of matrices are common to the structural mechanics as the finite element method was first developed for such problems, however now it can be used for a vast majority of different problems.

2.2 Numerical model of the blood flow in the patient-specific OA

In order to perform a clinically relevant FSI analysis of the patient-specific OA several procedures have to be considered:

- the constitutive material model for the artery wall and for the blood,
- the reconstruction of the patient-specific artery from the medical imaging data,
- the incorporation of the prestress,
- the definition of governing equations and boundary conditions.

2.2.1 Geometry reconstruction

Reconstruction of a patient-specific volume of an artery from MRI scan data is a non-trivial problem. Usually, a large number of elements represent the reconstructed

geometry, and depending on the structure, many elements may be of a bad quality, and eventually the direct use in numerical simulation can produce unreliable results, so further steps need to be taken in order to overcome this problem. One approach is based on smoothening out the obtained geometry while keeping the resulting volume very close to the initial volume (Taubin, 1995). We used another approach, which is based on the reconstruction of the artery by using a centerline as a parameterized curve with a varying artery wall thickness described by a maximum inscribed sphere radius, which is defined in detail in (Antiga, 2002). Our procedure of artery geometry reconstruction is as follows:

The reconstruction of artery volume from the MRI scan data is performed using the "VMTK 1.3" software (Antiga et al., 2008), which uses the level set method to generate image (Gibou et al., 2018). Fast marching initialization is used for the level set method, where a number of seed points and source points needs to be selected for the artery geometry extraction (Forcadel et al., 2008). The marching cubes algorithm (Newman et al., 2006) is used on the obtained image to generate the artery surface.

Centerline of an artery is computed using "VMTK 1.3" software (Antiga, 2002). A relatively large database of points representing the centerline is usually obtained in comparison with the artery length. Smoothing is performed in order to prevent wrinkle formation by increasing the maximum allowed distance between the generated curve and the sequence of points to be equal to 0.01 m. The curve is generated by the internal COMSOL Multiphysics® interpolation curve procedure.

Finally, a smooth geometry shape of the lumen area and vessel wall is generated from the smoothed out centerline with COMSOL CAD by using the internal sweep procedure (Anon. 2015). Sweep procedure is used to traverse the initial artery configuration represented in a 2D plane, by incorporating the obtained internal lumen radius parametrization, throughout a smoothed centerline.

The scaling factor of the sweep procedure is defined as a function of the maximum inscribed sphere radius, which allows generation of a patient-specific lumen radius along the artery centerline.

2.2.2 Prestress method

The reconstruction of the artery from the medical imaging data obtained *in vivo* provides the material configuration geometry, which is stress-free as during the geometry reconstruction the stresses are not reconstructed, however, *in vivo* material configuration is subjected to loads (Humphrey et al., 2002) and residual stresses (Chuong et al., 1986). The methods used to incorporate the residual stresses and physiological loadings are called the prestressing methods. Considering arteries, the large strain analysis are carried out, and the stresses are usually not additive (Maas et al., 2016), and therefore numerical methods are required to account for the prestress. There are several numerical methods proposed to evaluate the prestress. (Hsu et al., 2011) proposed a method, which allows starting the FSI problems from equilibrium stress conditions, however, the prestrain is not accumulated and therefore the constitutive material model should start from the loaded configuration. (Gee et al., 2009) proposed a prestress method, which was further generalized by (Weisbecker et

al., 2014) and called the generalized prestress algorithm (GPA). In the GPA, the incremental update of displacement field is replaced with the incremental change in deformation gradient. The increment of the deformation gradient is as follows:

$$\Delta\mathbf{F} = \mathbf{I} + \frac{\partial \Delta\mathbf{u}}{\partial \mathbf{x}_t} \tag{64}$$

were $\mathbf{x}_t$ corresponds to the configuration affected by the history prestrain gradient $\mathbf{F}_t$, and $\Delta\mathbf{u}$ corresponds to the displacement from the $\mathbf{x}_t$ configuration. Current deformation gradient, $\mathbf{F}_{t+1}$, is multiplicatively decomposed into history prestrain gradient $\mathbf{F}_t$ and increment in deformation gradient $\Delta\mathbf{F}$ as follows:

$$\mathbf{F}_{t+1} = \Delta\mathbf{F}\mathbf{F}_t \tag{65}$$

The algorithm of the GPA is given in (Weisbecker et al., 2014). As $\Delta\mathbf{u} \to \mathbf{0}$ the $\mathbf{x}_t$ configuration approaches material stress-free configuration $\mathbf{X}$ obtained from the medical imaging and the prestrain kept in the history $\mathbf{F}_t$ can now be declared to be the prestrain gradient as follows $\mathbf{F}_p = \mathbf{F}_t$ and further forward analysis can be carried out with the deformation gradient defined as follows:

$$\mathbf{F} = \mathbf{F}_{arb}\mathbf{F}_p \tag{66}$$

were $\mathbf{F}_{arb}$ is an arbitrary deformation gradient obtained during the forward analysis. GPA method allows using the material models that can start from the stress-free configuration, as prestrain, which defines the prestress via hyperelastic constitutive artery wall model, is stored in the history variable.

2.2.3 Artery wall dynamics:

2.2.3.1 Governing equations

It was assumed that no volumetric forces are present and the equation of motion for the artery wall during dynamic analysis in the material description with omitted volumetric forces based on the Eq. (32) is as follows:

$$\rho_0 \frac{D}{Dt^2}\mathbf{U}_d{}^2 - \mathrm{Div}\mathbf{P} = \mathbf{0} \tag{67}$$

The artery wall is assumed to act as a hyperelastic material for which $\mathbf{P}$ based on Eq. (42) is as follows:

$$\mathbf{P} = \frac{\partial \Psi}{\partial \mathbf{F}} \tag{68}$$

where Ψ is the strain energy density function defined by the constitutive artery wall model.

2.2.3.2 Boundary conditions

The boundary conditions for the artery wall in the general form are as follows:

$$\mathbf{u} = \mathbf{u}_{\mathrm{D}},\ \mathbf{PN} = \mathbf{G} \tag{69}$$

where $\mathbf{u}_{\mathrm{D}}$ is the displacement prescribed at Dirichlet boundary, $\mathbf{N}$ is the unit normal vector in the material configuration pointing outward from the artery wall, $\mathbf{G}$ is the first Piola-Kirchoff stress tensor prescribed at the Neumann boundary.

2.2.3.3 Constitutive model

The non-trivial vascular wall structure requires a constitutive model that can reproduce mechanical behavior under various internal and external pressures during FSI simulations (Bianchi et al., 2017, Elkenani et al., 2017, Stupak et al., 2017). When considering FSI problems, oversimplified constitutive models will impede the results of structural and fluid flow domains. Some recently proposed problems require a very careful consideration of the constitutive artery wall model, as small disturbances in the blood flow velocity field caused by small displacements of the artery wall needs to be reliably determined (Misiulis et al., 2017). Therefore, we adopt a constitutive model proposed by (Holzapfel et al., 2000) and extended by (Holzapfel et al., 2005, Gasser et al., 2006), which to a great extent can reproduce a static arterial wall mechanical behavior. The SEF is given in a decoupled form consisting of two parts: a strictly convex function $\Psi_{\mathrm{vol}}(J)$, which is responsible for the volumetric (hydrostatic) elastic response, and the convex function in reduced form $\overline{\Psi}(\bar{I}_1, \bar{I}_4, \bar{I}_6)$, which is responsible for the volume preserving isochoric (deviatoric) elastic response, and the SEF then is given as follows:

$$\Psi = \Psi_{\mathrm{vol}}(J) + \overline{\Psi}(\bar{I}_1, \bar{I}_4, \bar{I}_6) \tag{70}$$

Artery wall is considered as incompressible material (Carew et al., 1968), and so the product of principal stretches: λ_r, λ_θ and λ_z in radial, circumferential and longitudinal directions, respectively is $\lambda_r\lambda_\theta\lambda_z = 1$. In order to enforce incompressibility constrain we introduce the Ψ_{vol} to be as follows (Kiousis et al., 2009):

$$\Psi_{\mathrm{vol}}(J) = \frac{\kappa}{2}(J-1)^2 \tag{71}$$

where κ is the bulk modulus, and when $\kappa \to \infty$, then $J \to 1$ and the exact incompressibilty is attained. However, finite element method (FEM) requires that incompressible materials should be set to nearly incompressible in order to avoid locking problem (Babuska et al., 1992) as the volumetric stresses usually have no impact on incompressible materials, and the shape functions are unable to evaluate the volumetric stress based on a strain or deformation gradient (COMSOL Multiphysics, 2015). The volumetric stress $\boldsymbol{\sigma}_m$ is calculated as follows:

$$\boldsymbol{\sigma}_m = -\frac{\partial \Psi_{\mathrm{vol}}(J)}{\partial J}\mathbf{I} \tag{72}$$

Given, that Eq. (71) is used for the $\Psi_{\text{vol}}(J)$, the volumetric stress $\boldsymbol{\sigma}_m$ then becomes linearly related to the volume change as follows:

$$\boldsymbol{\sigma}_m = -\kappa(J-1)\mathbf{I} \tag{73}$$

The reduced form of the isochoric response, that describes the features of arterial wall mechanical behavior, is governed by isotropic and anisotropic parts. The matrix component is considered isotropic and is governed by neo-Hookean constitutive model. The anisotropic part is governed by constitutive equation introduced in (Holzapfel et al., 2005). The isochoric part of SEF $\bar{\Psi}(\bar{I}_1, \bar{I}_4, \bar{I}_6)$, in Eq. (70) then is given as follows:

$$\bar{\Psi}(\bar{I}_1, \bar{I}_4, \bar{I}_6) = \bar{\Psi}_{\text{iso}}(\bar{I}_1) + \bar{\Psi}_{\text{aniso}}(\bar{I}_1, \bar{I}_4, \bar{I}_6) \tag{74}$$

where isotropic part is as follows:

$$\bar{\Psi}_{\text{iso}}(\bar{I}_1) = \frac{\mu}{2}(\bar{I}_1 - 3) \tag{75}$$

where $\mu > 0$ is a stress-like material parameter. The anisotropic part is as follows:

$$\begin{aligned}\bar{\Psi}_{\text{aniso}}(\bar{I}_1, \bar{I}_4, \bar{I}_6) = \sum_{i=4,6} \frac{k_1}{2k_2}(\exp\Big(k_2\big((1-\varsigma)(\bar{I}_1-3)^2 \\ + \varsigma(\bar{I}_i - 1)^2\big)\Big) - 1)\end{aligned} \tag{76}$$

where $k_1 > 0$ is a stress-like material parameter, $\varsigma \in [0,1]$ and $k_2 > 0$ are dimensionless parameters. ς can be interpreted as a dispersion about the mean fiber direction. Fibers only contribute in tension and therefore only when $\bar{I}_i > 1$.

Invariants $\bar{I}_1$, $\bar{I}_4$, $\bar{I}_6$ are as follows (Holzapfel et al., 2000):

$$\bar{I}_1 = \text{tr}\bar{\mathbf{C}}, \qquad \bar{I}_4 = \mathbf{M}_{f_1} \cdot \bar{\mathbf{C}}\mathbf{M}_{f_1}, \qquad \bar{I}_6 = \mathbf{M}_{f_2} \cdot \bar{\mathbf{C}}\mathbf{M}_{f_2} \tag{77}$$

where $\bar{\mathbf{C}} = \bar{\mathbf{F}}^{\text{T}}\bar{\mathbf{F}}$ is the isochoric right Cauchy-Green deformation tensor, $\bar{\mathbf{F}} = (J^{-1/3}\mathbf{I})\mathbf{F}$ is the isochoric part of deformation gradient, $\mathbf{M}_{f_i}$ $(i = [1,2])$ are tensors characterizing two families of collagen fibers by the tensor product of two mean fiber direction vectors in the material configuration (Holzapfel et al., 2000):

$$\mathbf{M}_{f_i} = \mathbf{m}_{0i} \otimes \mathbf{m}_{0i} \tag{78}$$

where based on (Holzapfel et al., 2005) it is assumed that collagen fibers have no radial component and, therefore, $\mathbf{m}_{0i}$ in the local cylindrical coordinate system is defined as follows:

$$\mathbf{m}_{01} = \begin{bmatrix} 0 \\ \cos(\beta) \\ \sin(\beta) \end{bmatrix} \tag{79}$$

$$\mathbf{m}_{02} = \begin{bmatrix} 0 \\ \cos(\beta) \\ -\sin(\beta) \end{bmatrix}$$

where β is the angle between the local longitudinal and the local circumferential directions.

In order to define $\mathbf{m}_{0i}$, that represent the mean fiber directions in the material configuration, the local cylindrical coordinate (global curvilinear coordinate) system must be introduced, which is dependent on the geometrical shape of the structure and is defined by vectors $\{\mathbf{r}_\Omega, \boldsymbol{\theta}_\Omega, \mathbf{z}_\Omega\}$ (Fig. 11). Ideally, planes P_1 and P_2 should be perpendicular as vectors $\{\mathbf{r}_\Omega, \boldsymbol{\theta}_\Omega, \mathbf{z}_\Omega\}$.

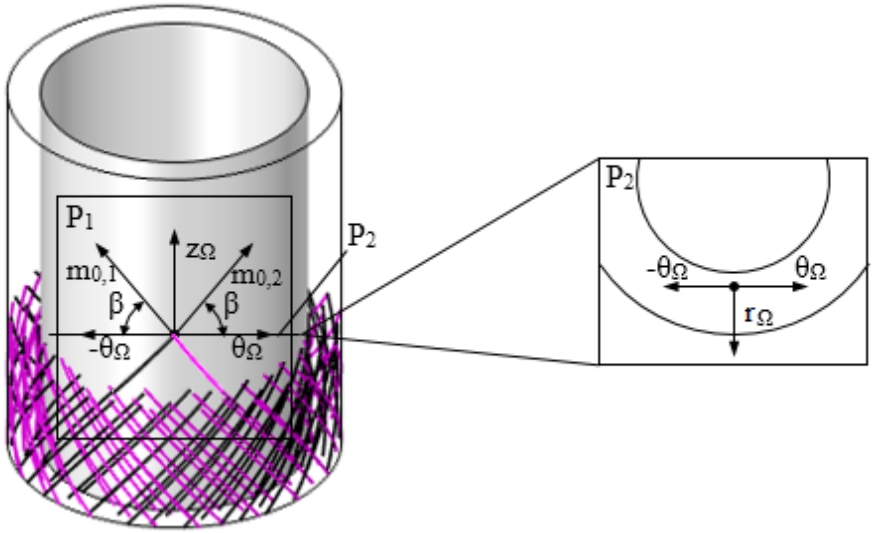

Fig. 11. The fiber structure with the unit vectors of curvilinear coordinate system on planes P_1 and P_2. Figure adapted from Fig. 1 in (Misiulis et al., 2019)

2.2.3.4 Methods of the mean fiber direction definition

There are several methods available for the mean fiber direction definition (Karajan et al., 2005, Kiousis et al., 2009, Alastrué et al., 2010, Bayer et al., 2012, Roy et al., 2014). In order to define the fiber structure in the artery wall, we developed a new method (*Method I*), which is based on the Laplace-Dirichlet method (Bayer, Jason et al., 2005). For the comparison of the resulting fiber structure, we selected the fiber definition method presented in (Alastrué et al., 2010) (*Method II*), which is currently the state-of-the-art fiber definition method.

Method I:

In order to define the mean fiber directions in the volume of the artery wall, we propose to solve the simplified partial differential equation (PDE) governing the physical process (such as fluid flow, scalar diffusion, etc.) with the corresponding boundary conditions. The gradient of the obtained scalar field provides the local basis upon which the mean fiber directions can be defined by Eq. (79).

In our case, the solution of the stationary modified scalar diffusion equation with the prescribed Dirichlet and Neumann boundary conditions provides the optimal results when compared with other PDE's (fluid flow, etc.) and, in addition, it can be trivially implemented into the FEM software, therefore, we elaborate here more on the implementation of this method in the FEM.

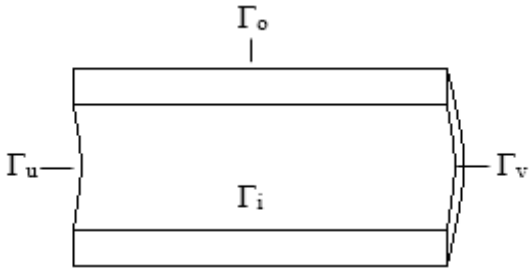

Fig. 12. Idealized cylindrical shape (only a half shown) with defined surface boundaries. Figure adapted from Fig. 2 in (Misiulis et al., 2019)

First, let us use the idealized cylindrical shape of an artery, as shown in Fig. 12, and define the surface of the inner wall, as Γ_i, the outer wall as Γ_o, one end wall as Γ_u, and the other end wall as Γ_v.

The curvilinear coordinates are obtained by solving the stationary modified scalar diffusion Eq. (80) with the corresponding boundary conditions, which is also known as the Laplace-Dirichlet method:

$$\nabla \cdot (\nabla U) = 0 \tag{80}$$

$$U = U_0, -\mathbf{n} \cdot \nabla U = 0 \tag{81}$$

were U is an arbitrary scalar field, U_0 is the value prescribed on the Dirichlet boundary, $\mathbf{n}$ is the unit vector of the surface normal. In FEM, weak formulation of the problem is needed, which is obtained by multiplying both sides of Eq. (82) by an arbitrary weighting (also called test) function v, and integrating over the domain Ω. By applying the divergence theorem, the weighted residual weak form then becomes as follows:

$$\int_{\Omega} \nabla U \cdot \nabla v d\Omega - \int_{\Gamma} \nabla U \cdot \mathbf{n} v d\Gamma = 0 \tag{82}$$

were Γ denotes the arbitrary boundary.

The longitudinal vector field ∇U_z is obtained by solving Eq. (80) with the Neumann boundary condition prescribed on the inner Γ_i and outer Γ_o artery wall surfaces, together with the Dirichlet boundary condition prescribed on both artery end surfaces, provided that $U_{\Gamma_u} \neq U_{\Gamma_v}$. The radial vector field ∇U_r is obtained similarly, only the Neumann and Dirichlet boundary conditions must be interchanged. Additionally, the normalization of the obtained vector fields is performed as follows:

$$\mathbf{r}_\Omega = \frac{-\nabla U_\mathrm{r}}{|-\nabla U_\mathrm{r}|},\ \mathbf{z}_\Omega = \frac{-\nabla U_\mathrm{z}}{|-\nabla U_\mathrm{z}|} \tag{83}$$

Finally, the circumferential vector field $\boldsymbol{\theta}_\Omega$ is defined as a cross product of the unitary radial and longitudinal vector fields, $\mathbf{r}_\Omega$ and $\mathbf{z}_\Omega$, consequently:

$$\boldsymbol{\theta}_\Omega = \mathbf{r}_\Omega \times \mathbf{z}_\Omega \tag{84}$$

Let us note that if the shape of the artery is a curved cylinder with varying wall thickness, the obtained radial vector field $\mathbf{r}_\Omega$ may not be perpendicular to the obtained longitudinal vector field $\mathbf{z}_\Omega$, which may produce errors in the mean fiber directions. Also let us note that similar idea based on the solution of the Laplace equation for potential energy was implemented to define fiber directions in the heart muscle (Bayer et al., 2012).

Method II (Alastrué et al., 2010):

The static linear elastic analysis with allowed radial inflation and a prescribed small pressure on the internal surface of the artery wall is performed to obtain the principal stress directions. The obtained principal stress directions allow the definition of the local cylindrical coordinate system and sequentially the definition of the fiber structure. When performing the static linear elastic analysis, the rigid body motion is prevented by introducing a spring foundation boundary condition on the internal part of an artery and setting the spring constant to a value, which does not influence the stress levels. Let us note that *method II* provides fiber directions, which are collinear, however the direction can be opposite at random (Fig. 13 a) and, after enforced data interpolation by the FEM software, leads to the wrong results of the structural analysis, and therefore, additional procedure is required to correctly align fiber directions. Our *method I* has served for this purpose. We assumed that both fiber definition methods provide similar mean fiber directions. When checking whether the angle between the Cartesian components is greater than 90 degrees, and in this case, changing the direction with respect to the direction obtained by *method I*, we obtained the expected transversely isotropic configuration shown in Fig. 13 b). We must note that the proposed method to align fiber directions is not general and may result in local deviations for certain geometric configurations.

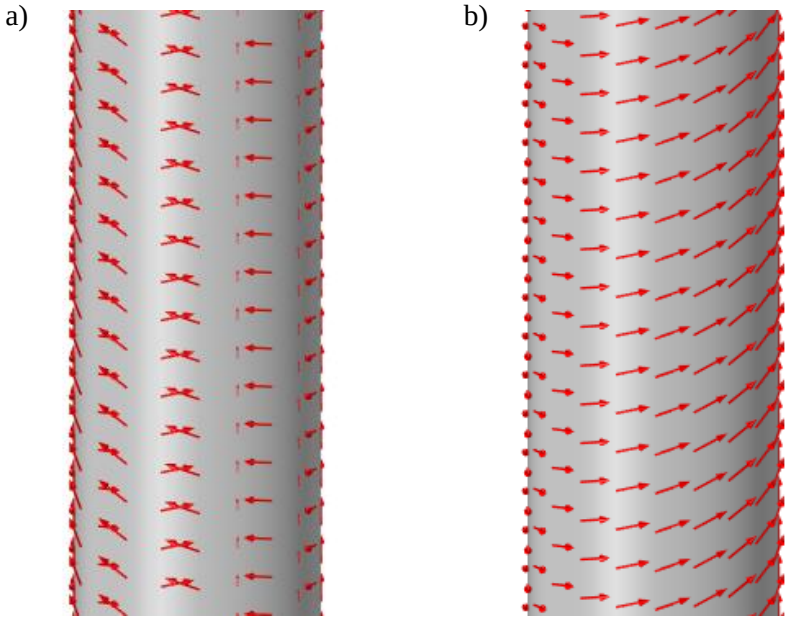

Fig. 13. Fiber directions shown on the mesh nodes of the internal surface of the straight portion of ICA obtained with method presented in (Alastrué et al., 2010) and interpolated in the COMSOL Multiphysics® software. a) initial result, b) aligned after additional procedure. Figure adapted from Fig. 3 in (Misiulis et al., 2019)

2.2.3.5 Governing equations for the blood flow

Blood flow is governed by the Navier-Stokes equations, which is a composition of the continuity and linear momentum conservation equations. The ALE formulation is used for the blood domain and therefore the Navier-Stokes equations in ALE formulation for the blood flow based on Eq. (44) and Eq. (45) with omitted volumetric forces are as follows:

- Continuity (mass conservation) for the incompressible blood:

$$\mathrm{div}\mathbf{v}_f = 0 \tag{85}$$

- Momentum (conservation of linear momentum):

$$\rho_f \left(\frac{\partial \mathbf{v}_f}{\partial t} + (\mathbf{c} \cdot \nabla)\mathbf{v}_f \right) - \mathrm{div}\boldsymbol{\sigma}_f = \mathbf{0} \tag{86}$$

2.2.3.6 Boundary conditions

The boundary conditions for the blood flow in the general form are as follows:

$$\mathbf{v}_f = \mathbf{v}_f^{\mathrm{D}}, \boldsymbol{\sigma}\mathbf{n} = \mathbf{g}_f \tag{87}$$

where $\mathbf{v}_f^{\mathrm{D}}$ is the velocity prescribed at Dirichlet boundary, $\mathbf{n}$ is the unit normal vector in the spatial configuration pointing outward from the blood domain, $\mathbf{g}_f$ is the Cauchy stress tensor prescribed at the Neumann boundary.

2.2.3.7 Constitutive model

The blood is treated as the incompressible Newtonian fluid for which the constitutive equation is as follows:

$$\boldsymbol{\sigma}_f = -p_f \mathbf{I} + \mu_f (\nabla \mathbf{v}_f + \nabla \mathbf{v}_f^{\mathrm{T}}) \tag{88}$$

were p_f is the arterial blood pressure, μ_f is the effective blood dynamic viscosity, which for Newtonian fluid is constant.

2.3 The modeling of the measurement

We define the measurement distance as the distance between two locations one of which is located in the part of the ophthalmic artery that is affected by the intracranial pressure, and the other is located in the part of the ophthalmic artery that is affected by the extracranial pressure. The properties of the measurement model:

• During the simulated measurement, information is obtained from the plane (without volume), one point of which coincides with the point on the center line of the artery, and the normal is directed according to the gradient of the center line.

• The step of measurement data collection depends on the time step of the data collected during the calculation.

3 RESULTS

We proposed and implemented a fiber structure definition method (*Method I*) presented in (2.2.3.4), which is based on the solution of the simplified equations describing the physical processes (such as hydrodynamics flow, scalar diffusion, etc.) in the volume of the artery wall. Obtained mean preferred fiber directions in the artery wall allowed us to implement the state of the art extended HGO constitutive artery wall model (chapter 2.2.3.3) and simulate the passive arterial wall behavior. In addition, the prestress method (GPA) was implemented (chapter 2.2.2), which allowed us to start the simulation with considered *in vivo* stresses. All the before mentioned implementations were incorporated into the COMSOL Multiphysics® software.

Results of model verification and validation are presented in chapter 3.1. In chapters 3.1.1 and 3.1.2 the simplified geometry is used for the model verification, while in chapter 3.1.3 the patient-specific geometry is used for the model validation.

Results of the simulation of the pulsatile blood flow in the compliant OA and discussion about the clinical relevance of the ICP measurement accuracy are presented in chapter 3.2.

3.1 Model verification and validation

3.1.1 Prestress method on a simple geometry

To verify the correctness of the GPA implementation, a test case scenario based on (Weisbecker et al., 2014) was performed. The hyperelastic incompressible cube (with dimensions $a \times a \times a$, were a = 1 mm) was made of one mixed finite element discretized with the linear Lagrange shape function. The cube was loaded with the force $\boldsymbol{\mathcal{F}} =$ 4 N, which was applied on the top surface Γ_t, as shown in Fig. 14 a). The bottom surface Γ_b was prescribed to be immovable in the normal direction and to prevent any rigid motion the spring foundation boundary conditions were prescribed on the sides with the spring constant $k = 1\ \mathrm{N/m^3}$. The obtained spatial configuration was of the following dimensions: $b \times b \times c$, with $b = 0.496$ mm and $c = 4.061$ mm. The obtained spatial configuration was used as a new material configuration, shown in Fig. 14 b). All boundary conditions were prescribed as in the previous case and the GPA was performed by increasing the force $\boldsymbol{\mathcal{F}}(n) = \boldsymbol{\mathcal{F}}/n$, were $n = 10$ is the number of time steps. At the last time step the force $\boldsymbol{\mathcal{F}}(n)$ was kept constant, while additional GPA iterations were performed, each reducing the overall displacement and error in a damped oscillating manner and converging towards the analytical solution, as well as to the solution provided in (Weisbecker et al., 2014). The Cauchy stress in the direction of loading was $\sigma_{zz} = 16.24$ MPa, and the corresponding prestrain was $F_{zz} = 4.061$, while in the perpendicular non-loaded directions the prestrain was $F_{xx} = F_{yy} = 0.496$.

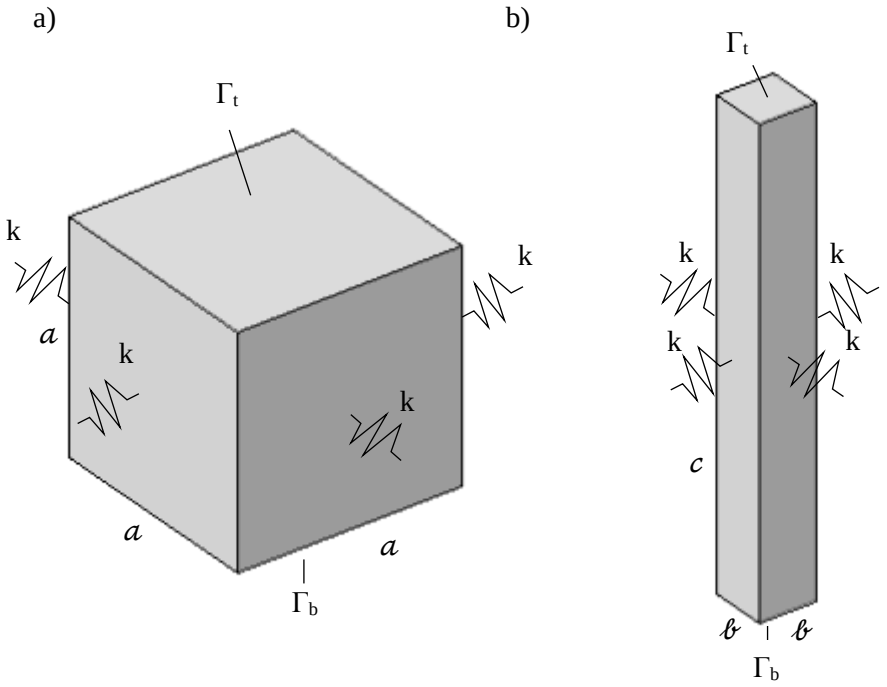

Fig. 14. The prestress scenario: a) unloaded unit cube and b) spatial configuration obtained after applied 4 N load on the top boundary, denoted as Γ_t. In the next step, the same spatial configuration shown in b) was initialized as material configuration without prestrain and the GPA was performed, which resulted in a correct reconstruction of the prestrain gradient. Figure adapted from Fig. 4 in (Misiulis et al., 2019)

3.1.2 Verification of the extended HGO material model implementation

To verify the correct implementation of the extended HGO material model in our numerical model we chose to reproduce the experimental results of mechanical testing of small ICA portions presented in (Sommer et al., 2012). The dimensions of our modeled ICA portion was based on the mean values given by the same authors in (Sommer et al., 2010). The outer radius in the unloaded configuration was $R_o = 2.67$ mm, wall thickness was $h_{\text{wall}} = 0.86$ mm, and the length was $L = 26$ mm. The artery wall was meshed with 2400 hexahedral mixed finite elements discretized with the quadratic Lagrange shape function and with $3 \times 20 \times 40$ elements in radial, circumferential and longitudinal directions, respectively (shown in Fig. 15 b). For the extended HGO material model the mean fiber directions were defined in the material configuration by methods presented in the Section 2.2.3.4.

We validated the correct implementation of fiber definition methods by comparing the obtained fiber structures with the analytical solution Eq. (79). It was found that the maximum difference of fiber directions between any of the fiber definition methods (*method I* and *method II*) and the analytical method in the whole

volume of a straight portion of ICA wall did not exceed $\Delta\beta < 0.6$ degrees and the relative (percentage) error did not exceed $\Delta\beta_p < 2.75$ %. The percentage error was calculated as follows: $\Delta\beta_p = |\beta_i - \beta_a|/\beta_a \cdot 100$ %, where β_i corresponds to the fiber direction obtained with the i-th method, where $i = 1, 2$, β_a corresponds to the fiber direction obtained with the analytical method.

In the extended HGO constitutive material model Eq. (70), the material parameters were defined based on (Sommer et al., 2012) of the intact ICA wall of a donor VII (Table 1). It was assumed that two fiber families were mechanically equivalent and therefore $\bar{I}_4 = \bar{I}_6$. The artery ends were prescribed to be immovable, and the pressure load was applied on the internal boundary Γ_i, shown in Fig. 15 a). The classical forward analysis was performed with the pressure load ranging from 0 mmHg to the 210 mmHg in increments of 10 mmHg. Additionally, another analysis was performed that incorporated the GPA followed by the forward analysis. The GPA was used to pre-load the straight portion of ICA up to the diastolic 80 mmHg pressure, and after the prestrain was obtained, the forward analysis was commenced to load the artery for up to the 210 mmHg of internal pressure. The resulting stresses of classical forward and GPA together with the forward analysis are shown in Fig. 15 c) and Fig. 15 d), respectively.

Table 1. ICA material parameters for the test case scenario reproduced from (Sommer et al., 2012) of the intact ICA wall of donor VII.

μ (kPa)	k_1 (kPa)	k_2	β (°)	ϱ
12.4	93.4	96.9	21.8	0.7

The obtained outer circumferential stretch of a straight portion of ICA was compared with the numerical fit of the experimental data (Sommer et al., 2012). The circumferential stretch was calculated as $\lambda_\theta = r_o/R_o$, were r_o is the outer radius obtained after the applied load and R_o is the initial outer radius. In addition, we obtained the inner circumferential stretch, defined as $\lambda_\theta = r_i/R_i$, and the midpoint circumferential stretch, defined as $\lambda_\theta = r_m/R_m$ (R_o, R_i, R_m are shown in Fig. 15 a). The small deviations in fiber directions obtained with *method I* and *method II* produced negligible effect on the outer circumferential stretch of the artery and therefore only one case is shown in Figure 6. From the Fig. 16 it can be seen that the numerically obtained outer circumferential stretch is comparable with the numerically fitted experimental results reproduced from (Sommer et al., 2012). The percentage error of the circumferential stretch between the solutions did not exceed 0.35 % over the applied internal pressure range. Additionally, from Fig. 17 it can be seen that when GPA is applied, the forward analysis resumes with stiffened ICA, which shows that the prestrain was incorporated, as ICA became stiffer.

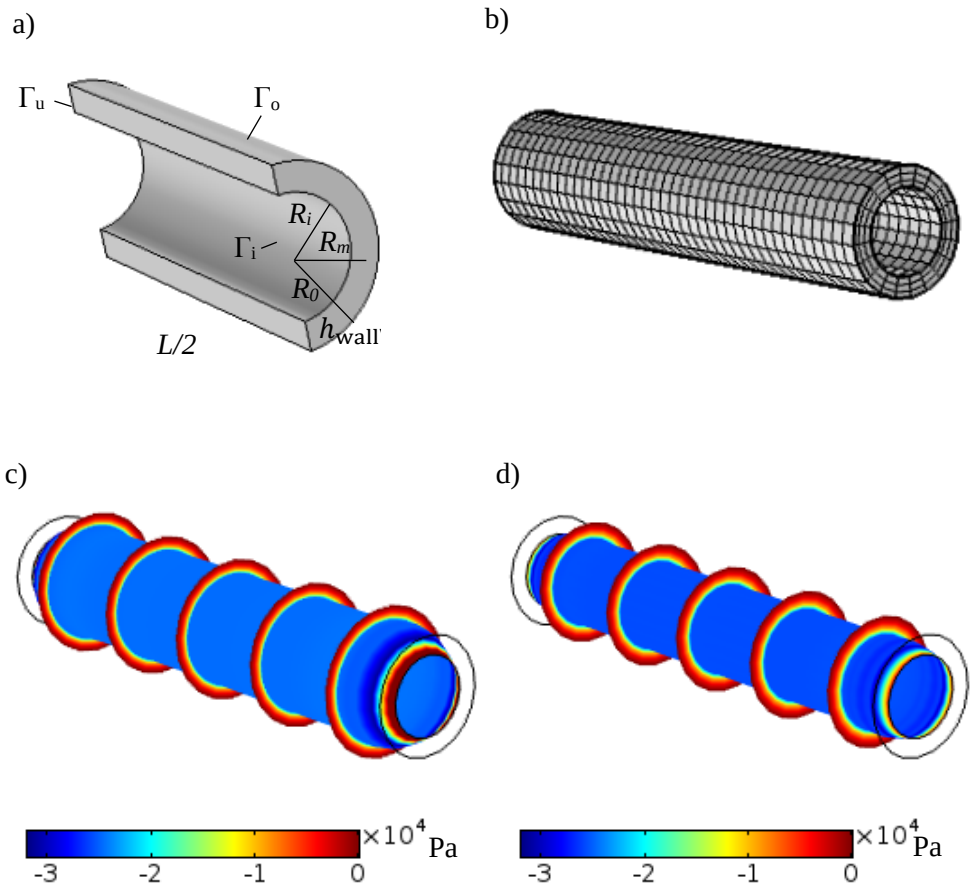

Fig. 15. In a) half of the artery is shown with defined boundaries and radiuses: R_0 – outer, R_m – middle, R_i – inner. In b) the mesh is shown. In c) the radial component σ_{rr} of the Cauchy stress is shown in case without the pre-load and in d) σ_{rr} is shown with the pre-load, both at 210 mmHg. Figure adapted from Fig. 5 in (Misiulis et al., 2019)

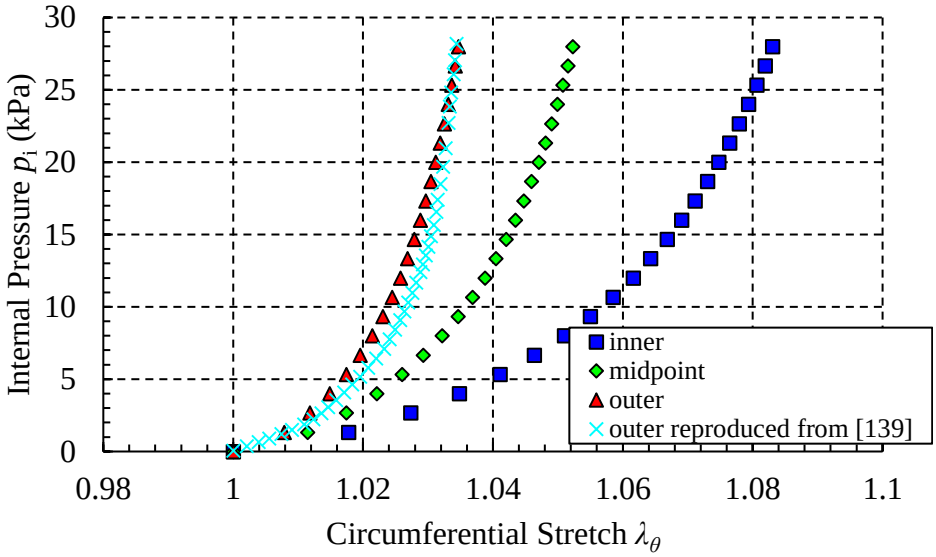

Fig. 16. Inner, midpoint and outer circumferential stretches obtained in numerical simulations with fiber directions defined with methods presented in chapter 2.2.3.4 and due to similar results represented in one figure. Circumferential stretch of the outer portion of the artery wall reproduced from (Sommer et al., 2012) is comparable with that obtained by us. Figure adapted from Fig. 6 in (Misiulis et al., 2019)

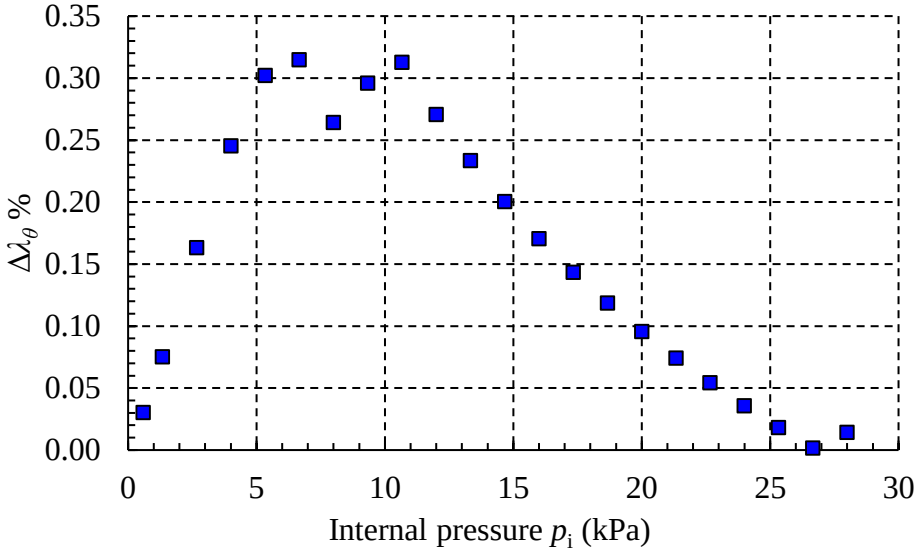

Fig. 17. The relative difference between our and (Sommer et al., 2012) results of the outer circumferential stretch of ICA in the internal pressure range from 0 kPa to 28 kPa

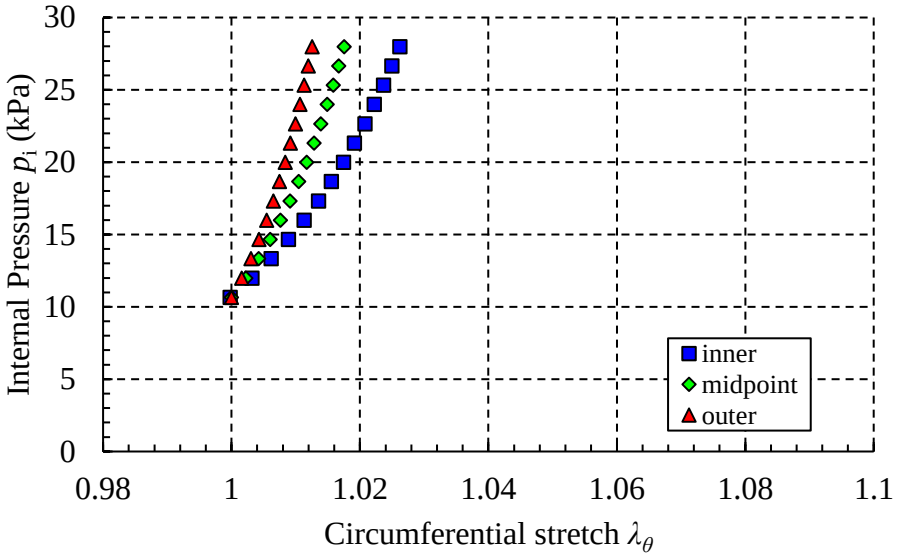

Fig. 18. Inner, midpoint and outer circumferential stretches obtained after pre-loading the straight portion of ICA up to the diastolic pressure of 80 mmHg and commencing the forward analysis for up to 210 mmHg. Figure reproduced from Fig. 7 in (Misiulis et al., 2019)

3.1.3 Verification of methods on the patient-specific artery

3.1.3.1 Geometry reconstruction

Reconstruction of the patient-specific ICA was made according to the methods provided in chapter 2.2.1. The reconstruction of ICA volume was performed from the MRI scan data (Magnetic field strength 1.5T, voxel size (0.37x0.37x0.5) mm^3), shown in Fig. 22 a). Obtained centerline of an artery is shown in Fig. 19.

The function of maximum inscribed sphere radius is obtained by performing a Fourier fit with the first 8 series terms (shown in Fig. 21):

$$R(\xi) = \mathfrak{a}_0 + \sum_{i=1}^{8} \mathfrak{a}_i \cos\left(i\xi w_f\right) + \mathfrak{b}_i \sin(i\xi w_f) \tag{89}$$

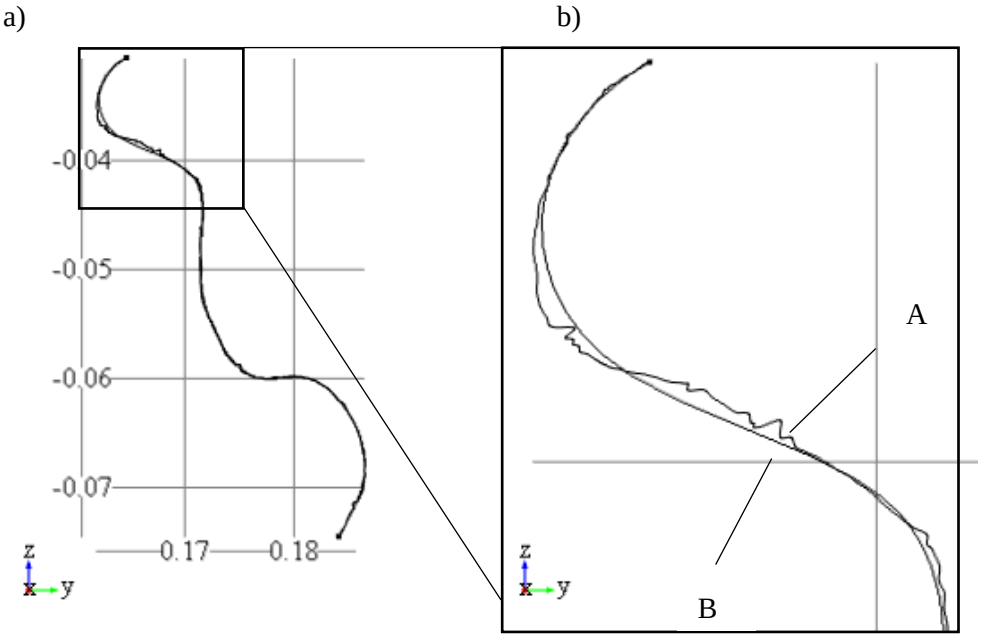

Fig. 19. Centerline A is composed of all the values obtained during the centerline computation in "VMTK 1.3", while centerline B represents a smoothed out centerline. The part where the biggest differences occur is zoomed and showed in b), while in a) the both full-length centerlines are showed. Figure adapted from Fig. 8 in (Misiulis et al., 2019)

The end parts of the ICA radius parametrization $R(\xi)$ was set to a constant value:

$$R(\xi) = \begin{cases} R_{out}, \xi < 0.22 \\ R_{in}, \xi > 0.88 \end{cases} \quad (90)$$

were $R_{out} = 2.09$ mm and $R_{in} = 2$ mm, otherwise due to boundary effects method of the maximum inscribed sphere radius provided erroneous results.

Artery wall thickness, h_{wall}, was defined to be proportional to the artery lumen radius $h_{\text{wall}} = 2 \cdot R(\xi)/5$ (Polak et al., 2010), where $0 \leq \xi \leq 1$ is the parametrization of the smoothed out centerline

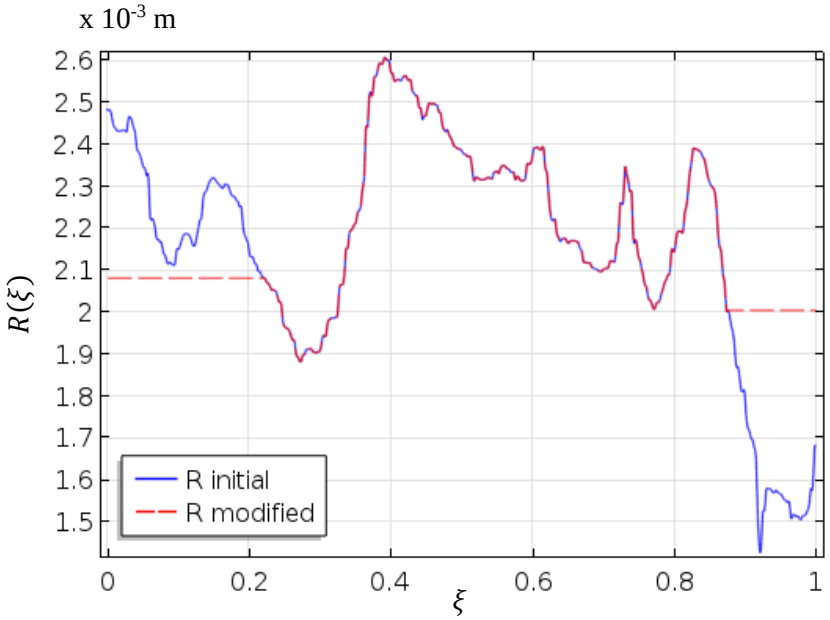

Fig. 20. Blue curve represents the initial radius (R initial) obtained by the "VMTK 1.3" software. Dashed red curve represents the modified radius (R modified), which is initial radius adopted to generate a 3D geometry. Figure adapted from Fig. 9 in (Misiulis et al., 2019)

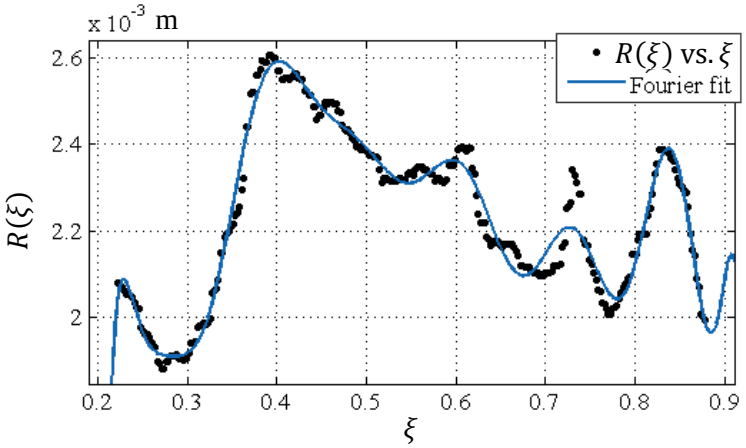

Fig. 21. Blue curve represents the Fourier fit, black dots represent the obtained maximum inscribed sphere radius at smoothed out centerline parameterized by ξ. Figure adapted from Fig. 10 in (Misiulis et al., 2019)

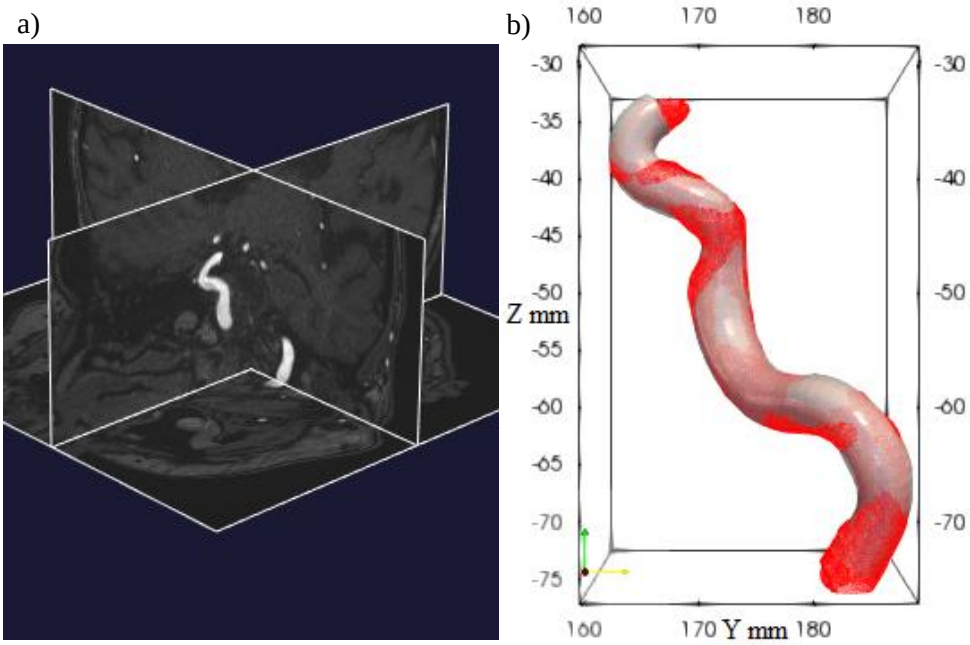

Fig. 22. a) a view of the MRI data in the "VMTK 1.3" software, b) patient-specific geometry (transparent white) created using the centerline obtained from the patient-specific geometry (wireframe red). Figure reproduced from Fig. 11 in (Misiulis et al., 2019)

The obtained patient-specific ICA geometry (shown in Fig. 22 b)) was meshed with a 11200 hexahedral mixed finite elements (Fig. 23) discretized with quadratic Lagrange shape function. $5 \times 28 \times 80$ elements were used in radial, circumferential and longitudinal directions to resolve stress gradients.

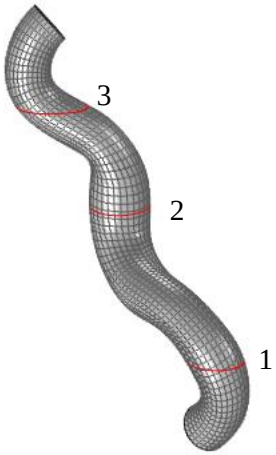

Fig. 23. Computational mesh and slices selected for the evaluation. Figure adapted from Fig. 12 in (Misiulis et al., 2019)

3.1.3.2 Comparison of fiber directions obtained with different methods for the patient-specific ICA

The mean fiber directions obtained by both fiber definition methods (chapter 2.2.3.4) are presented in Fig. 24 a) while their differences are shown in Fig. 24 b).

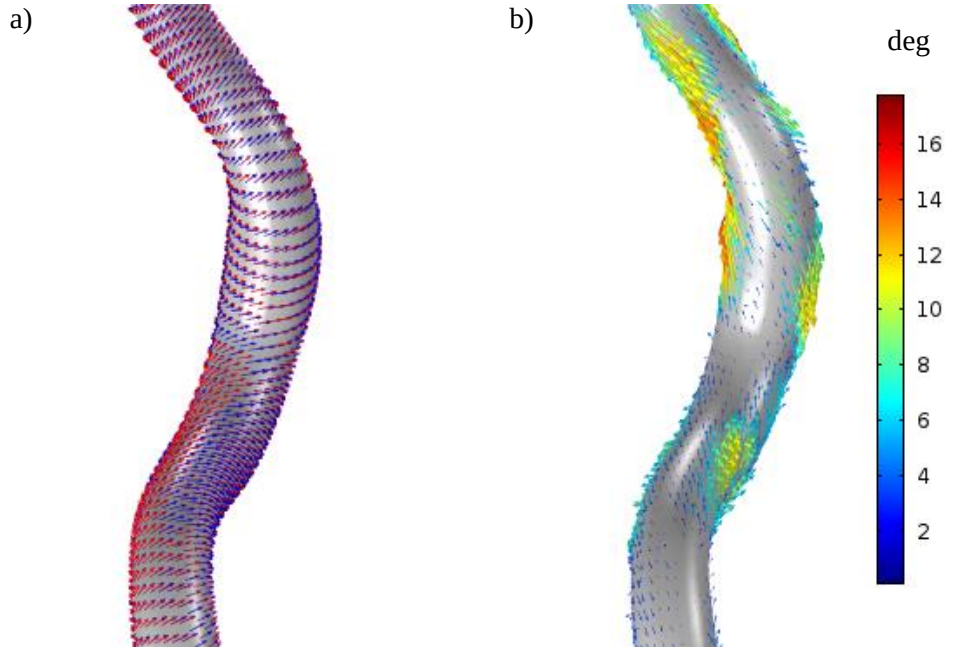

Fig. 24. Obtained mean fiber directions on the mesh nodes on the internal surface of ICA: a) blue and red arrows correspond to the mean fiber directions obtained with method I and method II, respectively, b) difference between the mean fiber directions. Figure adapted from Fig. 13 in (Misiulis et al., 2019)

From Fig. 24 a) it can be seen that mean fiber directions in a large portion of ICA was comparable. The average mean difference of fiber directions represented by the angle between vectors did not exceed 3.9 degrees in the whole volume of ICA wall, however, there were some regions were the difference in mean fiber directions were 0.01 degrees as well as regions were the difference reached 18 degrees (Fig. 24 b)). In terms of the percentage error the mean fiber directions defined by different methods did not exceed 17.73 % (at least 0.05 %, at most 81.82 %). The percentage error was calculated as follows: $\Delta\beta = |\beta_I - \beta_{II}|/\beta_p \cdot 100$ %, where β_I corresponds to the fiber direction obtained with *method I*, β_{II} corresponds to the fiber direction obtained with the *method II*, and β_p is the prescribed angle.

3.1.3.3 The mechanical behavior of the patient-specific ICA

The static mechanical analysis of the patient-specific ICA, whose mechanical behavior was defined by the extended HGO constitutive material model Eq. (70), was

performed with the material parameters based on the mean ICA material values provided in (Sommer et al., 2012) (shown in Table 2).

Table 2. Patient-specific ICA material parameters reproduced from (Sommer et al., 2012) (the mean of the intact ICA wall).

μ (kPa)	k_1 (kPa)	k_2	β (°)	ϱ
29.7	27.8	64.2	22	0.8

ICA ends were prescribed to be immovable while the load was applied on the internal lumen surface. Also, the spring foundation was prescribed on the internal lumen surface with the spring constant $k = 1 \cdot 10^6$, which was determined to have minimal effect on stresses and was used to prevent any rigid motion. It was assumed that two fiber families were mechanically equivalent and therefore $\bar{I}_4 = \bar{I}_6$.

The GPA was used to pre-load the ICA for up to the diastolic pressure of 80 mmHg and forward analysis was carried out from 80 mmHg to 180 mmHg in increments of 10 mmHg. The circumferential component of Cauchy stress obtained at the systolic pressure of 120 mmHg is shown in Fig. 25 b). The maximum percentage difference of the maximum stress values at slice locations (1, 2, 3) was less than 10 %, and the percentage error of the mean stress in the whole volume of ICA wall did not exceed 0.1 %.

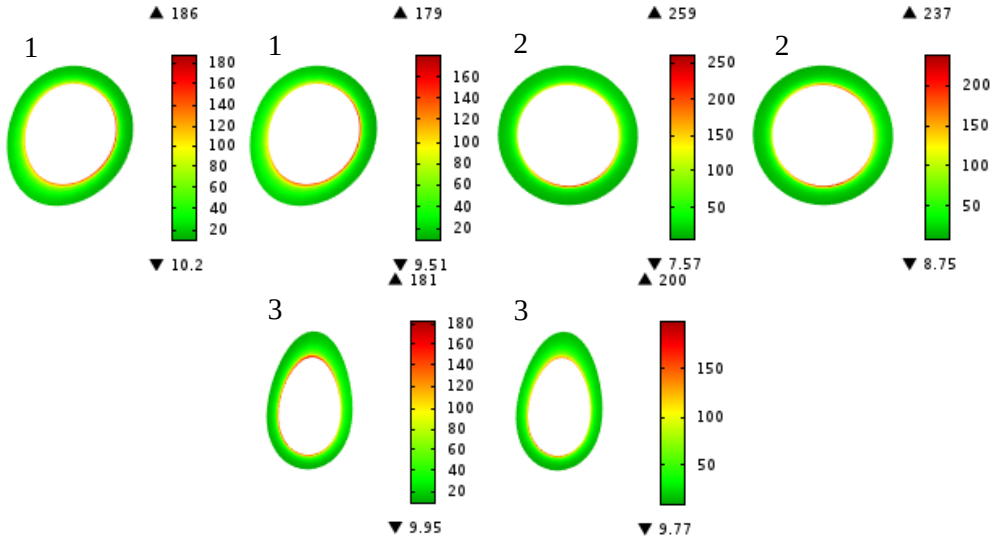

Fig. 25. The circumferential component $\sigma_{\theta\theta}$ of Cauchy stress in [kPa] at 120 mmHg internal pressure. Numbers corresponds to slices presented in Fig. 23. Figure adapted from Fig. 14 in (Misiulis et al., 2019)

3.2 Numerical investigation of the nICP measurement

We introduce the referential numerical model of a straight OA, which can be used as a general model that is easier to implement and test out, also it is a good reference based on which the effects of curvature can be evaluated by comparison

with a model in which a patient-specific artery is introduced. Both cases, case of a straight artery and case of a patient-specific artery have many conditions in common, therefore in the beginning we introduce common conditions and afterwards we introduce the results of the model of a straight OA and patient-specific OA.

3.2.1 Definition of parameters, boundary and initial conditions for straight and patient-specific OA models

The pulsatile blood flow in the compliant OA and their interaction was solved based on the governing equations presented in chapters 2.2.3.1 and 2.2.3.5.

The histologically motivated artery wall constitutive model (presented in chapter 2.2.3.3) that is stimulated by the mechanical effects of fibrous collagen structure inside the artery wall was implemented in our OA models. This is currently a state-of-the-art hyperelastic phenomenological model used in many scientific problems (Holzapfel et al., 2009, Nolan et al., 2014a, Carlsen et al., 2015, Leng et al., 2015, Montalvo Navarrete et al., 2017, Vu et al., 2018) especially regarding the artery wall (Gasser et al., 2006, Helfenstein et al., 2010, Zdunek et al., 2017, Leng et al., 2018, Wang et al., 2018) as it is able to accurately reproduce mechanical behavior and an exponential stiffening effect common to arteries.

It was assumed that two fiber families were mechanically equivalent and, therefore, $\bar{I}_4 = \bar{I}_6$ (Nolan et al., 2014b).

Blood was considered as incompressible, Newtonian fluid (presented in chapter 2.2.3.7) and at the inlet started as a fully developed laminar flow. The consideration of the Newtonian blood flow model is justified by the fact that OA is larger than 1 mm and therefore the shear rate was expected to be larger than 100 s^{-1} everywhere in the OA and at every time moment.

Arbitrary Lagrangian-Eulerian (ALE) formulation (presented in chapter 2.1.2) was used to describe the deformations of the fluid domain (Benselama et al., 2007). The artery wall was formulated in material description, while blood domain was formulated in ALE formulation and therefore in a deformable mesh description. ALE formulation allowed us to track the boundary interface between blood and artery wall, and therefore to solve the FSI problem.

A transient fluid-structure interaction (FSI) simulation of the blood flow in a compliant OA was performed. Boundaries Γ_1 (in IOA segment) and Γ_2 (in EOA segment) were affected by the pressure $ICP_{1,i}$ and Pe, respectively (shown in Fig. 27 and Fig. 34). The wall of the OA was considered as nearly incompressible (Carew et al., 1968), hyperelastic material composed of two layers (in case of straight OA) and composed of one layer (in case of patient-specific OA), of which mechanical characteristics were defined by material parameters.

Table 3. Basic material parameters

Blood properties	**Notation**	**Value**	**Units**
Effective dynamic viscosity (Milnor, 1990)	μ_f	0.003675	$kg \cdot m^{-1} \cdot s^{-1}$
Density (Cutnell et al., 1997)	ρ_f	1060	$kg \cdot m^{-3}$
OA wall properties	**Notation**	**Value**	**Units**
Density (Kuhl et al., 2007)	ρ_s	1100	$kg \cdot m^{-3}$

Table 4. Basic simulation parameters

Simulation parameters	**Notation**	**Value**	**Units**
Duration of one heartbeat pulse period (Holdsworth et al., 1999)	T	1	s
Duration of initialization	t_{init}	1	s
Duration of Pe = const	t_c	2	s
Duration of Pe loop	t_P	3	s
Peak value of velocity profile max. of one time period	$u_{max_{peak}}$	56.48	cm/s
Surface averaged value of velocity profile max. of time period	$u_{max_{mean}}$	28.24	cm/s
Peak value of velocity profile min. of time period	$u_{min_{peak}}$	12.28	cm/s
Surface averaged value of velocity profile min. of time period	$u_{min_{mean}}$	6.14	cm/s
Max. pressure of time period (Langham, 2009)	P_{sys}	80	mmHg
Min. pressure of time period (Langham, 2009)	P_{dias}	40	mmHg
Magnitude of the increase in $ICP_{1,i}$	s_{ICP}	10	mmHg
Amplitude of ICP_i (function of i)	$A_{ICP} = s_{ICP}(i-1)$		mmHg
Amplitude of Pe	A_{Pe}	38	mmHg
Magnitude of the increase in Pe	s_{Pe}	2	mmHg

We assumed that the rate of change of ICP is negligible during one heartbeat pulse period, therefore the ICP was constant throughout the heartbeat pulse period. It was assumed that ICP is homogenously distributed on the surface it acts on.

ICP was prescribed as a Neumann boundary condition based on Eq. (69) and Eq. (91) as a function dependent on time $ICP_i(t)$ acting on the outside surface of IOA wall segment Γ_1 as follows:

$$ICP_i = A_{ICP}(i)\begin{cases}\dfrac{t}{t_{init}}, & t < t_{init}\\ 1, & t \geq t_{init}\end{cases} \tag{91}$$

For a healthy adult in the supine position, normal ICP is in the range between 7 mmHg and 15 mmHg (Steiner et al., 2006), for children between 3 mmHg and 7 mmHg, for term infants from 2 mmHg and 6 mmHg, and for pathological patients, ICP can exceed 25 mmHg (Dunn, 2002). Aforementioned ICP values motivated us to set ICP lower limit to 0 mmHg and upper limit to 30 mmHg and in case of a straight

OA the set of ICP amplitude values was, $A_{ICP}(i) = \{0, 10, 20, 30\}$ mmHg, for $i =$ 1,2,3,4, while in case of patient-specific OA only one value $A_{ICP}(i) = 10$ mmHg was used.

Pe was prescribed as a Neumann boundary condition based on the Eq. (69) and Eq. (92) as a function dependent on time $Pe(t)$ acting on the outside surface of EOA wall segment Γ_2 as follows:

$$Pe = \begin{cases} Pe_b, & t > t_{init} \\ 0, & t \leq t_{init} \end{cases} \tag{92}$$

where Pe_b was prescribed as follows:

$$Pe_b = s_{Pe} \begin{cases} \dfrac{t - \text{floor}\left(\dfrac{t}{t_P}\right) t_P}{T} + \text{floor}\left(\dfrac{t}{t_P}\right) - 1, & t - \text{floor}\left(\dfrac{t}{t_P}\right) t_P < T \\ \text{ceil}\left(\dfrac{t - t_P}{t_P}\right), & t - \text{floor}\left(\dfrac{t}{t_P}\right) t_P \geq T \end{cases} \tag{93}$$

Boundaries Γ_3, Γ_4 (shown in Fig. 27 and Fig. 34) were prescribed to be immovable based on the Dirichlet boundary condition Eq. (69) and the spring foundation was prescribed on interface boundary Γ_i with a spring constant defined so as to have no effect on the stress field and only to limit the rigid motion.

Laminar inflow boundary condition based on the Neumann boundary condition Eq. (69) was prescribed as a pressure function $P_{in}(t)$ acting on the surface of OA blood domain inlet. It was used to start the blood flow as fully developed at the inlet and was prescribed as follows:

$$P_{in} = \begin{cases} \dfrac{P_{dias} t}{t_{init}}, & t < t_{init} \\ P_v, & t \geq t_{init} \end{cases} \tag{94}$$

where P_v waveform was similar to v_{in} waveform provided in Fig. 26 with a difference in amplitude where P_{sys} was pressure value at the systole and P_{dias} was pressure at the diastole.

We considered a constant outlet pressure boundary condition at pre-calculated distance, which led to the periodic downstream vasculature resistance and therefore, it was not used to predict the behavior of downstream vasculature due to added external pressure, but was used to generate a typical velocity waveform Fig. 26.

Laminar outflow boundary condition based on the Neumann boundary condition Eq. (69) was prescribed as a constant pressure function $P_{out}(t)$ acting on the surface of OA blood domain outlet and it was used to define the pressure P_{out} at distance L_{exit} as follows:

$$P_{out} = \begin{cases} \dfrac{P_{dist} t}{t_{init}}, & t < t_{init} \\ P_{dist}, & t \geq t_{init} \end{cases} \tag{95}$$

A combination of variable inlet pressure P_{in} and constant outlet pressure $P_{dist} = 70.15$ mmHg Eq. (97) at the analytically calculated distance $L_{exit} = 25.63$ cm Eq. (96), based on the Hagen-Poiseuille equation generated a uniform waveform of blood pressure and the blood velocity according to Fig. 26.

$$L_{exit} = \frac{d_{init}^2 (P_{sys} - P_{dias})}{32\mu(u_{max_{mean}} - u_{min_{mean}})} \tag{96}$$

$$P_{dist} = P_{sys} - \frac{u_{max_{mean}}(P_{sys} - P_{dias})}{(u_{max_{mean}} - u_{min_{mean}})} \tag{97}$$

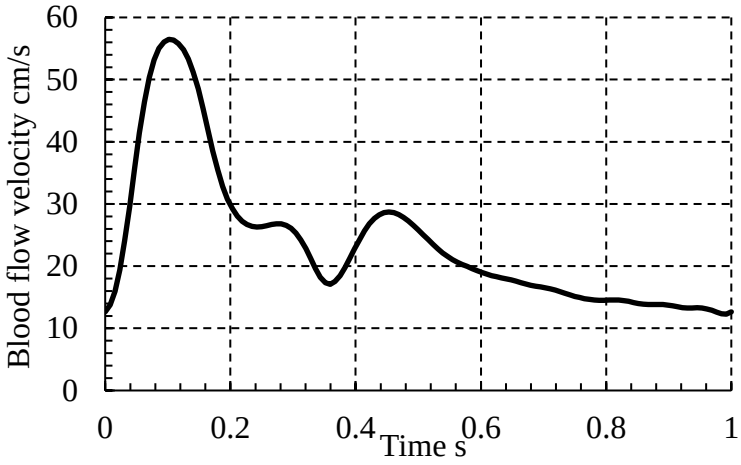

Fig. 26. Typical maximum blood flow velocity waveform in OA that was implemented in the numerical model. Figure adapted from Fig. 4 in (Misiulis et al., 2018)

3.2.2 Case of the straight OA

3.2.2.1 Model parameters

Parameters presented in Table 5, and Table 6 are used to define the basic OA wall morphological parameters, and locations of data extraction.

Table 5. OA geometry parameters

OA wall parameters	Notation	Value	Units
initial lumen diameter	d_{init}	1.3	mm
length of the OA (Hayreh, 2006)	L	25.8	mm
length of Γ_1 (IOA) (Hayreh, 2006)	L_{Γ_1}	4.1	mm
length of Γ_5 (OC) (Liu et al., 2000)	L_{Γ_5}	12	mm
length of Γ_2 (EOA) (Hayreh, 2006)	L_{Γ_2}	9.7	mm
wall thickness (Polak et al., 2010)	h_{wall}	0.18	mm

Table 6. Locations of cross-sections were data was extracted

Simulation parameters	Notation	Value	Units
distance from the OA starting location at which the data was collected at IOA segment	$L_{c,IOA}$	2.058	mm
distance from the OA starting location at which the data was collected at EOA segment	$L_{c,EOA}$	20.834	mm

3.2.2.2 Model setup

OA geometry was composed of a blood domain Ω_{blood} and two OA wall domains: Ω_{media} and $\Omega_{adventitia}$ shown in Fig. 27. Parameters defining the basic material properties of the blood, and of the OA wall are given in Table 3. As the data of additional parameters, required by constitutive material model for OA wall, are scarce in the scientific literature, ICA parameters were used instead (provided in Table 7).

Table 7. OA wall parameters used for fiber-reinforced double layer model based on ICA wall parameters according to (Sommer et al., 2012)

Arterial wall parameters	Adventitia	Media
Isotropic, μ, kPa	28.3	17.6
Anisotropic, k_1, kPa	112.1	21.3
Anisotropic, k_2	100.6	17.3
Fiber angle, β, deg	31.8	9.8
Dispersion, ϱ, 1	0.9	0.8

Structural information consisting of the wall thickness of OA, the internal vessel diameter, the length of the vessel and the lengths of IOA, OC, and EOA segments are provided in Table 5.

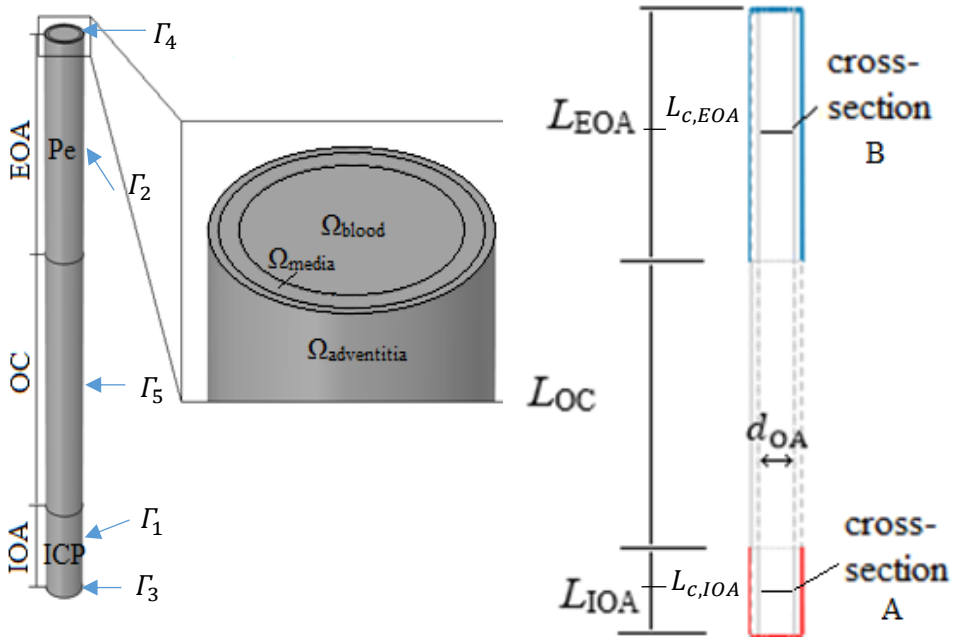

Fig. 27. The OA model geometry with depicted IOA, OC, EOA segments, blood and OA *media* and *adventitia* layer domains, boundaries of acting pressures *Pe* and *ICP* together with a cross-sectional scheme of OA and lines representing A and B cross-sections where the data was collected at the distances $L_{c,IOA}$ and $L_{c,EOA}$, respectively. Figure adapted from Fig. 3 in (Misiulis et al., 2018)

Based on (Misiulis et al., 2017), the geometry was discretized into 71644 finite elements, with 49734 elements for blood domain, 13506 elements for *tunica media* domain, and 8404 elements for *tunica adventitia* domain.

3.2.2.3 Analysis of simulation results

In total $n \cdot 60$ time periods were modeled, where $n = 4$ is the number of simulations and $i = \overline{1{:}n}$ is the study index/number. The first time period was used to initialize the simulation by gradually increasing the inlet pressure P_{in} from 0 mmHg to 40 mmHg, outlet pressure P_{out} from 0 mmHg to P_{dist} and ICP_i from 0 mmHg to $\{0, 10, 20, 30\}$ mmHg depending on the study number i. After initialization ICP was held constant, while Pe changed according to Eq. (92), $Pe = 0{:}2{:}38$ mmHg.

Starting from $t = 0\ s$, the data was collected at every time step $t_s = 0.004\ s$ for all $n \cdot 60$ hearbeat pulse periods. During simulation blood density and blood dynamic viscosity was constant, while the blood velocity and the lumen diameter was dynamic parameters. The maximum $Re_{max} = \rho_f |\mathbf{v}_f(t_{sys})| d(t_{sys})/\mu = 129$, where t_{sys} is the time of systole and minimum $Re_{min} = \rho_f |\mathbf{v}_f(t_{dias})| d(t_{dias})/\mu = 24.7$, where t_{dias} is the time of diastole Reynolds numbers were calculated from all data

points to justify the assumption of laminar blood flow. In addition, the Womersley number was calculated and found to be approximately equal to $\alpha \approx 0.86$.

From all the data available, only the specific data on the cross-sections A and B (Fig. 27) were selected ($i = \{A, B\}$), i.e. the cross-sectional area $S_i(t)$, over the cross-section averaged blood flow velocity $< v_i(t) >$ and the blood pressure $< p_i(t) >$. Characteristic parameters are periodic in time, therefore, we denote $t' = \mathrm{mod}(t, T)$, which allows us to compare the results on a single time scale, and to evaluate the influence of ICP and Pe. With t' introduced the functional dependence of characteristic parameters becomes as follows: $S_i(t', ICP, Pe)$, $< v_i(t', ICP, Pe) >$ and $< p_i(t', ICP, Pe) >$. Next, we omit the variables in brackets and use only S_i, $< v_i >$ and $< p_i >$. In general we denote the characteristic parameter as follows: $c_i = \{S_i, < v_i >, < p_i >\}$.

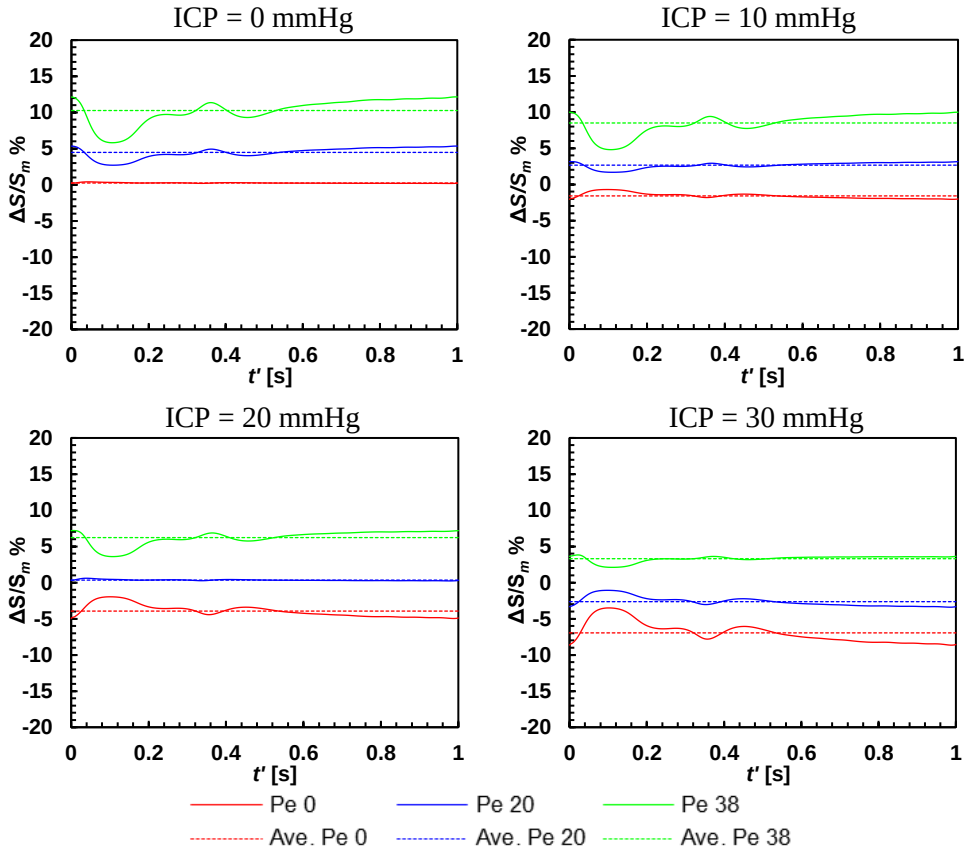

Fig. 28. Cross-sectional area difference between A and B cross-sections, denoted as ΔS, and over the heartbeat pulse period averaged ΔS, denoted as $\widehat{\Delta S}$, dependence on t', ICP and Pe

Differences of the blood flow parameters between the OA segments affected by ICP and Pe are important during the nICP measurement. The differences between A and B cross-sections of the S_i, $< v_i >$ and $< p_i >$ are as follows: $\Delta S = S_A - S_B$, $< \Delta v >=< v_A > - < v_B >$ and $< \Delta p >=< p_A > - < p_B >$. In general we denote the

difference of the characteristic parameter between A and B cross-sections as follows: $\Delta c = \{\Delta S, < \Delta v >, < \Delta p >\}$.

The differences in cross-sectional areas were divided by $S_m = \frac{\hat{S}_A - \hat{S}_j}{2}$, were $\hat{S}_A$ is the over the heartbeat pulse period averaged cross-sectional area at cross-section A, $\hat{S}_j$ is the over the heartbeat pulse period averaged cross-sectional area at cross-section j, were in this case $j = \{B\}$.

The differences in mean blood flow velocity were divided by $v_m = \frac{\hat{v}_A - \hat{v}_j}{2}$, were $\hat{v}_A$ is the over the heartbeat pulse period averaged mean blood flow velocity at cross-section A, $\hat{v}_j$ is the over the heartbeat pulse period averaged mean blood flow velocity at cross-section j, were in this case $j = \{B\}$.

Over one heartbeat pulse period averaged ΔS, $< \Delta v >$ and $< \Delta p >$ are denoted as $\widehat{\Delta S}$, $< \widehat{\Delta v} >$ ir $< \widehat{\Delta p} >$, respectively. In general the difference of the characteristic parameter between A and B cross-sections averaged over one heartbeat pulse period is denoted as follows: $\widehat{\Delta c} = \{\widehat{\Delta S}, < \widehat{\Delta v} >, < \widehat{\Delta p} >\}$.

We must note that the influence of Pe and ICP on the characteristic parameters not only depends on their difference but also on their respective values and therefore when we refer to the $Pe - ICP$ we also refer to the given Pe and ICP values.

ΔS and $\widehat{\Delta S}$ dependence on the t', ICP and Pe is shown in Fig. 28. From Fig. 28 it can be seen that when $Pe - ICP$ becomes close to a value that we denote as inv, then changing the $Pe - ICP$ in the same direction as before, results in the inversion of ΔS with respect to the time axis t'. This means that the change in dynamics of the standard deviation of S_A and S_B is due to the change in acting pressures, i.e. the change in $Pe - ICP$ value. These processes are due to the non-linear artery wall constitutive model.

The standard deviation of the ΔS (Fig. 29) (or characteristic parameter Δc) is calculated as follows:

$$\mathrm{SD}(\Delta c) = \sqrt{\frac{\sum_{i=1}^{n} (\Delta c_i - \widehat{\Delta c})^2}{n}} \tag{98}$$

From Fig. 29 it can be seen that the standard deviation of ΔS becomes the lowest when $Pe - ICP \to inv$, irrespectively of the specific values of Pe and ICP.

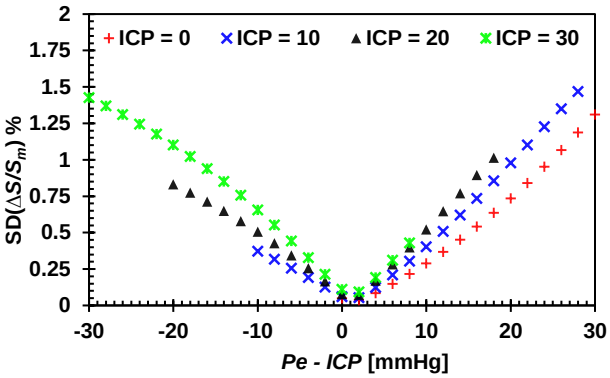

Fig. 29. The dependence of the standard deviation of the ΔS on Pe and ICP

A heartbeat pulse averaged difference $< \Delta p >$, denoted as $< \widehat{\Delta p} >$, dependence on the parameters ICP and Pe is depicted in Fig. 30. It can be seen that $< \widehat{\Delta p} >$ changes nonlinearly with respect to ICP and Pe. This nonlinear change is due to nonlinear change in ΔS. When $ICP = Pe = \{0, 10, 20, 30\}$ mmHg, then $< \widehat{\Delta p} > = \{1.112, 1.124, 1.141, 1.164\}$ mmHg. $< \Delta v >$ and $< \widehat{\Delta v} >$ dependence on t', ICP and Pe is shown in Fig. 31. From Fig. 31 it can be seen that unlike ΔS case, when $Pe - ICP \rightarrow inv$, then $< \Delta v >$ does not tend towards the $< \widehat{\Delta v} >$.

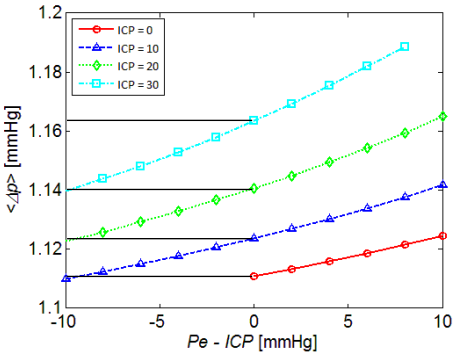

Fig. 30. Over a heartbeat pulse period averaged $< \Delta p >$, denoted as $< \widehat{\Delta p} >$, dependence on the ICP and Pe

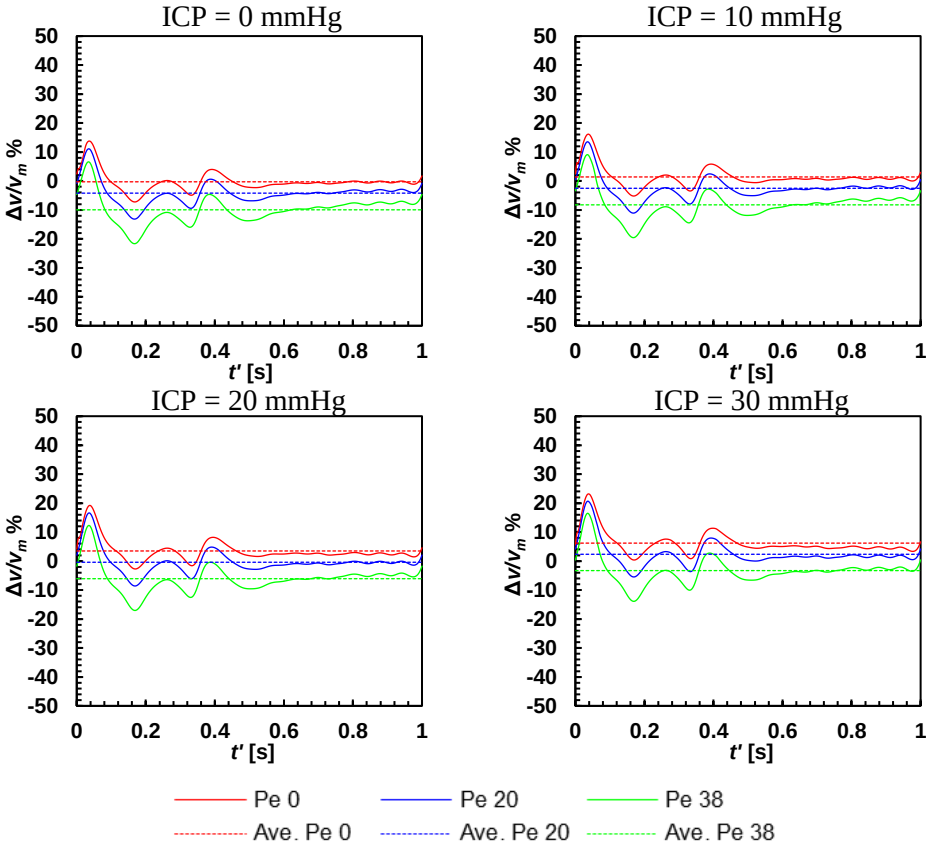

Fig. 31. Surface averaged blood flow velocity difference between A and B cross-sections, denoted as $< \Delta v >$, and over a heartbeat pulse period averaged $< \Delta v >$, denoted as $< \widehat{\Delta v} >$, dependence on t', ICP and Pe

As the Pe or ICP increases, the standard deviation of the $< \Delta v >$ determined by Eq. (98) also increases (Fig. 32).

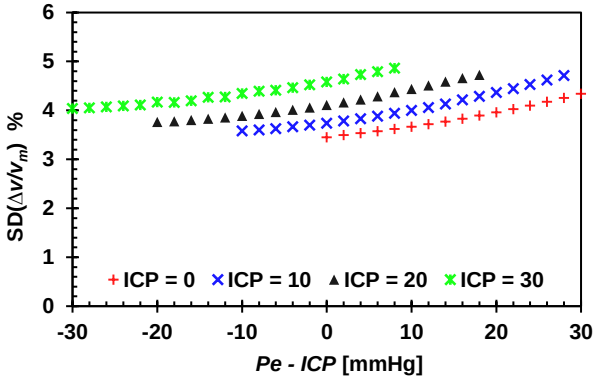

Fig. 32. The dependence of the standard deviation of the $< \Delta v >$ on *Pe* and *ICP*

$\widehat{\Delta S}$ and $< \widehat{\Delta v} >$ dependence on ICP and Pe is shown in Fig. 33 a) it can be seen that when $\widehat{\Delta S} = 0$, then $ICP = Pe \pm \varepsilon$, where ε is the deviation from the balance condition at $< \widehat{\Delta c} > = 0$. From Fig. 33 b) we can see that the same is true for the blood velocity, only the deviation based on $< \widehat{\Delta v} >$ differ from the deviation obtained based on $\widehat{\Delta S}$, therefore the deviation based on $\widehat{\Delta S}$ is denoted as ε_S and the deviation based on $< \widehat{\Delta v} >$ is denoted as ε_v. The ε_S and ε_v are determined by evaluating the intersection point of curves, denoted as (ICP = 0, ICP = 10, ICP = 20, ICP = 30) with their respective axis. In this way $\varepsilon_S = \{-1.48, -1.37, -1.17\}$ mmHg, and $\varepsilon_v = \{-1.84, -1.76, -1.625\}$ mmHg, when $ICP = \{10, 20, 30\}$ mmHg. The difference between ε_S and ε_v is due to artery compliance in the region between A and B cross-sections. As the artery expands it creates additional volume between A and B cross-sections, which is occupied by incoming blood flow, and as the artery contracts this volume is reduced. However, when integrated over one heartbeat pulse period it turns out that the blood flow rate difference between A and B cross-sections is non-zero, leading to the aforementioned difference in deviations. We denote deviation due to compliance as $\varepsilon_c = \{-0.36, -0.39, -0.455\}$ mmHg, when $ICP = \{10, 20, 30\}$ mmHg. The deviation due to compliance is dependent on the constitutive artery wall model, on the external material effect on the dynamics of the arterial blood pressure and on the initial lumen volume between A and B cross-sections.

In case of $\widehat{\Delta S} = 0$, the systematic deviation ε_S would be 0 only if the mechanical conditions in cross-sections A and B would be equivalent and there would be no difference in acting pressures (Misiulis et al., 2016). Artery mechanical non-equivalence means that it acts differently when subjected to the same loads. This is at least due to different internal stress distribution, which can be due to the difference in curvature, external tissue behavior (which can be imitated by appropriate boundary conditions), etc. In our case, based on (Misiulis et al., 2016) the mechanical non-equivalence is due to the non-equivalent internal stress distribution between IOA and EOA segments and therefore in A and B cross-sections. We will denote the deviation due to mechanical non-equivalence, as p_{add}. From Fig. 33 a) at $\widehat{\Delta S} = 0$ the $p_{add} = \{-0.356, -0.229, -0.006\}$ mmHg. In (Misiulis et al., 2017), only one value of ICP was considered of 10 mmHg and the bifurcation site of OA from internal carotid artery effect was incorporated and modeled, while in this study imaginary bifurcation site at boundary Γ_3 was prescribed to be immovable. In (Misiulis et al., 2017) it was obtained that $\varepsilon_S = -0.5$ mmHg, $p_{add} = 0.26$ mmHg, $\varepsilon_v = 1.1$ mmHg and $\varepsilon_c = 1.6$ mmHg. While in this study, with $ICP = 10$ mmHg these values were $\varepsilon_S = -1.48$ mmHg, $p_{add} = -0.356$ mmHg, $\varepsilon_v = -1.84$ mmHg, and $\varepsilon_c = -0.36$ mmHg. The difference in p_{add} between this investigation and (Misiulis et al., 2017) suggests, that internal stress distribution differences due to bifurcation site reduces the deviation by 34%, while immovable boundary increases it by {31.67 %, 20.07 %, 0.5 %} (with the reference to $< \widehat{\Delta p} >$ and $ICP = \{10, 20, 30\}$ mmHg). However, the effect on deviations in the model by (Misiulis et al., 2017) may change with the change in ICP as suggested by current investigation where p_{add} decreased with ICP value reducing effect on the deviations. Artery compliance between selected A and B cross-sections increased the deviation by 210% in the study of (Misiulis et al., 2017), while in this

study it increased the deviation by {32 %, 34 %, 39%} (with reference to $< \widehat{\Delta p} >$ and $ICP = \{10, 20, 30\}$ mmHg). The effect of compliance cannot be directly compared with the results of (Misiulis et al., 2017) as the initial volume between A and B cross-sections, constitutive artery wall model, arterial blood pressure dynamics and the external material effect was different.

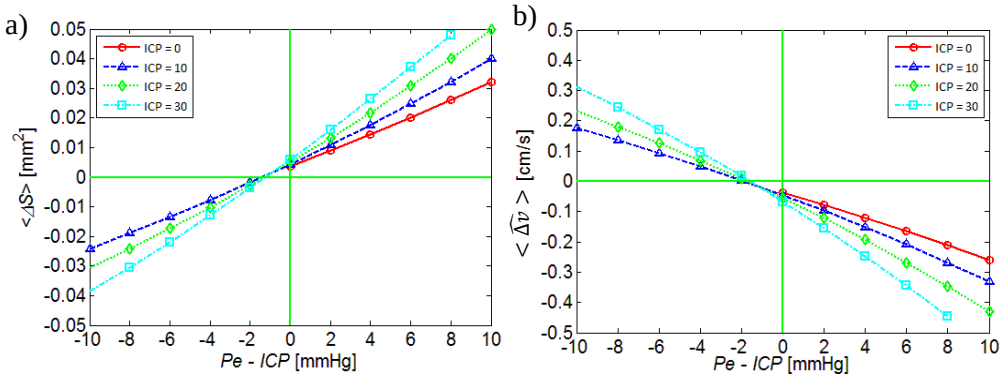

Fig. 33. a) Over a heartbeat pulse period averaged cross-sectional area difference between A and B cross-sections $\widehat{\Delta S}$ dependence on ICP and Pe, b) Over a heartbeat pulse period and surface averaged blood flow velocity difference between A and B cross-sections $< \widehat{\Delta v} >$ dependence on ICP and Pe

In conclusion, for the straight OA at $ICP = \{10, 20, 30\}$ mmHg the systematic deviations of the nICP method estimated based on ΔS and $< \Delta v >$ was $\{-1.48, -1.37, -1.17\}$ mmHg and $\{1.84, -1.76, -1.625\}$ mmHg, respectively.

3.2.3 Case of the patient-specific OA

3.2.3.1 Model setup

The shape of the patient-specific OA was reconstructed from the MR imaging data based on the method provided in chapter 2.2.1. The obtained shape was prepared for solving with FEM by discretizing it into 19840 finite elements, of which 4800 hexahedral elements were used for the artery wall, 3200 hexahedral elements were used to resolve high blood flow boundary layer gradients and 11840 prism elements were used for the bulk of the blood flow. The fiber structure in the OA wall was defined in the local cylindrical coordinate system based on Eq. (79). The local cylindrical coordinate system was obtained by implementing our proposed *Method I*, which is provided in chapter 2.2.3.4. The graphical representation of aforementioned steps is provided in Fig. 34.

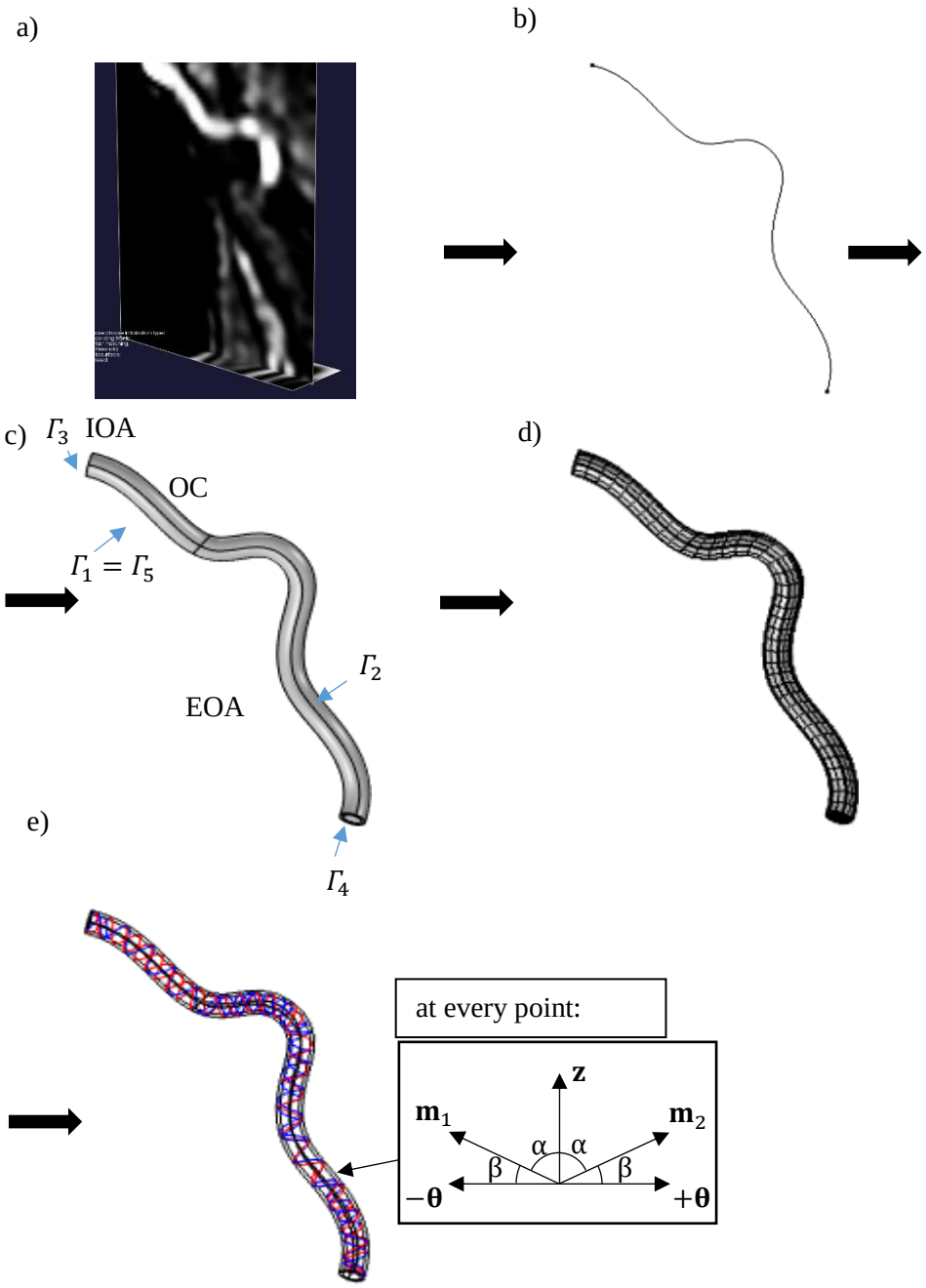

Fig. 34. The process of geometry reconstruction and fiber structure definition in a patient-specific OA: a) the volume of interest that encompasses OA obtained from MR imaging data b) a centerline obtained with VMTK software, c) volumetric OA containing the blood flow domain and a single layered artery wall, d) OA discretized into finite elements, e) the fibrous structure generated at every point in the OA wall

OA geometry was composed of the blood domain Ω_{blood} and OA wall domain Ω_{wall}. Parameters defining the basic material properties of the blood, and of the OA

wall are given in Table 3. As the data of additional parameters, required by constitutive material model for OA wall, are scarce in the scientific literature, ICA parameters were used instead (provided in Table 8), as in case of a straight OA model.

Table 8. OA wall parameters used for fiber-reinforced intact layer model based on ICA wall parameters according to (Sommer et al., 2012)

Arterial wall parameters	**Intact (both *media* and *adventitia*)**
Isotropic, μ, kPa	29.7
Anisotropic, k_1, kPa	27.8
Anisotropic, k_2	64.2
Fiber angle, β, deg	22.0
Dispersion, ϱ, 1	0.8

The OA was prestressed for up to the diastolic pressure of 40 mmHg according to method provided in chapter 2.2.2. The results were obtained from a total of 9 heartbeat pulse periods with $ICP = 10$ mmHg and $Pe = 0{:}18{:}36$ mmHg. The data was saved every 0.004 s. Obtained highest and lowest values of Re and α were close to the values obtained in case of the straight OA.

3.2.3.2 Definition of cross-sections for the data extraction

In case the provided 3D artery shape can be described by the analytical function the definition of the cross-section for the data extraction is a trivial task e.g. the location of the center point of the arbitrary cross-section can be obtained from the analytical function of the parametrized centerline, while the normal can be obtained from the gradient of the centerline at that point. However, in case the analytical expression is unavailable the cross-section definition can become a challenging task, as the normal direction cannot be trivially obtained. In such case we propose to implement the *method I* (presented in chapter 2.2.3.4) to define the curvilinear coordinate system in the lumen volume by prescribing the Dirichlet boundary condition on the lumen inlet and outlet, and Neumann boundary condition on the walls that are in direct contact with the artery wall. The obtained gradient of the scalar field should be a good approximation of the gradient of the centerline that was unavailable in a first place. Now with the gradient and the arbitrary point in the artery domain the cross-section of the patient-specific artery can be defined.

3.2.3.3 Analysis of simulation results

Based on method (presented in 3.2.3.2) four cross-sections of OA denoted as *A*, *B*, *C* and *D* (depicted in Fig. 35) are defined on which the data of characteristic parameters S, p and v were extracted. The results were normalized in the same way as in the case of a straight OA.

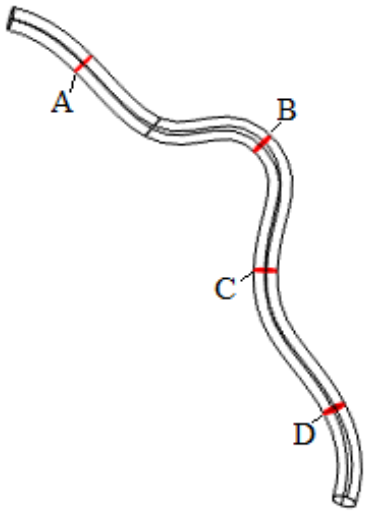

Fig. 35. The cross-sections were data for the analysis was collected

Cross-section *A* is in the OA segment that is affected by *ICP*, cross-sections *B*, *C* and *D* are in the OA segment that is affected by *Pe*. The distance between the cross-section A and the other cross-sections along the OA is denoted as l_i, where $i \in \{1,2,3\} \leftarrow \{l(A,B), l(A,C), l(A,D)\}$. In general l will refer to the distance between nICP measurement locations. The cross-sections B, C and D from the cross-section A are away by an incremental distance $l_i = \{9.03, 15.11, 22.08\}$ mm. In general, the characteristic parameter dependence on the distance between the measurement locations is denoted as follows: Δc_i, where $i \in \{1,2,3\} \leftarrow \{l(A,B), l(A,C), l(A,D)\}$.

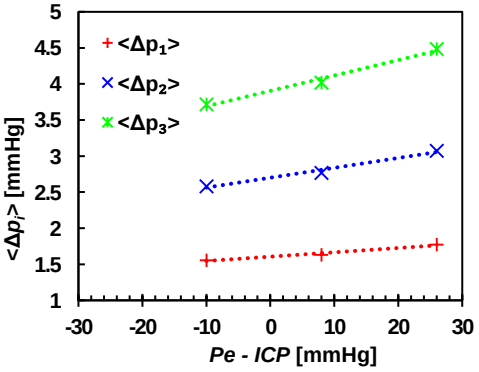

Fig. 36. Over a heartbeat pulse period averaged $< \Delta p_i >$, denoted as $< \widehat{\Delta p_i} >$, dependence on the ICP, Pe and the distance l, were higher index i value indicates greater distance between cross-sections

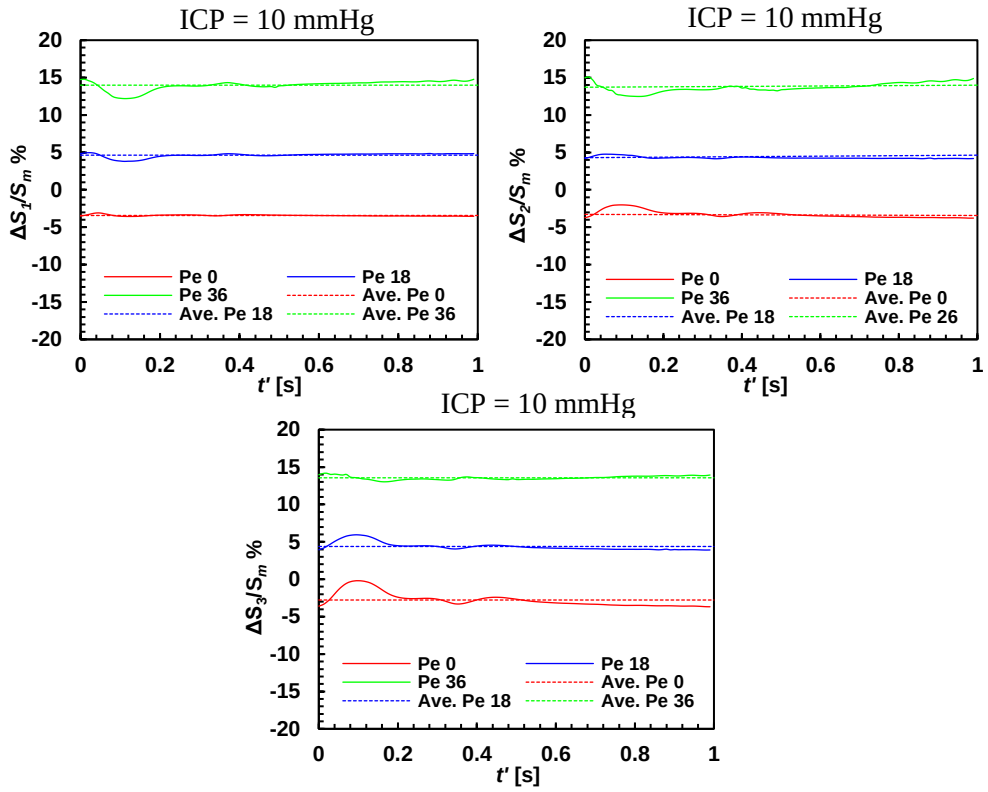

Fig. 37. Cross-sectional area difference ΔS_i and over the heartbeat pulse period averaged ΔS_i, denoted as $\widehat{\Delta S}_i$, dependence on t', ICP, Pe and the distance l were higher index i value indicates greater distance between cross-sections

A heartbeat pulse averaged internal pressure difference $< \Delta p(l) >$, denoted as $< \widehat{\Delta p}(l) >$, dependence on the parameters ICP and Pe at increasing distance l is depicted in Fig. 36. The $< \widehat{\Delta p}(l) >$ increases with the increase in Pe more when the distance between cross-sections in question is higher. This is due to the fact that the larger portion of OA is compressed by the external pressure, which leads to higher decrease in the lumen volume between cross-sections. Based on the Hagen-Poiseuille equation, in order to maintain the same blood flow rate through smaller vessel an increase in blood flow velocity and therefore increase in pressure difference is required, which is in consistence with the results presented in Fig. 36. As $< \Delta p(l) >$ is dependent on the distance between cross-sections, so do other characteristic parameters are dependent not only on the ICP and Pe but also on the $< \Delta p(l) >$ or on the distance l.

ΔS and $\widehat{\Delta S}$ dependence on the t', ICP and Pe is shown in Fig. 37. From Fig. 37 it can be seen that the value of $Pe - ICP$, at which the inversion of ΔS_i occurs with respect to the time axis t' depends on the distance l. From Fig. 38 a) it can be seen that there exists a unique $\min(\mathrm{SD}_{\Delta S_i})$ value at a certain values of distance l and $Pe - ICP$. When increasing the distance l, $\min(\mathrm{SD}_{\Delta S_i})$ shifts towards higher $Pe - ICP$

b)

value (Fig. 38 b), which means that there exists a distance l at which $\min(\mathrm{SD}_{\Delta S_i})$ will be reached when $Pe = ICP$. This is due to the non-linear constitutive OA wall material model as the artery compliance change due to changes in acting external forces.

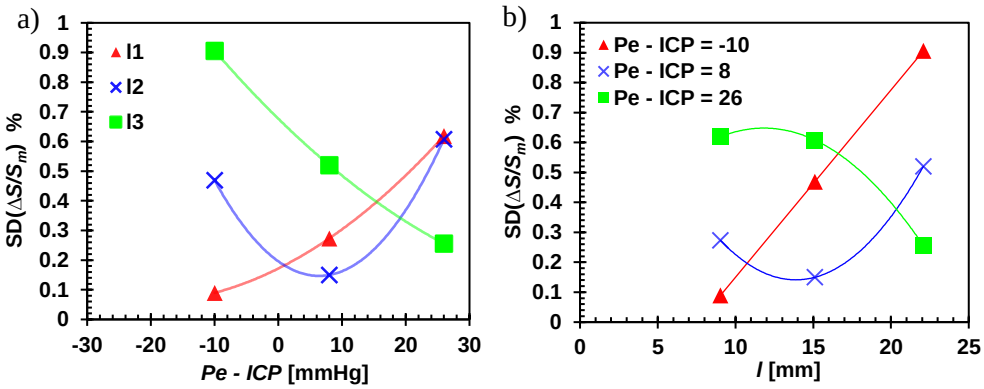

Fig. 38. The dependence of the standard deviation of the ΔS_i on *Pe*, *ICP* and the distance l: a) shows how $\mathrm{SD}_{\Delta S_i}$ changes at a certain distance l when changing *Pe – ICP*, b) shows how $\mathrm{SD}_{\Delta S_i}$ changes given a certain *Pe – ICP* value and changing the distance l

The standard deviation of the ΔS_i approaches the lowest value depending on the value of $< \widehat{\Delta p_i} >$. Since the value of Pe is known, and if the distance l or $< \widehat{\Delta p_i} >$ is also known, at which the standard deviation of the ΔS_i is the lowest, e.g. $\mathrm{SD}_{\Delta S_i} = \min(\mathrm{SD}_{\Delta S_i})$, *ICP* can be obtained based on the result shown in Fig. 39. Plus marks in Fig. 39 indicate a situation when $\mathrm{SD}_{\Delta S_i} = \min(\mathrm{SD}_{\Delta S_i})$.

The surface averaged blood flow velocity difference $< \Delta v_i >$ and over the heartbeat pulse period averaged $< \Delta v_i >$, denoted as $< \widehat{\Delta v_i} >$, dependence on t', ICP and Pe at the increasing distance l is shown in Fig. 40.

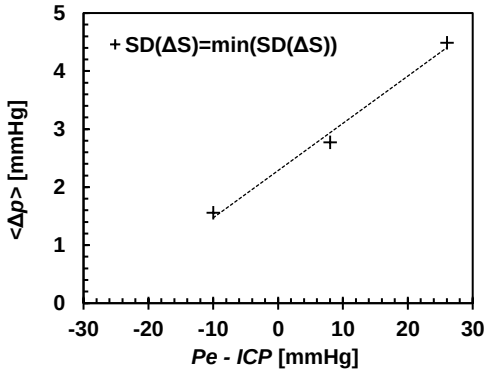

Fig. 39. Over a heartbeat pulse period averaged $< \Delta p >$, denoted as $< \widehat{\Delta p} >$, dependence on the ICP and Pe. The plus sign represents the situation, in which $\mathrm{SD}_{\Delta S_i} = \min(\mathrm{SD}_{\Delta S_i})$

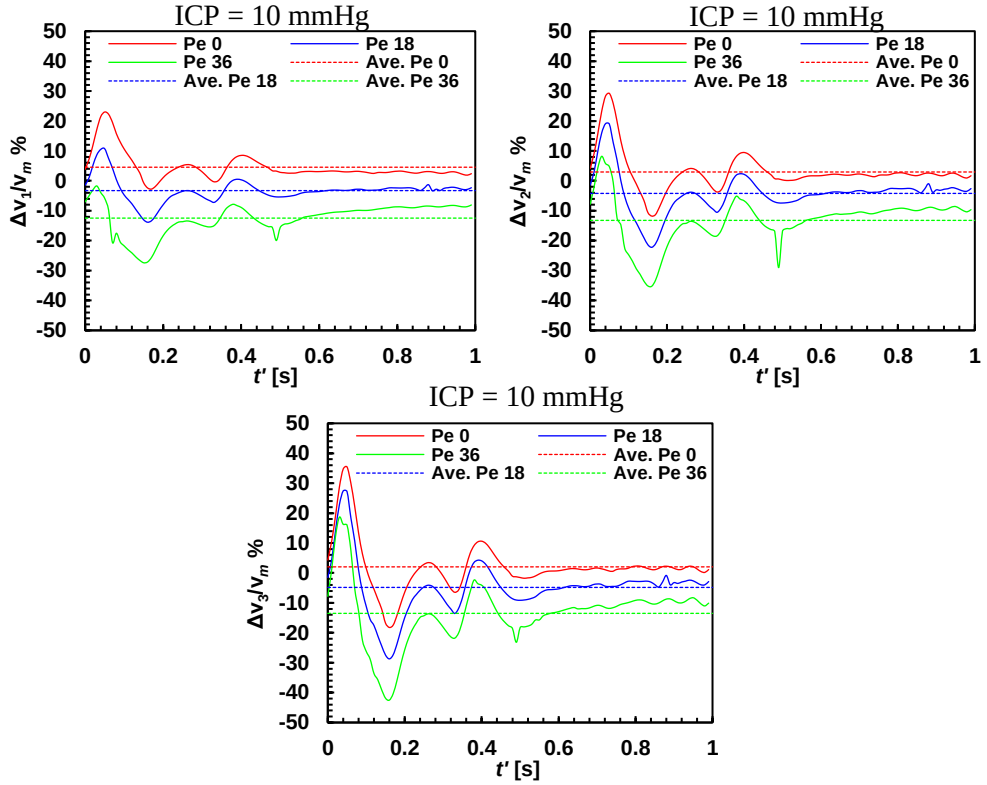

Fig. 40. Surface averaged blood flow velocity difference denoted as $< \Delta v_i >$, and over a heartbeat pulse period averaged $< \Delta v_i >$, denoted as $< \widehat{\Delta v_i} >$, dependence on t', ICP, Pe and the distance l, were higher index i value indicates greater distance between cross-sections

From Fig. 40 it can be seen that unlike the case of ΔS_i, there is no inversion of $< \Delta v_i >$ with respect to the time axis t', when changing the value of $Pe - ICP$. Decreasing the distance l, standard deviation of the $< \Delta v_i >$ decreases and the inversion of $< \Delta v_i >$ with respect to the time axis t' is expected at $l = 0$ mm (Fig. 41). Due to the compliant artery wall there exists a momentary difference in blood flow rate between the cross-sections under consideration. As the distance between cross-sections increases, the dynamics of blood flow rate shifts in time, resulting in the dynamics of blood velocity differences seen in Fig. 40. From Fig. 41 it can be seen that the standard deviation of the $< \Delta v_i >$ is proportional to the distance l.

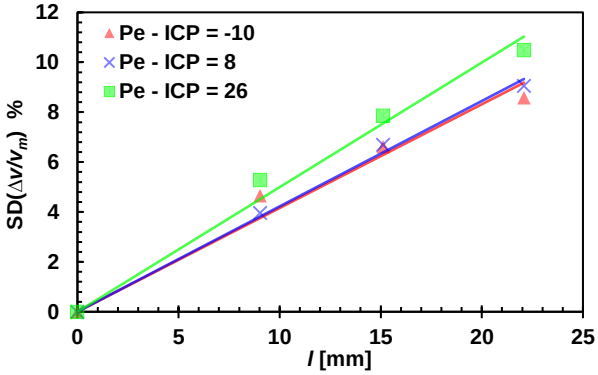

Fig. 41. The dependence of the standard deviation of the $< \Delta v_i >$ on *Pe*, *ICP* and the distance l

The dependence of $\widehat{\Delta S_i}$ and $< \widehat{\Delta v_i} >$ on ICP, Pe and the distance between cross-sections is shown in Fig. 42 a) and Fig. 42 b), respectively. ε_{S_i} and ε_{v_i} are determined by finding the intersection point between the curve of characteristic parameter and the corresponding axis. In this way $\varepsilon_{S_i} = \{-2.18, -2.24, -2.99\}$ mmHg and $\varepsilon_{v_i} = \{-0.04, -2.83, -4.63\}$ mmHg. In case of a rigid artery when $\widehat{\Delta S_i} = 0$ then $< \widehat{\Delta v_i} > = 0$, however in case of a compliant artery the blood capacity between cross-sections in question may increase or decrease. When integrated over a one heartbeat pulse period it turned out that the blood flow rate difference between cross-sections may be non-zero, leading to the difference in systematic errors. Therefore, we denote systematic error due to compliance as ε_{k_i} and define it as follows: $\varepsilon_{k_i} = \varepsilon_{v_i} - \varepsilon_{S_i} = \{2.14, -0.59, -1.64\}$ mmHg.

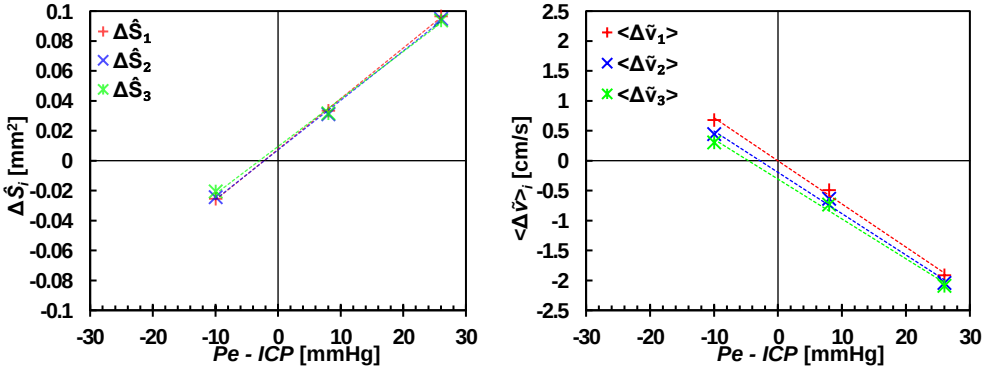

Fig. 42. a) Over a heartbeat pulse period averaged cross-sectional area difference $\widehat{\Delta S_i}$ dependence on ICP, Pe and the distance l. b) Over a heartbeat pulse period and surface averaged blood flow velocity difference $< \widehat{\Delta v_i} >$ dependence on ICP, Pe and the distance l. Higher index i value indicates greater distance between cross-sections

The mechanical non-equivalence due to difference in the curvature and in the boundary conditions between cross-sections leads to the difference in the internal stress distribution, which produces another source of deviation (Misiulis et al., 2016).

The deviation due to mechanical non-equivalence from Fig. 42 a) at $\widehat{\Delta S_i} = 0$ and at different distances is equal to $p_{add_i} = (-0.59, 0.43, 0.85)$ mmHg.

All effects influencing the systematic deviation except the arterial pressure difference can affect it in both ways (reduce it or increase it) and this may explain the low systematic errors obtained in experimental studies by other authors (Ragauskas et al., 2012).

In conclusion, for the patient-specific OA at the $ICP = 10$ mmHg and for three different measurement distances l, the systematic deviation of the nICP method based on ΔS_i and $< \Delta v_i >$ was $\{-2.18, -2.24, -2.99\}$ mmHg and $\{-0.04, -2.83, -4.63\}$ mmHg, respectively.

3.2.4 Limitations

We provide several key limiting factors of the current investigation below:

1) The resolution of MR imaging data was insufficient to reproduce OA shape with the accuracy required by the investigations, and therefore the OA radius was defined according to data presented in the scientific literature (Polak et al., 2010).
2) A stationary ICP value was prescribed, while in reality ICP is a dynamic function varying in time due to change in posture, brain activity, respiratory functions, etc. (Harary et al., 2018). In addition, it is not known how artificially added external pressure affects the ICP dynamics. In the future, in order to achieve more precise results, the pulsating behavior of ICP should be included and the investigation of how the added external pressure affects the ICP dynamics should be carried out.
3) Outflow resistance was assumed to be proportional to the inlet blood flow, which is used as a first approximation of the eye's vascular net resistance. Next step of the research would be the inclusion of an advanced model of eye's vascular net resistance.
4) ICA material parameters were used for OA, because to the author's knowledge no information on material parameters of OA are present in the scientific literature regarding the fiber-reinforced artery wall model. As soon as OA material parameters are available, in order to increase the precision of the numerical model they should be incorporated.
5) Only passive artery wall mechanical behavior was modeled, while active behavior, which is due to the smooth muscle cell contractions (Coccarelli et al., 2018), should be included in the future.
6) The mechanical behavior of surrounding tissues was not included in the numerical model.

3.3 The scope of the performed research

3.3.1 Fluid flow regime

When modeling the fluid flow it is important to evaluate the Reynolds Re and the Womersley α numbers to properly simulate the pulsating flow. It is widely accepted that when $Re < 2300$ flow is laminar, when $Re > 2900$ is turbulent, and at $2300 < Re < 2900$, the flow is in transition mode.

For the pulsating flow there is a typical phase difference between the pressure gradient and the fluid velocity, which leads to the deviation of the fluid velocity profile from the laminar velocity profile. This can be estimated by the ratio of the time-inertial forces and the viscosity forces described by the non-dimensional Womersley number:

$$\alpha = L\left(\frac{\omega\rho}{\mu_f}\right)^{\frac{1}{2}} \tag{99}$$

The force ratio described by the Womersley number allows us to compare systems, which are of different scales and in which a dynamic flow of fluid occurs. It is widely accepted that when $\alpha \leq 1$ then the pulse rate is low enough and there is plenty of time for a parabolic velocity profile to develop during each cycle. When $\alpha \geq 10$, then the velocity profile becomes relatively flat and the average flow lags behind the pressure gradient by about 90 degrees.

Generally, in various technological systems the flow needs to be analyzed within the wide range of these parameters. However, in our case, under the system in consideration (i.e. blood flow in the ophthalmic artery), based on experimental studies results carried out by different authors on different patients (Chien, 1981, Pries et al., 1992, Rojanapongpun et al., 1993, Kwaan, 2010, Baskurt et al., 2013, Cherry et al., 2013, Jeong et al., 2013, Cho et al., 2014, Tu et al., 2015, Michalinos et al., 2015, Reinhart, 2016) by considering the maximum values of the investigated samples, the Re will not exceed 350, and α will not exceed 1, so we can deduce that the flow mode, due to the inertial and viscosity force ratio, will be laminar, and during each heart pulse cycle the flow will produce a nearly fully developed parabolic velocity profile.

In our study Re ranged from 24 to 129, α ranged from about 0.86. Also, the properties of our blood substance, blood velocity, arterial pressure, and the diameter of the ophthalmic artery corresponded to the average values of a healthy person.

3.3.2 Artery mechanics

To the best of our knowledge, in the scientific literature there is no data on the properties of the ophthalmic artery, but, since the ophthalmic artery bifurcates from the internal carotid artery, we assumed that the elastic properties of the ophthalmic artery are close to those of the internal carotid artery (Gupta et al., 1997, Sommer et al., 2010, 2012). In our research, the passive mechanical behavior of the arterial wall was consistent with the elderly age of (76.8 + - 6.3 years), when atherosclerosis is estimated to be lower than the average. This mechanical behavior was published by

other scientists, who performed experimental tension-inflation tests while maintaining the artery submersed in the 37 °C temperature physiological saline.

From the experimental data published by other scientists on mechanical behavior of internal carotid arteries (Sommer et al., 2010), we observe that although the principal course of stress-strain is similar between arteries, the intra- and inter-variations are also typical. In this research we did not investigated the influence of these variations, as we took the parameters corresponding to the average mechanical behavior of the internal carotid artery (Sommer et al., 2012).

Another important parameter is the patient's age. From other authors' published data (Gupta et al., 1997) we see that arteries for younger people are more compliant than for the elderly. Artery compliance influences the results obtained, so in the future, with more experimental data available, numerical investigations may be performed in a wider range and the dependence of the values we examined on the different compliance of the artery can be determined.

3.3.3 Artery geometry variations

The variations in the shape and path of the ophthalmic artery between different patients is shown by (Hayreh, 1962a, 1962b, 1962c, 2006, Michalinos et al., 2015). Several most frequent shape and path variations can be distinguished. Here we analyzed one ophthalmic artery form that corresponds to one of the most frequent forms.

3.3.4 Variations of intracranial pressure

For a healthy adult in the supine position, normal ICP is in the range between 7 mmHg and 15 mmHg (Steiner et al., 2006), for children between 3 mmHg and 7 mmHg, for term infants from 2 mmHg and 6 mmHg, and for pathological patients, ICP can exceed 25 mmHg (Dunn, 2002). Aforementioned ICP values motivated us to set ICP lower limit to 0 mmHg and upper limit to 30 mmHg.

CONCLUSIONS

After the numerical model of the blood flow of the patient-specific compliant ophthalmic artery was developed, with which the dependencies of the blood flow and of the potential systematic deviations of the non-invasive intracranial pressure measurement method were obtained from the measurement conditions and the characteristics of the blood flow when considering:

- straight ophthalmic artery, when $l = 19$ mm, $ICP_i = \{10, 20, 30\}$ mmHg, $Pe = 0{:}\,2{:}\,38$ mmHg,
- curved (patient-specific) ophthalmic artery, when $l_i = \{9.03, 15.11, 22.08\}$ mm, $ICP = 10$ mmHg, $Pe_i = 0{:}\,18{:}\,36$ mmHg,

following conclusions were made:

1. It was found that the percentage error of the directions of fiber structure defined in the arterial wall of the straight artery by our and other authors' methods in the whole artery wall did not exceed 2.75 %. For the curved artery, the average percentage difference of the fiber directions made by our and other authors' methods did not exceed 17.73% (the lowest did not exceed 0.05%, the highest did not exceed 81.82%). Comparison of the influence on the resulting stresses when the fibers were obtained with different fiber definition methods showed that the percentage difference of the mean circumferential stress within the arterial pressure range from 80 mmHg to 180 mmHg did not exceed 0.1 %. The directions of the fiber structure defined with our method is independent on the arterial wall material model.
2. By increasing the external pressure, the lowest standard deviation of the difference in the cross-sectional area, from over the heartbeat pulse period averaged cross-sectional area difference, is obtained with the higher distance:
   - $\mathrm{SD}_{\Delta S}(l_1, Pe) = \min\left(\mathrm{SD}_{\Delta S}(l_1, Pe)\right)$, kai $Pe = 0$ mmHg ir $l_1 = 9.03$ mm;
   - $\mathrm{SD}_{\Delta S}(l_2, Pe) = \min\left(\mathrm{SD}_{\Delta S}(l_2, Pe)\right)$, kai $Pe = 18$ mmHg ir $l_2 = 15.11$ mm;
   - $\mathrm{SD}_{\Delta S}(l_3, Pe) = \min\left(\mathrm{SD}_{\Delta S}(l_3, Pe)\right)$, kai $Pe = 36$ mmHg ir $l_3 = 22.08$ mm.
3. The standard deviation of the difference in the mean blood flow velocity, from over the heartbeat pulse averaged mean blood flow velocity, is proportional to the distance:
   - $\mathrm{SD}_{<\Delta v>} = C \cdot l$, where C is constant, depending on the values of Pe and ICP.
4. By increasing the added external pressure or with the increasing intracranial pressure, the standard deviation of the mean blood flow velocity difference, from over the heartbeat pulse period averaged mean blood flow velocity difference, increases:
   - $\mathrm{SD}_{<\Delta v>} = \sum_{i=0}^{2} a_i ICP^i + \sum_{i=0}^{2} b_i Pe^i$, where a_i and b_i are constants.
5. By increasing the prescribed intracranial pressure ($ICP = \{10, 20, 30\}$ mmHg), the systematic deviation ε based on the measurement parameters

decreases: the ε based on the cross-sectional area was $\varepsilon_S = \{-1.48, -1.37, -1.17\}$ mmHg, and the ε based on the mean blood flow velocity was $\varepsilon_v = \{-1.84, -1.76, -1.625\}$ mmHg.

6. By increasing the distance between the measurement locations ($l_i = \{9.03, 15.11, 22.08\}$ mm), the systemic error ε based on the measurement parameters increases: the ε based on the cross-sectional area was $\varepsilon_S = \{-2.18, -2.24, -2.99\}$ mmHg, and the ε based on the mean blood flow velocity was $\varepsilon_v = \{-0.04, -2.83, -4.63\}$ mmHg.

REFERENCES

1. AKBAR, N. S. Non-Newtonian model study for blood flow through a tapered artery with a stenosis. *Alexandria Engineering Journal*. 2016, 55(1), 321–329. ISSN 11100168.
2. ALASTRUÉ, V., GARÍA, A., PEÑA, E., RODRÍGUEZ, J. F., MARTÍNEZ, M. A., and DOBLARÉ, M. Numerical framework for patient-specific computational modelling of vascular tissue. *International Journal for Numerical Methods in Biomedical Engineering*. 2010, 26(1), 35–51. ISSN 20407939.
3. ANJNA, A. and RAJANDEEP, K. Review of image segmentation techniques. *International Journal of Advanced Research in Computer Science*. 2017, 8(4), 36–39. ISSN 0094-2405.
4. ANNEREL, S., CLAESSENS, T., DEGROOTE, J., SEGERS, P., and VIERENDEELS, J. Validation of a numerical FSI simulation of an aortic BMHV by in vitro PIV experiments. *Medical Engineering & Physics*. 2014, 36(8), 1014–1023. ISSN 13504533.
5. ANON. *COMSOL Multiphysics: Reference Manual*. v5.1. 2015
6. ANTIGA, L. Patient-specific Modeling of Geometry and Blood Flow in Large Arteries. 2002
7. ANTIGA, L., PICCINELLI, M., BOTTI, L., ENE-IORDACHE, B., REMUZZI, A., and STEINMAN, D. A. An image-based modeling framework for patient-specific computational hemodynamics. *Medical & Biological Engineering & Computing*. 2008, 46(11), 1097–1112. ISSN 0140-0118.
8. APOSTOLIDIS, A. J., MOYER, A. P., and BERIS, A. N. Non-Newtonian effects in simulations of coronary arterial blood flow. *Journal of Non-Newtonian Fluid Mechanics*. 2015, 233155–165. ISSN 03770257.
9. ASIEDU, D. P., LEE, K., MILLS, G., and KAUFMANN, E. E. A Review of Non-Invasive Methods of Monitoring Intracranial Pressure. *J Neurol Res.* 2014, 4(1), 1–6.
10. AURICCHIO, F., CONTI, M., FERRARA, A., MORGANTI, S., and REALI, A. Patient-specific finite element analysis of carotid artery stenting: a focus on vessel modeling. *International Journal for Numerical Methods in Biomedical Engineering*. 2013, 29(6), 645–664. ISSN 20407939.
11. BABUSKA, I. and SURI, M. On locking and robustness in the finite element method. *SIAM Journal on Numerical Analysis*. 1992, 291261–1293.
12. BADER, H. Dependence of wall stress in the human thoracic aorta on age and pressure. *Circulation research*. 1967, 20(3), 354–361. ISSN 00097330.
13. BALI, A. and SINGH, S. N. A Review on the Strategies and Techniques of Image Segmentation. In: *2015 Fifth International Conference on Advanced Computing & Communication Technologies*. 2015. IEEE, pp. 113–120
14. BALZANI, D., NEFF, P., SCHRÖDER, J., and HOLZAPFEL, G. A. A polyconvex framework for soft biological tissues. Adjustment to experimental data. *International Journal of Solids and Structures*. 2006, 43(20), 6052–6070. ISSN 00207683.

15. BASKURT, O. K. and MEISELMAN, H. J. Erythrocyte aggregation: Basic aspects and clinical importance. *Clinical Hemorheology and Microcirculation*. 2013, 53(1–2), 23–37. ISSN 13860291.
16. BAYER, JASON, D., BEAUMONT, J., and KROL, A. Laplace – Dirichlet Energy Field Specification for Deformable Models. An FEM Approach to Active Contour Fitting. *Annals of Biomedical Engineering*. 2005, 33(9), 1175–1186.
17. BAYER, J. D., BLAKE, R. C., PLANK, G., and TRAYANOVA, N. A. A novel rule-based algorithm for assigning myocardial fiber orientation to computational heart models. *Annals of Biomedical Engineering*. 2012, 40(10), 2243–2254. ISSN 00906964.
18. BENSELAMA, A. M. and MONNIER, J. *Navier-Stokes ALE free surface flow with generalized Navier slip conditions. Droplet impact and attempt using Comsol Multiphysics 3.2*. 2007
19. BERGER, S. A. and JOU, L.-D. Flows in Stenotic Vessels. *Annual Review of Fluid Mechanics*. 2000, 32(1), 347–382. ISSN 0066-4189.
20. BERNSDORF, J. and WANG, D. Non-Newtonian blood flow simulation in cerebral aneurysms. *Computers and Mathematics with Applications*. 2009, 58(5), 1024–1029. ISSN 08981221.
21. BIANCHI, D., MONALDO, E., GIZZI, A., MARINO, M., FILIPPI, S., and VAIRO, G. A FSI computational framework for vascular physiopathology: A novel flow-tissue multiscale strategy. *Medical Engineering & Physics*. 2017, 4725–37. ISSN 13504533.
22. BIANCHI, D., MARINO, M., and VAIRO, G. An integrated computational approach for aortic mechanics including geometric, histological and chemico-physical data. *Journal of Biomechanics*. 2016, 49(12), 2331–2340. ISSN 00219290.
23. BUXTON, R. B., ULUDAĞ, K., DUBOWITZ, D. J., and LIU, T. T. Modeling the hemodynamic response to brain activation. *NeuroImage*. 2004, 23(SUPPL. 1), S220–S233. ISSN 10538119.
24. CAREW, T. E., VAISHNAV, R. N., and PATEL, D. J. Compressibility of the Arterial Wall. *Circulation Research*. 1968, 23(1), 61–68. ISSN 0009-7330.
25. CARLSEN, R. W. and DAPHALAPURKAR, N. P. The importance of structural anisotropy in computational models of traumatic brain injury. *Frontiers in Neurology*. 2015, 6(FEB), 1–6. ISSN 16642295.
26. CHEN, H. and KASSAB, G. S. Microstructure-based constitutive model of coronary artery with active smooth muscle contraction. *Scientific Reports*. 2017, 7(1), 9339. ISSN 2045-2322.
27. CHERRY, E. M. and EATON, J. K. Shear thinning effects on blood flow in straight and curved tubes. *Physics of Fluids*. 2013, 25(7), ISSN 10706631.
28. CHIASTRA, C., MIGLIORI, S., BURZOTTA, F., DUBINI, G., and MIGLIAVACCA, F. Patient-Specific Modeling of Stented Coronary Arteries Reconstructed from Optical Coherence Tomography: Towards a Widespread Clinical Use of Fluid Dynamics Analyses. *Journal of Cardiovascular*

Translational Research. 2017, 11(2), 1–17. ISSN 19375395.
29. CHIEN, S. Determinants of blood viscosity and red cell deformability. *Scandinavian Journal of Clinical and Laboratory Investigation*. 1981, 41(S156), 7–12. ISSN 00365513.
30. CHO, Y. I., CHO, D. J., and ROSENSON, R. S. Endothelial shear stress and blood viscosity in peripheral arterial disease. *Current Atherosclerosis Reports*. 2014, 16(4), ISSN 15346242.
31. CHOMSKIS, R., GEDIMINAS, D., GIANSIRACUSA, R., MOEHRING, M., PETKUS, V., RAGAUSKAS, A., SAXON, E. A., SWEDENBURG, S., and ZAKELIS, R. Method and apparatus for determining the absolute value of intracranial pressure. 2011
32. CHUONG, C. J. and FUNG, Y. C. On Residual Stresses in Arteries. *Journal of Biomechanical Engineering*. 1986, 108(2), 189. ISSN 01480731.
33. COCCARELLI, A., EDWARDS, D. H., AGGARWAL, A., NITHIARASU, P., and PARTHIMOS, D. A multiscale active structural model of the arterial wall accounting for smooth muscle dynamics. *Journal of The Royal Society Interface*. 2018, 15(139), 20170732. ISSN 1742-5689.
34. COMSOL MULTIPHYSICS. Structural mechanics module: user's guide. *Manual*. 2015, 706.
35. CUTNELL, J. D. and JOHNSON, K. W. *Physics*. 4 th. 1997. John Wiley & Sons Inc
36. DASHTI, S. R., BAHARVAHDAT, H., SPETZLER, R. F., SAUVAGEAU, E., CHANG, S. W., STIEFEL, M. F., PARK, M. S., and BAMBAKIDIS, N. C. Operative intracranial infection following craniotomy. *Neurosurgical Focus*. 2008, 24(6), E10. ISSN 1092-0684.
37. DELFINO, A., STERGIOPULOS, N., MOORE, J. E., and MEISTER, J. J. Residual strain effects on the stress field in a thick wall finite element model of the human carotid bifurcation. *Journal of Biomechanics*. 1997, 30(8), 777–786. ISSN 00219290.
38. DIMOV, I., FARAGÓ, I., EDS, L. V., and HUTCHISON, D. *Finite Difference Methods. Theory and Applications*. 1st ed. 2018. Springer International Publishing
39. DOOST, S. N., ZHONG, L., SU, B., and MORSI, Y. S. The numerical analysis of non-Newtonian blood flow in human patient-specific left ventricle. *Computer Methods and Programs in Biomedicine*. 2016, 127232–247. ISSN 18727565.
40. DUNN, L. T. Raised intracranial pressure. *Journal of Neurosurgical Psychiatry*. 2002, 73(Suppl I), i23–i27. ISSN 0022-3050.
41. DUNN, M. L. Application of A Microstructural Constitutive Model of the Pulmonary Artery to Patient-Specific Studies: Validation and Effect of Orthotropy. *Journal of Biomechanical Engineering*. 2006, 129(2), 193. ISSN 0148-0731.
42. EL-BOURI, W. K. and PAYNE, S. J. Multi-scale homogenization of blood flow in 3-dimensional human cerebral microvascular networks. *Journal of Theoretical Biology*. 2015, 38040–47. ISSN 10958541.

43. EL-BOURI, W. K. and PAYNE, S. J. A statistical model of the penetrating arterioles and venules in the human cerebral cortex. *Microcirculation*. 2016, 23(7), 580–590. ISSN 15498719.
44. ELKENANI, H., AL-BAHKALI, E., and SOULI, M. Numerical Investigation of Pulse Wave Propagation in Arteries Using Fluid Structure Interaction Capabilities. *Computational and Mathematical Methods in Medicine*. 2017, 20171–7. ISSN 1748-670X.
45. EYRE, D. R., WEIS, M. A., and WU, J. J. Advances in collagen cross-link analysis. *Methods*. 2008, 45(1), 65–74. ISSN 10462023.
46. FORCADEL, N., LE GUYADER, C., and GOUT, C. Generalized fast marching method: applications to image segmentation. *Numerical Algorithms*. 2008, 48(1–3), 189–211. ISSN 1017-1398.
47. FORTIER, A., GULLAPALLI, V., and MIRSHAMS, R. A. Review of biomechanical studies of arteries and their effect on stent performance. *IJC Heart and Vessels*. 2014, 4(1), 12–18. ISSN 22147632.
48. FUNG, Y. C., FRONEK, K., and PATITUCCI, P. Pseudoelasticity of arteries and the choice of its mathematical expression. *American Journal of Physiology-Heart and Circulatory Physiology*. 1979, 237(5), H620–H631. ISSN 0363-6135.
49. GASSER, T. C., OGDEN, R. W., and HOLZAPFEL, G. A. Hyperelastic modelling of arterial layers with distributed collagen fibre orientations. *Journal of the Royal Society Interface*. 2006, 3(6), 15–35. ISSN 17425662.
50. GEE, M. W., REEPS, C., ECKSTEIN, H. H., and WALL, W. A. Prestressing in finite deformation abdominal aortic aneurysm simulation. *Journal of Biomechanics*. 2009, 42(11), 1732–1739. ISSN 00219290.
51. GEE, M. W., FÖRSTER, C., and WALL, W. A. A computational strategy for prestressing patient-specific biomechanical problems under finite deformation. *International Journal for Numerical Methods in Biomedical Engineering*. 2010, 26(1), 52–72. ISSN 20407939.
52. GIBOU, F., FEDKIW, R., and OSHER, S. A review of level-set methods and some recent applications. *Journal of Computational Physics*. 2018, 35382–109. ISSN 00219991.
53. GOULD, I. G., TSAI, P., KLEINFELD, D., and LINNINGER, A. The capillary bed offers the largest hemodynamic resistance to the cortical blood supply. *Journal of Cerebral Blood Flow and Metabolism*. 2017, 37(1), 52–68. ISSN 15597016.
54. GOVINDJEE, S. and MIHALIC, P. A. Computational methods for inverse deformations in quasi-incompressible finite elasticity. *International Journal for Numerical Methods in Engineering*. 1998, 43(5), 821–838. ISSN 0029-5981.
55. GUPTA, B. S. and KASYANOV, V. A. Biomechanics of human common carotid artery and design of novel hybrid textile compliant vascular grafts. *Journal of Biomedical Materials Research*. 1997, 34(3), 341–349. ISSN 00219304.

56. HARARY, M., DOLMANS, R. G. F., and GORMLEY, W. Intracranial Pressure Monitoring—Review and Avenues for Development. *Sensors*. 2018, 18(2), 465. ISSN 1424-8220.
57. HARGENS, A. R., BHATTACHARYA, R., and SCHNEIDER, S. M. Space physiology VI: exercise, artificial gravity, and countermeasure development for prolonged space flight. *European Journal of Applied Physiology*. 2013, 113(9), 2183–2192. ISSN 1439-6319.
58. HAYREH, S. S. The ophthalmic artery I: origin and intra-cranial and intra-canalicular course. *British Journal of Ophthalmology*. 1962a
59. HAYREH, S. S. The ophthalmic artery: II intraorbital course. *British Journal of Ophthalmology*. 1962b, 165–185.
60. HAYREH, S. S. The ophthalmic artery: III. branches. *British Journal of Ophthalmology*. 1962c, 46(4), 212–247. ISSN 0007-1161.
61. HAYREH, S. S. Orbital vascular anatomy. *Eye*. 2006, 20(10), 1130–1144. ISSN 0950-222X.
62. HELFENSTEIN, J., JABAREEN, M., MAZZA, E., and GOVINDJEE, S. On non-physical response in models for fiber-reinforced hyperelastic materials. *International Journal of Solids and Structures*. 2010, 47(16), 2056–2061. ISSN 00207683.
63. HICKMAN, K. M., MAYER, B. L., and MUWASWES, M. Intracranial pressure monitoring: review of risk factors associated with infection. *Heart & lung : the journal of critical care*. 1990, 19(1), 84–90. ISSN 0147-9563.
64. HO, H., MCGHEE, C., and HUNTER, P. Numerical analysis for the blood flow in a patient-specific ophthalmic artery. *Medical Engineering & Physics*. 2012, 34(1), 123–127. ISSN 13504533.
65. HOLDSWORTH, D. W., NORLEY, C. J. D., FRAYNE, R., STEINMAN, D. A., and RUTT, B. K. Characterization of common carotid artery blood-flow waveforms in normal human subjects. *Physiological Measurement*. 1999, 20(3), 219–240. ISSN 0967-3334.
66. HOLZAPFEL, G. Nonlinear solid mechanics: A continuum approach for engineering. *John Wiley & Sons*. 2000, 455. ISSN 1572-9648.
67. HOLZAPFEL, G. A., SOMMER, G., GASSER, C. T., and REGITNIG, P. Determination of layer-specific mechanical properties of human coronary arteries with nonatherosclerotic intimal thickening and related constitutive modeling. *American Journal of Physiology-Heart and Circulatory Physiology*. 2005, 289(5), H2048–H2058. ISSN 0363-6135.
68. HOLZAPFEL, G. A., GASSER, T. C., and OGDEN, R. W. A New Constitutive Framework for Arterial Wall Mechanics and a Comparative Study of Material Models. *Journal of Elasticity*. 2000, 61(1/3), 1–48. ISSN 03743535.
69. HOLZAPFEL, G. A. and OGDEN, R. W. Constitutive modelling of passive myocardium: A structurally based framework for material characterization. *Philosophical Transactions of the Royal Society A: Mathematical, Physical and Engineering Sciences*. 2009, 367(1902), 3445–3475. ISSN 1364503X.
70. HSU, M.-C. and BAZILEVS, Y. Blood vessel tissue prestress modeling for

vascular fluid–structure interaction simulation. *Finite Elements in Analysis and Design*. 2011, 47(6), 593–599. ISSN 0168874X.
71. HUMPHREY, J. D. and NA, S. Elastodynamics and arterial wall stress. *Annals of Biomedical Engineering*. 2002, 30(4), 509–523. ISSN 00906964.
72. HUYGHE, J. M., VAN CAMPEN, D. H., ARTS, T., and HEETHAAR, R. M. A two-phase finite element model of the diastolic left ventricle. *Journal of Biomechanics*. 1991, 24(7), 527–538. ISSN 00219290.
73. JEONG, S. K. and ROSENSON, R. S. Shear rate specific blood viscosity and shear stress of carotid artery duplex ultrasonography in patients with lacunar infarction. *BMC Neurology*. 2013, 13ISSN 14712377.
74. JUNG, J. and HASSANEIN, A. Three-phase CFD analytical modeling of blood flow. *Medical Engineering & Physics*. 2008, 30(1), 91–103. ISSN 13504533.
75. JUNG, J., HASSANEIN, A., and LYCZKOWSKI, R. W. Hemodynamic Computation Using Multiphase Flow Dynamics in a Right Coronary Artery. *Annals of Biomedical Engineering*. 2006, 34(3), 393–407. ISSN 0090-6964.
76. KALTENBACHER, M. *Numerical Simulation of Mechatronic Sensors and Actuators*. 2015. Berlin, Heidelberg: Springer Berlin Heidelberg
77. KAMENSKIY, A. V., DZENIS, Y. A., MACTAGGART, J. N., LYNCH, T. G., JAFFAR KAZMI, S. A., and PIPINOS, I. I. Nonlinear Mechanical Behavior of The Human Common, External, and Internal Carotid Arteries In Vivo. *Journal of Surgical Research*. 2012, 176(1), 329–336. ISSN 00224804.
78. KARAJAN, N., EHLERS, W., MARKERT, B., ACARTÜRK, A., and WIENERS, C. FE Treatment of InhomogeneitiesWithin the Intervertebral Disc. *PAMM*. 2005, 5(1), 237–238. ISSN 1617-7061.
79. KARIMI, S., DABAGH, M., VASAVA, P., DADVAR, M., DABIR, B., and JALALI, P. Effect of rheological models on the hemodynamics within human aorta: CFD study on CT image-based geometry. *Journal of Non-Newtonian Fluid Mechanics*. 2014, 20742–52. ISSN 03770257.
80. KAWOOS, U., MCCARRON, R., AUKER, C., and CHAVKO, M. Advances in Intracranial Pressure Monitoring and Its Significance in Managing Traumatic Brain Injury. *International Journal of Molecular Sciences*. 2015, 16(12), 28979–28997. ISSN 1422-0067.
81. KHAMDAENG, T., LUO, J., VAPPOU, J., TERDTOON, P., and KONOFAGOU, E. E. Arterial stiffness identification of the human carotid artery using the stress–strain relationship in vivo. *Ultrasonics*. 2012, 52(3), 402–411. ISSN 0041624X.
82. KHAN, S., RAHMANI, H., SHAH, S. A. A., and BENNAMOUN, M. A Guide to Convolutional Neural Networks for Computer Vision. *Synthesis Lectures on Computer Vision*. 2018, 8(1), 1–207. ISSN 2153-1056.
83. KIOUSIS, D. E., RUBINIGG, S. F., AUER, M., and HOLZAPFEL, G. A. A Methodology to Analyze Changes in Lipid Core and Calcification Onto Fibrous Cap Vulnerability: The Human Atherosclerotic Carotid Bifurcation as an Illustratory Example. *Journal of Biomechanical Engineering*. 2009,

131(12), 121002. ISSN 01480731.
84. KRAKAUSKAITE, S., PETKUS, V., BARTUSIS, L., ZAKELIS, R., CHOMSKIS, R., PREIKSAITIS, A., RAGAUSKAS, A., MATIJOSAITIS, V., PETRIKONIS, K., and RASTENYTE, D. *Intracranial Pressure and Brain Monitoring XV*. Intracranial Pressure and Brain Monitoring XV. 2016. Cham: Springer International Publishing
85. KUHL, E., MAAS, R., HIMPEL, G., and MENZEL, A. Computational modeling of arterial wall growth : Attempts towards patient-specific simulations based on computer tomography. *Biomechanics and Modeling in Mechanobiology*. 2007, 6(5), 321–331. ISSN 16177959.
86. KWAAN, H. C. Role of plasma proteins in whole blood viscosity: A brief clinical review. *Clinical Hemorheology and Microcirculation*. 2010, 44(3), 167–176. ISSN 13860291.
87. LANGHAM, M. E. *Ischemia and loss of vascular autoregulation in ocular and cerebral diseases: A new perspective*. Ischemia and Loss of Vascular Autoregulation in Ocular and Cerebral Diseases: A New Perspective. 2009. New York, NY: Springer New York
88. LENG, X., CHEN, X., DENG, X., SUTTON, M. A., and LESSNER, S. M. Modeling of Experimental Atherosclerotic Plaque Delamination. *Annals of Biomedical Engineering*. 2015, 43(12), 2838–2851. ISSN 15739686.
89. LENG, X., ZHOU, B., DENG, X., DAVIS, L., LESSNER, S. M., SUTTON, M. A., and SHAZLY, T. Experimental and numerical studies of two arterial wall delamination modes. *Journal of the Mechanical Behavior of Biomedical Materials*. 2018, 77(September 2017), 321–330. ISSN 18780180.
90. LI, D. and ROBERTSON, A. M. A structural multi-mechanism constitutive equation for cerebral arterial tissue. *International Journal of Solids and Structures*. 2009, 46(14–15), 2920–2928. ISSN 00207683.
91. LI, K., OGDEN, R. W., and HOLZAPFEL, G. A. Computational method for excluding fibers under compression in modeling soft fibrous solids. *European Journal of Mechanics, A/Solids*. 2016, 57178–193. ISSN 09977538.
92. LIU, X., ZHOU, C., ZHANG, G., LIN, Y., and LI, S. CT anatomic measurement of the optic canal and its clinical significance. *Zhonghua Er Bi Yan Hou Ke Za Zhi*. 2000, 35(4), 275–7.
93. LIU, X., FAN, Y., DENG, X., and ZHAN, F. Effect of non-Newtonian and pulsatile blood flow on mass transport in the human aorta. *Journal of Biomechanics*. 2011, 44(6), 1123–1131. ISSN 00219290.
94. LORTHOIS, S., CASSOT, F., and LAUWERS, F. Simulation study of brain blood flow regulation by intra-cortical arterioles in an anatomically accurate large human vascular network: Part I: Methodology and baseline flow. *NeuroImage*. 2011, 54(2), 1031–1042. ISSN 10538119.
95. MAAS, S. A., ERDEMIR, A., HALLORAN, J. P., and WEISS, J. A. A general framework for application of prestrain to computational models of biological materials. *Journal of the Mechanical Behavior of Biomedical Materials*. 2016, 61499–510. ISSN 18780180.
96. MACRAE, R. A., MILLER, K., and DOYLE, B. J. Methods in Mechanical

Testing of Arterial Tissue: A Review. *Strain*. 2016, 52(5), 380–399. ISSN 14751305.
97. MANDEVILLE, J. B., MAROTA, J. J. A., AYATA, C., ZAHARCHUK, G., MOSKOWITZ, M. A., ROSEN, B. R., and WEISSKOFF, R. M. Evidence of a cerebrovascular postarteriole windkessel with delayed compliance. *Journal of Cerebral Blood Flow and Metabolism*. 1999, 19(6), 679–689. ISSN 0271678X.
98. MARINO, M. Elasto-Damage Modeling of Biopolymer Molecules Response. 2012, (June 2014),
99. MARRERO, V. L., TICHY, J. A., SAHNI, O., and JANSEN, K. E. Numerical Study of Purely Viscous Non-Newtonian Flow in an Abdominal Aortic Aneurysm. *Journal of Biomechanical Engineering*. 2014, 136(10), 101001. ISSN 0148-0731.
100. MICHALINOS, A., ZOGANA, S., KOTSIOMITIS, E., MAZARAKIS, A., and TROUPIS, T. Anatomy of the Ophthalmic Artery: A Review concerning Its Modern Surgical and Clinical Applications. *Anatomy Research International*. 2015, 20151–8. ISSN 2090-2743.
101. MILNOR, W. R. *Cardiovascular Physiology*. ed. 1. 1990. New York, NY: Oxford University Press
102. MISIULIS, E., DŽIUGYS, A., NAVAKAS, R., and STRIŪGAS, N. A fluid-structure interaction model of the internal carotid and ophthalmic arteries for the noninvasive intracranial pressure measurement method. *Computers in Biology and Medicine*. 2017, 84(March), 79–88. ISSN 18790534.
103. MISIULIS, E., DŽIUGYS, A., NAVAKAS, R., and PETKUS, V. A comparative study of methods used to generate the arterial fiber structure in a clinically relevant numerical analysis. *International Journal for Numerical Methods in Biomedical Engineering*. 2019, e3194. ISSN 2040-7939.
104. MISIULIS, E. and DŽIUGYS, A. Effect of geometrical shape and boundary conditions on the stress distribution and deformations in ophthalmic artery numerical model. *13th Annual international conference of young scientists on energy issues (CYSENI 2016)*. 2016, 363–370.
105. MISIULIS, E., SKARBALIUS, G., and DŽIUGYS, A. Numerical evaluation of systematic errors of a non-invasive intracranial pressure measurement. *Energetika*. 2018, 64(3), 121–136. ISSN 1822-8836.
106. MOKRI, B. The Monro-Kellie hypothesis: Applications in CSF volume depletion. *Neurology*. 2001, 56(12), 1746–1748. ISSN 0028-3878.
107. MONTALVO NAVARRETE, J. I., HIDALGO-SALAZAR, M. A., ESCOBAR NUNEZ, E., and ROJAS ARCINIEGAS, A. J. Thermal and mechanical behavior of biocomposites using additive manufacturing. *International Journal on Interactive Design and Manufacturing (IJIDeM)*. 2017, 12(2), 449–458. ISSN 1955-2513.
108. NAKAMURA, M., BESSHO, S., and WADA, S. Spring-network-based model of a red blood cell for simulating mesoscopic blood flow. *International Journal for Numerical Methods in Biomedical Engineering*. 2013, 29(1), 114–

128. ISSN 20407939.
109. NEWMAN, T. S. and YI, H. A survey of the marching cubes algorithm. *Computers & Graphics*. 2006, 30(5), 854–879. ISSN 00978493.
110. NICHOLS, W. W., O'ROURKE, M. F., and VLACHOPOULOS, C. *McDonald's Blood Flow in Arteries, 6th ed: Theoretical, Experimental and Clinical Principles*. 2011. Hodder Arnold Publishers
111. NOLAN, D. R., GOWER, A. L., DESTRADE, M., OGDEN, R. W., and MCGARRY, J. P. A robust anisotropic hyperelastic formulation for the modelling of soft tissue. *Journal of the Mechanical Behavior of Biomedical Materials*. 2014a, 3948–60. ISSN 17516161.
112. NOLAN, D. R., GOWER, A. L., DESTRADE, M., OGDEN, R. W., and MCGARRY, J. P. A robust anisotropic hyperelastic formulation for the modelling of soft tissue. *Journal of the Mechanical Behavior of Biomedical Materials*. 2014b, 3948–60. ISSN 18780180.
113. NOLAN, D. R. and MCGARRY, J. P. On the Compressibility of Arterial Tissue. *Annals of Biomedical Engineering*. 2016, 44(4), 993–1007. ISSN 0090-6964.
114. OGDEN, R. W. *Non-linear elastic deformations*. 1997
115. OSWAL, A. and TOMA, A. K. Intracranial pressure and cerebral haemodynamics. *Anaesthesia and Intensive Care Medicine*. 2017, 18(5), 259–263. ISSN 18787584.
116. PADAYACHY, L. C. Non-invasive intracranial pressure assessment. *Child's Nervous System*. 2016, 32(9), 1587–1597. ISSN 0256-7040.
117. PAYNE, S. J. and LUCAS, C. Oxygen delivery from the cerebral microvasculature to tissue is governed by a single time constant of approximately 6 seconds. *Microcirculation*. 2018, 25(2), e12428. ISSN 15498719.
118. POLAK, J. F., PENCINA, M. J., MEISNER, A., PENCINA, K. M., BROWN, L. S., WOLF, P. A., and D'AGOSTINO, R. B. Associations of carotid artery intima-media thickness (IMT) with risk factors and prevalent cardiovascular disease: comparison of mean common carotid artery IMT with maximum internal carotid artery IMT. *Journal of ultrasound in medicine*. 2010, 29(12), 1759–68. ISSN 1550-9613.
119. PRIES, A. R., NEUHAUS, D., and GAEHTGENS, P. Blood viscosity in tube flow: dependence on diameter and hematocrit. *The American journal of physiology*. 1992, 263(6 Pt 2), H1770-8. ISSN 0002-9513.
120. PUNTIS, M., REDDY, U., and HIRSCH, N. Cerebrospinal fluid and its physiology. *Anaesthesia and Intensive Care Medicine*. 2016, 17(12), 611–612. ISSN 18787584.
121. RABOEL, P. H., BARTEK, J., ANDRESEN, M., BELLANDER, B. M., and ROMNER, B. Intracranial Pressure Monitoring: Invasive versus Non-Invasive Methods—A Review. *Critical Care Research and Practice*. 2012, 20121–14. ISSN 2090-1305.
122. RAGAUSKAS, A., DAUBARIS, G., DZIUGYS, A., AZELIS, V., and GEDRIMAS, V. Innovative non-invasive method for absolute intracranial

pressure measurement without calibration. *Acta neurochirurgica. Supplement*. 2005, 95(95), 357–61. ISSN 0065-1419.
123. RAGAUSKAS, A., MATIJOSAITIS, V., PIPER, I., and DAUBARIS, G. Clinical assessment of noninvasive intracranial pressure absolute value measurement method. *American Academy of Neurology*. 2012, 78(232545), 1684–1691. ISSN 0028-3878.
124. RAGAUSKAS, A., PETKUS, V., CHOMSKIS, R., ZAKELIS, R., DAUBARIS, G., MOEHRING, M., SAXON, E. A., GIANSIRACUSA, R., SWEDENBURG, S., and RAISUTIS, R. Method and apparatus for determining the absolute value of intracranial pressure. 2013
125. RAGAUSKAS, A., DAUBARIS, G., and DZIUGYS, A. Method and apparatus for determining the pressure inside the brain. 1999
126. RAJESH, A., KINGSTON-HEPNER, M., and KRISHNAKUMAR, D. Raised intracranial pressure. *Paediatrics and Child Health (United Kingdom)*. 2017, 27(6), 260–267. ISSN 1878206X.
127. RAZAVI, A., SHIRANI, E., and SADEGHI, M. R. Numerical simulation of blood pulsatile flow in a stenosed carotid artery using different rheological models. *Journal of Biomechanics*. 2011, 44(11), 2021–2030. ISSN 00219290.
128. REINHART, W. H. The optimum hematocrit. *Clinical Hemorheology and Microcirculation*. 2016, 64(4), 575–585. ISSN 18758622.
129. RILEY, W. A., BARNES, R. W., EVANS, G. W., and BURKE, G. L. Ultrasonic measurement of the elastic modulus of the common carotid artery. The Atherosclerosis Risk in Communities (ARIC) Study. *Stroke*. 1992, 23(7), 952–956. ISSN 0039-2499.
130. ROCCABIANCA, S., BELLINI, C., and HUMPHREY, J. D. Computational modelling suggests good, bad and ugly roles of glycosaminoglycans in arterial wall mechanics and mechanobiology. *Journal of The Royal Society Interface*. 2014, 11(97), 20140397–20140397. ISSN 1742-5689.
131. RODRÍGUEZ-BOTO, G., RIVERO-GARVÍA, M., GUTIÉRREZ-GONZÁLEZ, R., and MÁRQUEZ-RIVAS, J. Basic concepts about brain pathophysiology and intracranial pressure monitoring. *Neurología*. 2015, 30(1), 16–22. ISSN 02134853.
132. ROJANAPONGPUN, P., DRANCE, S. M., and MORRISON, B. J. Ophthalmic artery flow velocity in glaucomatous and normal subjects. *British Journal of Ophthalmology*. 1993, 77(1), 25–29. ISSN 00071161.
133. ROOZENBEEK, B., MAAS, A. I. R., and MENON, D. K. Changing patterns in the epidemiology of traumatic brain injury. *Nature Reviews Neurology*. 2013, 9(4), 231–236. ISSN 17594758.
134. ROY, D., HOLZAPFEL, G. A., KAUFFMANN, C., and SOULEZ, G. Finite element analysis of abdominal aortic aneurysms: Geometrical and structural reconstruction with application of an anisotropic material model. *IMA Journal of Applied Mathematics (Institute of Mathematics and Its Applications)*. 2014, 79(5), 1011–1026. ISSN 14643634.
135. SCHAAFSMA, A. Harvey with a modern twist: How and why conducting

arteries amplify the pressure wave originating from the heart. *Medical Hypotheses*. 2014, 82(5), 589–594. ISSN 03069877.
136. SEGERS, P., RIETZSCHEL, E. R., DE BUYZERE, M. L., STERGIOPULOS, N., WESTERHOF, N., VAN BORTEL, L. M., GILLEBERT, T., and VERDONCK, P. R. Three-and-four-element Windkessel models: Assessment of their fitting performance in a large cohort of healthy middle-aged individuals. *Proceedings of the Institution of Mechanical Engineers, Part H: Journal of Engineering in Medicine*. 2008, 222(4), 417–428. ISSN 09544119.
137. SIAUDVYTYTE, L., JANULEVICIENE, I., RAGAUSKAS, A., BARTUSIS, L., SIESKY, B., and HARRIS, A. Update in intracranial pressure evaluation methods and translaminar pressure gradient role in glaucoma. *Acta Ophthalmologica*. 2015, 93(1), 9–15. ISSN 17553768.
138. SOMMER, G., REGITNIG, P., KÖLTRINGER, L., HOLZAPFEL, G. a, KOLTRINGER, L., and HOLZAPFEL, G. a. Biaxial mechanical properties of intact and layer-dissected human carotid arteries at physiological and supraphysiological loadings. *American journal of physiology. Heart and circulatory physiology*. 2010, 298(3), H898–H912. ISSN 0363-6135.
139. SOMMER, G. and HOLZAPFEL, G. A. 3D constitutive modeling of the biaxial mechanical response of intact and layer-dissected human carotid arteries. *Journal of the Mechanical Behavior of Biomedical Materials*. 2012, 5(1), 116–128. ISSN 17516161.
140. SONG, M., MA, J., and HUANG, Y. Fluid-structure interaction analysis of ship-ship collisions. *Marine Structures*. 2017, 55121–136. ISSN 09518339.
141. SOULI, M. and BENSON, D. J. *Arbitrary Lagrangian-Eulerian and Fluid-Structure Interaction*. Arbitrary Lagrangian-Eulerian and Fluid-Structure Interaction. 2013. Hoboken, NJ USA: John Wiley & Sons, Inc.
142. STEINER, L. A. and ANDREWS, P. J. D. Monitoring the injured brain: ICP and CBF. *British Journal of Anaesthesia*. 2006, 97(1), 26–38. ISSN 00070912.
143. STUPAK, E., KAČIANAUSKAS, R., KAČENIAUSKAS, A., STARIKOVIČIUS, V., MAKNICKAS, A., PACEVIČ, R., STAŠKŪIENE, M., DAVIDAVIČIUS, G., and AIDIETIS, A. The geometric model-based patient-specific simulations of turbulent aortic valve flows. *Archives of Mechanics*. 2017, 69(4–5), 317–345. ISSN 03732029.
144. SU, S.-W., CATHERALL, M., and PAYNE, S. The Influence of Network Structure on the Transport of Blood in the Human Cerebral Microvasculature. *Microcirculation*. 2012, 19(2), 175–187. ISSN 10739688.
145. TAGHIZADEH, H., TAFAZZOLI-SHADPOUR, M., SHADMEHR, M., and FATOURAEE, N. Evaluation of Biaxial Mechanical Properties of Aortic Media Based on the Lamellar Microstructure. *Materials*. 2015, 8(1), 302–316. ISSN 1996-1944.
146. TAUBIN, G. Curve and surface smoothing without shrinkage. In: *Proceedings of IEEE International Conference on Computer Vision*. 1995. IEEE Comput. Soc. Press, pp. 852–857
147. THIBODEAU, G. A. and PATTON, K. T. *Structure & function of the body*. 14th ed. 2012. Elsevier

148. TORRE, L. A., BRAY, F., SIEGEL, R. L., FERLAY, J., LORTET-TIEULENT, J., and JEMAL, A. Global cancer statistics, 2012. *CA: A Cancer Journal for Clinicians*. 2015, 65(2), 87–108. ISSN 00079235.
149. TRICERRI, P. Mathematical and Numerical Modeling of Healthy and Unhealthy Cerebral Arterial Tissues. 2014, 6232
150. TRICERRI, P., DEDÈ, L., GAMBARUTO, A., QUARTERONI, A., and SEQUEIRA, A. A numerical study of isotropic and anisotropic constitutive models with relevance to healthy and unhealthy cerebral arterial tissues. *International Journal of Engineering Science*. 2016, 101126–155. ISSN 00207225.
151. TU, J., INTHAVONG, K., and WONG, K. K. L. *Computational Hemodynamics – Theory, Modelling and Applications*. Antimicrobial agents and chemotherapy. 2015. Dordrecht: Springer Netherlands
152. VALENCIA, A., BURDILES, P., IGNAT, M., MURA, J., BRAVO, E., RIVERA, R., and SORDO, J. Fluid Structural Analysis of Human Cerebral Aneurysm Using Their Own Wall Mechanical Properties. *Computational and Mathematical Methods in Medicine*. 2013, 20131–18. ISSN 1748-670X.
153. DE VILLIERS, A. M., MCBRIDE, A. T., REDDY, B. D., FRANZ, T., and SPOTTISWOODE, B. S. A validated patient-specific FSI model for vascular access in haemodialysis. *Biomechanics and Modeling in Mechanobiology*. 2017, 1–19. ISSN 16177940.
154. VU, N.-H., PHAM, X.-T., FRANÇOIS, V., and CUILLIÈRE, J.-C. Characterization of multilayered carbon-fiber–reinforced thermoplastic composites for assembly process. *Journal of Thermoplastic Composite Materials*. 2018, 089270571877287. ISSN 0892-7057.
155. WALLER, B. F., ORR, C. M., SLACK, J. D., PINKERTON, C. A., VAN TASSEL, J., and PETERS, T. Anatomy, histology, and pathology of coronary arteries: A review relevant to new interventional and imaging techniques-Part I. *Clinical Cardiology*. 1992, 15(7), 535–540. ISSN 01609289.
156. WALSH, M. T., CUNNANE, E. M., MULVIHILL, J. J., AKYILDIZ, A. C., GIJSEN, F. J. H., and HOLZAPFEL, G. A. Uniaxial tensile testing approaches for characterisation of atherosclerotic plaques. *Journal of Biomechanics*. 2014, 47(4), 793–804. ISSN 18732380.
157. WANG, L., HILL, N. A., ROPER, S. M., and LUO, X. Modelling peeling- and pressure-driven propagation of arterial dissection. *Journal of Engineering Mathematics*. 2018, 109(1), 227–238. ISSN 15732703.
158. WEISBECKER, H., PIERCE, D. M., and HOLZAPFEL, G. A. A generalized prestressing algorithm for finite element simulations of preloaded geometries with application to the aorta. *International Journal for Numerical Methods in Biomedical Engineering*. 2014, 30(9), 857–872. ISSN 20407939.
159. WYKES, V. and VINDLACHERUVU, R. Intracranial pressure, cerebral blood flow and brain oedema. *Surgery (United Kingdom)*. 2015, 33(8), 355–362. ISSN 18781764.
160. YOSIBASH, Z., MANOR, I., GILAD, I., and WILLENTZ, U. Experimental

evidence of the compressibility of arteries. *Journal of the Mechanical Behavior of Biomedical Materials*. 2014, 39339–354. ISSN 17516161.
161. YOSIBASH, Z. and PRIEL, E. p -FEMs for hyperelastic anisotropic nearly incompressible materials under finite deformations with applications to arteries simulation. *International Journal for Numerical Methods in Engineering*. 2011, 88(11), 1152–1174. ISSN 00295981.
162. YOSSEF, O. E., FARAJIAN, M., GILAD, I., WILLENZ, U., GUTMAN, N., and YOSIBASH, Z. Further experimental evidence of the compressibility of arteries. *Journal of the Mechanical Behavior of Biomedical Materials*. 2017, 65177–189. ISSN 17516161.
163. ZDUNEK, A. and RACHOWICZ, W. A mixed higher order FEM for fully coupled compressible transversely isotropic finite hyperelasticity. *Computers and Mathematics with Applications*. 2017, 74(7), 1727–1750. ISSN 08981221.
164. ZHENG, Y. and MAYHEW, J. A time-invariant visco-elastic windkessel model relating blood flow and blood volume. *NeuroImage*. 2009, 47(4), 1371–1380. ISSN 10538119.

PUBLICATIONS RELATED TO THE DISSERTATION

Articles in journals from "Clarivate Analytics" "Web of Science" database list

1. MISIULIS, E., DŽIUGYS, A., NAVAKAS, R., and STRIŪGAS, N. A fluid-structure interaction model of the internal carotid and ophthalmic arteries for the noninvasive intracranial pressure measurement method. Computers in Biology and Medicine. 2017, 84(March), 79–88. ISSN 18790534.
2. MISIULIS, E., DŽIUGYS, A., NAVAKAS, R., and PETKUS, V. A comparative study of methods used to generate the arterial fiber structure in a clinically relevant numerical analysis. International Journal for Numerical Methods in Biomedical Engineering. 2019, e3194. ISSN 2040-7939. (in-press)

Articles in journals, referred in international scientific databases

1. MISIULIS, E., SKARBALIUS, G., and DŽIUGYS, A. Numerical evaluation of systematic errors of a non-invasive intracranial pressure measurement. Energetika. 2018, 64(3), 121–136. ISSN 1822-8836.

Publications at the international conferences

1. MISIULIS E., DŽIUGYS A. Numerical study of time dependent blood flow in ophthalmic artery with applied external pressure. *12th Annual international conference of young scientists on energy issues (CYSENI 2015)*, Kaunas, Lithuania, May 27–28, 2015. Kaunas: LEI, 2015. p. 270-278. ISSN 1822-7554.
2. MISIULIS E., DŽIUGYS A. Effect geometrical chape and boundary condition on stress distribution and deformation in ophthalmic artery numerical model. *13th Annual international conference of young scientists on energy issues (CYSENI 2016)*, Kaunas, Lithuania, May 26–27, 2016. Kaunas: LEI, 2016. p. 363-370. ISSN 1822-7554.
3. MISIULIS E., DŽIUGYS A. An investigation of the balance principle implemented by non-invasive intracranial pressure measurement method by means of computational modeling. *The 14th International Conference of Young Scientists on energy Issues (CYSENI 2017)*, Kaunas, Lithuania, May 25-26, 2017. Kaunas: LEI, 2017, p. 298-307. ISSN 1822-7554.
4. MISIULIS E., DŽIUGYS A. Investigation of a complex fluid-structure interaction problem in a patient specific ophthalmic artery using fiber-reinforced artery wall constitutive model. *The 15th International Conference of Young Scientists on Energy Issues (CYSENI 2018)*, Kaunas, Lithuania, May 23-25, 2018. Kaunas: LEI, 2018, p. 360-367. ISSN 1822-7554.

Publications at the national conferences

1. MISIULIS E., DŽIUGYS A., NAVAKAS R. Kraštinių sąlygų įtaka įtempių pasiskirstymui ir deformacijoms akies arterijos skaitiniame modelyje. *Šilumos energetika ir technologijos-2016: konferencijos pranešimų medžiaga*, Kauno technologijos universitetas, 2016 sausio 28-29 Kaunas: LEI 2016. p. 146-154. ISSN 2335-2485.

Reports in the international conferences

1. MISIULIS E., DŽIUGYS A. Numerical study of time dependent blood flow in ophthalmic artery with applied external pressure. *12th Annual international conference of young scientists on energy issues (CYSENI 2015)*, Kaunas, Lithuania, May 27–28, 2015. Kaunas: LEI, 2015. p. 270-278. ISSN 1822-7554.
2. MISIULIS E., DŽIUGYS A. Effect geometrical chape and boundary condition on stress distribution and deformation in ophthalmic artery numerical model. *13th Annual international conference of young scientists on energy issues (CYSENI 2016)*, Kaunas, Lithuania, May 26–27, 2016. Kaunas: LEI, 2016. p. 363-370. ISSN 1822-7554.
3. MISIULIS E., DŽIUGYS A. An investigation of the balance principle implemented by non-invasive intracranial pressure measurement method by means of computational modeling. *The 14th International Conference of Young Scientists on energy Issues (CYSENI 2017)*, Kaunas, Lithuania, May 25-26, 2017. Kaunas: LEI, 2017, p. 298-307. ISSN 1822-7554.
4. MISIULIS E., DŽIUGYS A. Investigation of a complex fluid-structure interaction problem in a patient specific ophthalmic artery using fiber-reinforced artery wall constitutive model. *The 15th International Conference of Young Scientists on Energy Issues (CYSENI 2018)*, Kaunas, Lithuania, May 23-25, 2018. Kaunas: LEI, 2018, p. 360-367. ISSN 1822-7554.
5. MISIULIS E., DŽIUGYS A. A new method for the formation of fiber-reinforced structure in the curved artery for the numerical modeling applications. *Emerging Trends in Applied Mathematics and Mechanics (ETAMM)*, Krakow, Poland, June 18-22, 2018. Book of Abstracts, p. 214.

Reports in the national conferences

1. MISIULIS E., DŽIUGYS A., NAVAKAS R. Kraštinių sąlygų įtaka įtempių pasiskirstymui ir deformacijoms akies arterijos skaitiniame modelyje. *Šilumos energetika ir technologijos-2016: konferencijos pranešimų medžiaga*, Kauno technologijos universitetas, 2016 sausio 28-29 Kaunas: LEI 2016. p. 146-154. ISSN 2335-2485.
2. MISIULIS E., DŽIUGYS A. Skaitinis balanso principo taikomo neinvaziniame galvospūdžio matavime tyrimas. *Šilumos energetika ir technologijos-2017*, Kauno technologijos universitetas, 2017 sausio 26, Kaunas.
3. MISIULIS E., DŽIUGYS A. Skaitinis arterijų modeliavimas. *Šilumos energetika ir technologijos-2018*, Kauno technologijos universitetas, 2018 vasario 1, Kaunas.

SL344. 2019-05-02, 13,5 leidyb. apsk. l. Tiražas 12 egz. Užsakymas 102.

Išleido Kauno technologijos universitetas, K. Donelaičio g. 73, 44249 Kaunas
Spausdino leidyklos „Technologija“ spaustuvė, Studentų g. 54, 51424 Kaunas